COHERENT SOFT X-RAY MAGNETIC SCATTERING AND SPATIAL COHERENCE DETERMINATION

DISSERTATION
ZUR ERLANGUNG DES DOKTORGRADES
DES FACHBEREICHS PHYSIK
DER UNIVERSITÄT HAMBURG

vorgelegt von
Dipl.-Phys. Kai Bagschik
aus Hamburg

Hamburg
März 2017

Gutachter der Dissertation:	Prof. Dr. Hans Peter Oepen *Universität Hamburg, Germany* Prof. Dr. Gerhard Grübel *DESY, Germany*
Zusammensetzung der Prüfungskommission:	Prof. Dr. Hans Peter Oepen *Universität Hamburg, Germany* Prof. Dr. Gerhard Grübel *DESY, Germany* Prof. Dr. Robert Heinrich Blick *Universität Hamburg, Germany* Prof. Dr. Daniela Pfannkuche *Universität Hamburg, Germany* Prof. Dr. Nils Huse *Universität Hamburg, Germany*
Vorsitzende der Prüfungskommission:	Prof. Dr. Daniela Pfannkuche
Datum der Disputation:	12.05.2017
Vorsitzender des Promotionsausschusses:	Prof. Dr. Wolfgang Hansen
Leiter des Fachbereichs Physik:	Prof. Dr. Michael Potthoff
Dekan der Fakultät für Mathematik, Informatik und Naturwissenschaften:	Prof. Dr. Heinrich Graener

Abstract

In this thesis mainly two topics in the field of coherent X-ray magnetic scattering are addressed. The first topic deals with the determination of spatial coherence properties of synchrotron radiation in the soft X-ray range by means of magnetic speckle patterns. For this purpose an X-ray resonant magnetic scattering experiment at the L_3 absorption edge of cobalt has been performed using Co/Pt multilayers and CoPd alloy films. The obtained magnetic speckle patterns arise from scattering at magnetic domain patterns due to the X-ray magnetic circular dichroism. A method is introduced that is based on the analysis of the Fourier transform of magnetic speckle patterns and gives access to the two-dimensional representation of the mutual coherence function. It exploits the fact that the autocorrelation function of a disordered magnetic maze domain pattern possesses perfectly flat side lobes. The method allows for the simultaneous determination of the transverse coherence length in all radial directions of the illuminating beam.

The second topic deals with the investigation and characterization of magnetic maze domain patterns of a wedge-shaped Co/Pd multilayer film as a function of cobalt thickness close to and within the spin-reorientation transition. The thickness-driven evolution of the magnetic microstructure is studied by means of X-ray resonant magnetic scattering. Magnetic diffraction patterns of the magnetic domain structures as a function of cobalt thickness are extracted from the CCD images. The radial profiles of the scattering intensity reveal variations of the peak position, width and amplitude. For the interpretation of the changing intensity profiles a model has been developed to describe highly disordered maze domain patterns. The model is based on a synthetic one-dimensional domain pattern with gamma-distributed domain sizes to imply the significant domain size variations. It is described by the mean domain size, the domain-wall width, and the shape parameter of the gamma distribution that is found to be characteristic for a certain pattern geometry. As a proof of principle the obtained information from the scattering experiment is used to determine thickness-dependent anisotropies of the wedge-shaped Co/Pd multilayer.

Kurzzusammenfassung

Diese Arbeit befasst sich hauptsächlich mit zwei Themen aus dem Gebiet der kohärenten magnetischen Röntgenstreuung. Der erste Themenbereich beschäftigt sich mit der Ermittlung der räumlichen Kohärenzeigenschaften von Synchrotronstrahlung im weichen Röntgenbereich mit Hilfe von magnetischen Specklebildern. Dafür wurde ein resonantes magnetisches Röntgenstreuexperiment an der L_3 Absorptionskante von Kobalt unter der Verwendung von Co/Pt Multilagenfilmen und CoPd Legierungsfilmen durchgeführt. Die erhaltenen magnetischen Specklebilder entstehen dabei durch Streuung an magnetischen Domänenstrukturen infolge des Röntgenzirkulardichroismus. In der Arbeit wird eine Methode vorgestellt, die auf der Analyse der Fouriertransformation von magnetischen Specklebildern basiert und einen Zugang zur zweidimensionalen Darstellung der gegenseitigen Kohärenzfunktion verschafft. Dabei wird ausgenutzt, dass die Autokorrelationsfunktion von ungeordneten labyrinthartigen magnetischen Dömanenstrukturen perfekt plane Flanken aufweist. Die Methode erlaubt die gleichzeitige Ermittlung der transversalen Kohärenzlänge in allen radialen Richtungen des einfallenden Strahls .

Der zweite Themenbereich befasst sich mit der Untersuchung und Charakterisierung von labyrinthartigen magnetischen Domänenstrukturen von Co/Pd Multilagenkeilen in Abhängigkeit der Kobaltdicke nahe bei und innerhalb des Spinreorientierungsübergangs. Resonante magnetische Röntgenstreuung wird benutzt um die durch die Schichtdickenänderung hervorgerufene Veränderung der magnetischen Mikrostruktur zu untersuchen. Die aus den CCD Bildern extrahierten radialen Streuintensitätsprofile der magnetischen Domänenstrukturen zeigen Veränderungen der Peak-position, Breite und Intensität als Funktion der Kobaltschichtdicke. Um dieses Verhalten zu erklären wird ein Model vorgestellt, welches eine Beschreibung von ungeordneten labyrinthartigen magnetischen Domänenstrukturen ermöglicht. Das Model basiert auf synthetischen eindimensionalen Domänenstrukturen mit gammaverteilten Domänengrößen um signifikante Domänengrößenvariationen mit einzuschließen. Beschrieben wird das Model durch die mittlere Domänengröße, der Domänenwandbreite und dem Formparameter der Verteilungsfunktion, wobei gezeigt wird, dass dieser charakteristisch für eine bestimmte Domänenstrukturgeometrie ist. Als Anwendungsfall für das Model werden die Ergebnisse genutzt um Schichtdickenabhängige Anisotropien der Co/Pd Multilagenkeile zu bestimmen.

CONTENTS

LIST OF FIGURES

1 INTRODUCTION

Over the last decades, the field of research of thin film magnetism has evolved enormously. Much effort has been put into the study of the magnetic properties of thin films, which is especially due to their various technological applications such as sensors and actuators or data storage [1–8]. Current basic research in this field of research aims to investigate changes of the magnetic microstructure and magnetic reversal processes of diverse magnetic materials depending on material thickness (e.g., bulk or surface- and interface-determined properties), chemical composition (e.g., alloys or compounds), internal structure (e.g., morphology, symmetry, lateral patterning), and especially in reaction to external excitations (e.g., magnetic field, electrical current, THz or IR radiation) [9–17]. A solid knowledge and understanding of the resulting micromagnetic phenomena allows for tailoring magnetic properties, such as anisotropy, coercivity, remanence, exchange coupling, etc., to the specific requirements of present and future technologies. Investigations of the magnetic domain structure in magnetic materials enable access to many of these properties, as these structures essentially link the physical properties (anisotropy, exchange, stray field) of these materials with their macroscopic properties (magnetization, domain size, domain wall width, domain morphology) [18, 19]. The observation of magnetic domains has significantly contributed to the present state of knowledge of micromagnetic phenomena in thin films [18, 20–22]. Magnetic domain studies support the evolution of magnetic materials with custom-tailored properties, result in a deeper insight into magnetization processes and a better understanding of magnetic properties in thin films.

Scientific research has always been closely connected to technological applications. New insights often result in new innovative technologies, where magnetism is mostly associated with data storage devices and magnetic sensors [18, 23–25]. Nowadays large-scale storage is mainly based on magnetic hard disc drives (HDDs) where information is stored in sub-100 nm sized magnetic regions (bits), written and read out by magnetic thin-film heads. The magnetic microstructure of the utilized storage materials does not play a direct role in these devices, however, it causes energy losses created in the storage material and noise effects in the read-and-write heads [19]. New generation storage devices are aimed at higher areal densities (10 Tbit/in^2 [26–28])[1] and ever-faster switching times (1 THz = 10^{12}/s [26, 29, 30])[2]. To achieve this, the development of novel magnetic materials, further progress in theoretical developments, and the development of new experimental techniques are required, especially since novel devices with higher areal densities require ever smaller lateral bit dimensions down to a few nanometers ($d_{\mathrm{grain}} < 10$ nm)[27, 28]. Technically important are complex film structures consisting of multilayer thin films, alloys and compounds with a large number of diverse chemical constituents exhibiting magnetic microstructures with characteristic sizes in the nanometer range.

Static and dynamic investigations of the magnetic microstructure of these complex thin film systems, elementally resolved and with high spatial and temporal resolution, is still a challenge in modern research. Several well-established techniques exist to study nanometer-sized magnetic microstructures.

One approach is magnetic force microscopy (MFM), where a few-nm-sized magnetic tip scans above the surfaces of the sample and interacts with the stray field generated by the magnetic domains [31–33]. With this technique a two-dimensional map of the domain structure with a typical spatial resolution of around 30 nm is obtained [32].[3] However, the time resolution is strongly limited by the duration of the scanning process (few minutes). Additionally, MFM is highly susceptible to external magnetic fields often needed for domain investigations and also no depth-selective information can be obtained. A second scanning probe technique is spin-polarized scanning tunneling microscopy (Sp-STM) which reaches atomic resolution (< 1 nm) [35]. Sp-STM makes use of the spin of tunneling electrons to get information on the local sample magnetization. It is surface sensitive (< 0.2 nm) so that buried layers cannot be probed. In addition, it is relies on ideal crystalline surfaces of the probed sample.

Another seminal technique is scanning electron microscopy with polarization analysis (SEMPA), which probes the spin-polarization of low-energy secondary electrons

[1] 10 Tbit/in^2 $\approx 1.6 \cdot 10^{-2}$ bit/nm^2 $\hat{=}$ bits with 8 nm size.
[2] Switching process within 1 ps.
[3] A spatial resolution of around 10 nm has been reported using extensively modified tips with special coating [33, 34].

emitted from the magnetic sample [36, 37]. It achieves a high spatial resolution down to 3 nm [38] and recently a time resolution of 700 ps has been reported [39]. SEMPA has the unique advantage that two components of the magnetization can be detected simultaneously, which enables a vectorial magnetic imaging. Thus, SEMPA quantifies the magnitude and direction of the local magnetization directly. However, SEMPA is inherently surface sensitive due to the short mean free path of the secondary electrons ($l_\mathrm{e} < 1$ nm) and not suitable for studies using strong external fields due to the detection of low-energy secondary electrons. A related electron-based technique is Lorentz microscopy which is performed in transmission geometry and is based on the deflection of electrons traversing the magnetic sample due to the Lorentz force of the sample's magnetic field [40, 41]. Lorentz microscopy achieves a spatial resolution below 1 nm [42] and a temporal resolution of around 10 ns [43]. It can be performed in the presence of magnetic fields due to the high energy of the primary electrons.

An alternative approach is Kerr microscopy, which is based on the magneto-optical Kerr-effect (MOKE) [17, 44]. MOKE describes the rotation of the plane of polarization of linearly polarized light upon reflection at the surface of a sample with magnetization M. The observation of magnetic domains is given by a weak dependence of the optical constants on the direction of the magnetization. Using ultra-short intense laser pulses in pump-probe geometry, magnetization dynamics in the femtosecond regime can be probed where the time resolution is limited by the pulse length [45]. As an optical method, it is insensitive to applied external fields. A major drawback of this technique is the diffraction-limited spatial resolution which is around 200 nm using blue light ($\lambda = 460$ nm).

Since the pioneering work of Bergevin and Brunel in the 1970s [46], which used X-rays for magnetic investigations, a completely new field has been established, promoted by the development of synchrotron sources and free-electron lasers [47]. The short wavelengths enable high spatial resolution and ultra-short femtosecond X-ray pulses allow for studies of ultrafast magnetization dynamics. Due to the availability of X-ray sources with their high brilliance and the possibility of tuning the photon energy and polarization, investigations of magnetic samples in the soft and hard X-ray range become feasible and the strong variation of the magneto-optical constants at the absorption edges becomes accessible. Tuning the photon energy to the absorption edges opens up the possibility to investigate magnetism element selectively due to the ability to excite core-level electrons. This property is extremely useful for studies of individual magnetic layers within multilayer structures consisting of diverse magnetic materials. Additionally, external fields can be applied without affecting the probe.

Several X-ray techniques for the investigation of nanometer-sized magnetic microstructures have been developed during the last 30 years. These techniques are based on the X-ray magnetic circular dichroism (XMCD) that is characterized by an X-ray absorption cross-section depending on the orientation of local magnetization with respect to the helicity of incident circularly polarized X-rays. One approach is magnetic X-ray transmission microscopy which is a real-space technique and uses Fresnel zone plates (FZP) [48, 49]. It can be performed either in full-field operation (MTXM) [50, 51] or in scanning operation (STXM) [52, 53]. In a MTXM a condenser zone plate focuses the X-ray beam onto the sample and an image is obtained from the transmitted intensity using a micro zone plate. In a STXM an FZP focuses the X-ray beam onto the sample and an image is obtained by raster-scanning the sample. The spatial and time resolution is of around $15-25$ nm [51, 54–56] and 70 ps [57, 58] in MTXM and STXM. Both techniques are insensitive to external magnetic fields. Another method is X-ray photo-electron emission microscopy (X-PEEM), which measures X-ray induced photo-emitted secondary electrons, for which the intensity is proportional to the local X-ray absorption [21, 59]. X-PEEM is a surface-sensitive technique and is highly susceptible to external magnetic fields. This technique achieves 20 nm spatial resolution [60] and 15 ps time resolution [61].

Promising techniques based on coherent X-ray scattering are X-ray resonant magnetic scattering (XRMS) [62–65] and the lensless X-ray holographic microcopy (FTH, XHM) [66–69], which can be seen as complementary methods. Holographic microscopy uses an otherwise opaque optics mask containing an object hole and a reference hole in front of the transparent sample. The object hole defines the region of interest and the reference hole enables to recover the phase of the object wave. The generated hologram is recorded by a charge-coupled device (CCD) and a real-space image is obtained via a simple Fast Fourier Transform. The spatial resolution is limited by the maximum scattering angle detectable with the CCD and the size of the reference hole, which can be fabricated to a size smaller than 30 nm and hence sub-15 nm spatial resolution become feasible. Ultrafast pump-probe experiments using FTH have been performed with femtosecond time resolution [70, 71]. XRMS is used to obtain ensemble-averaged information from the magnetic microstructure, where the magnetic diffraction pattern caused by scattering from magnetic domains is detected by a CCD. Characteristic average properties, such as average domain size and lateral correlation length can be extracted. Thus, XRMS gives information about the collective behavior of the magnetic microstructure and hence gives global statistical information. Due to the fact that XRMS does not require any special optics, the spatial resolution is solely limited by the wavelength and the detectable maximum momentum transfer Q. In general, however, signal-to-noise limitations are relevant due to the dynamic range of the detector and the photon statistics as the intensity drops strongly towards higher Q.

In this thesis, magnetic domain patterns of a magnetic multilayer are investigated by means of XRMS. It is shown that by using suitable models, there is in fact a variety of information about the real-space domain patterns that can be extracted from magnetic diffraction patterns. The analysis and the developed model presented in this thesis are applied to static measurements of domain patterns. However, the main motivation is to use them for the interpretation of magnetic diffraction patterns obtained from dynamic experiments, especially with respect to ultrafast magnetization dynamics performed at free-electron lasers [11, 72–74]. Experiments of ultrafast femtosecond magnetization dynamics, such as ultrafast demagnetization [75–78], attract considerable attention in recent years as they are motivated by the question of fundamental time limits for the manipulation, destruction and control of local magnetic order. Such experiments are mainly performed using the XRMS technique in pump-probe geometry. XRMS compared to FTH offers the advantage of probing the collective response of the magnetic system to the external excitation and a simple operation without expensively manufactured optics masks. In addition, XRMS possesses a better signal-to-noise ratio (S/N). The interpretation of the magnetic diffraction patterns and their correlation to the real-space domain structure is an important issue and still under debate [73]. One part of this thesis deals specifically with this issue.

An important aspect which has not been addressed so far is the coherence of X-ray radiation. Coherence plays a decisive role for the performance of X-ray experiments like for instance FTH, XHM, coherent diffractive imaging (CDI) or X-ray ptychography. Holographic imaging is based on the interference between the exit waves of the object and reference hole, separated by a distance of around 3 μm. Hence these experiments demand a sufficiently large transverse coherence length to obtain useful magnetic contrast in the reconstructions. Particularly, X-ray radiation produced by synchrotron radiation sources is only coherent to a certain degree and can thus be seen as partially coherent. Consequently, the determination of the coherence properties of X-ray sources is of high interest since they are the essential prerequisites for interference-based X-ray experiments. Because of the high demand on beamtime at synchrotron and FEL facilities, experiments are very limited in time and consequently coherence measurements have to be simple and not too time consuming. Young's double pinhole experiments have been performed at synchrotron sources and FELs to determine the coherence properties for diverse beamline parameters [79–81]. Additionally, coherence experiments using non-redundant arrays of apertures (NRAs) [79, 82, 83] and uniformly-redundant arrays of apertures (URAs) [84, 85] have been conducted at synchrotron sources. The latter allow for some time saving due to the fact that they effectively perform many Young's double pinhole experiments simultaneously. However, all these techniques require expensively manufactured apertures and the analysis to determine the coherence length is in general lengthy. A promising method to determine coherence properties is the use of spatial intensity-correlation functions of speckle patterns from random scatterers [86–89]. The obtained speckle contrast characterizes the coherence properties by one number and can be extracted from the speckle pattern with low effort. However, this method does not allow for a direct measurement of the transverse coherence length. At this point this thesis sets in and a new method is demonstrated which makes use of magnetic speckle patterns produced by magnetic maze domain patterns. It is based on the Fourier transform of magnetic speckle patterns, is characterized by a simple and fast analysis and allows for an online check of the coherence properties.

This thesis is focused on the investigation of disordered magnetic maze domain patterns and the determination of the spatial coherence properties of X-ray radiation from synchrotron sources. *Chapter* 2 gives the framework for the understanding of this thesis and introduces the fundamentals of coherence theory and X-ray resonant magnetic scattering.

In *Chapter* 3 the holographic imaging endstation used for the X-ray scattering experiments is described, as well as the beamline parameters and optical elements of the beamline P04 at PETRA III where all experiments presented in this thesis have been performed. A short description of the fabrication procedure of the samples used is presented at the end of this chapter.

The newly developed Fourier analysis method to determine the coherence properties of synchrotron radiation is presented in *Chapter* 4. This chapter starts with a mathematical description of the method and general aspects of the properties of the autocorrelation function of magnetic domain patterns. Two experiments are demonstrated and a detailed description of the analysis procedure is given.

Chapter 5 presents an X-ray resonant magnetic scattering experiment on a wedge-shaped Co/Pd multilayer. The chapter begins with a characterization of the sample system. Subsequently, the experiment is described, followed by the analysis of the experimental findings using a newly developed model for the interpretation of diffraction patterns from highly-disordered maze domain patterns. The chapter closes with an analysis of the magnetic properties of the sample using the obtained information from the scattering experiment. A short description of the fundamentals of micromagnetism is given prior to the analysis.

Chapter 4 and *Chapter* 5 are separately introduced and end with a conclusion and an outlook.

2 FUNDAMENTALS OF SOFT X-RAY RESONANT MAGNETIC SCATTERING AND COHERENCE THEORY

In this chapter the theoretical foundations and terminologies of this thesis are introduced and described. The first section of this chapter deals with the theory of optical coherence, which is based on the statistical properties of radiation (section 2.1.1). A model is introduced to describe the radiation properties of partially coherent X-ray sources (section 2.1.2). The substantial quantities of the electromagnetic radiation such as spatial (section 2.1.3) and temporal coherence (section 2.1.4) are discussed. As an example, the coherence properties of the soft X-ray beamline P04 at PETRA III are analyzed and the influence of the source parameters and beamline optics on the coherence properties are explained (section 2.1.5). The second section deals with the fundamentals of X-ray resonant magnetic scattering from magnetic specimens. Starting from the definition of X-ray absorption and the optical constants (section 2.2.1), the strong X-ray magnetic circular dichroism (XMCD) effect at the absorption edges of $3d$ transition metals is introduced (section 2.2.2). Subsequently, an introduction to scattering theory is presented (section 2.2.3). Finally, X-ray resonant magnetic scattering on magnetic domains is described, together with a brief discussion about spatial coherence and magnetic speckle patterns (section 2.2.4).

2.1 Coherence theory

The following section focuses on the coherence theory of X-ray radiation produced by undulator-based sources at storage rings. The source can be treated as a sum of individual point sources emitting radiation with various amplitudes and phases. The total radiation can be expressed by a superposition of all these light fields. Due to random fluctuation of the source arising when point sources emit light independently with diverse frequencies and phases, the total radiation can be described by its statistical properties. This fact led to the field of statistical optics and optical coherence.

2.1.1 Coherence and correlation functions

Synchrotron radiation sources do not provide fully spatial and temporal coherent X-ray radiation. The degree of coherence of these sources is relatively high, but far away from the coherence properties of laser light. Thus, the X-ray radiation can be described by partially coherent light fields.

The main quantity of coherence theory is the so-called mutual coherence function (MCF) which is a first-order correlation function in terms of the electric field. For the case of stationary and ergodic light fields the MCF is defined as [90–93]

$$\Gamma\left(\mathbf{s}_1, \mathbf{s}_2, \tau\right) = \left\langle E\left(\mathbf{s}_1, t\right) E^*\left(\mathbf{s}_2, t+\tau\right)\right\rangle_T. \tag{2.1}$$

The MCF describes the correlation between two electrical field values $E(\mathbf{s}_1, t)$ and $E^*(\mathbf{s}_2, t+\tau)$ at two different points in space $\mathbf{s}_1$ and $\mathbf{s}_2$ with a time delay of τ. The brackets $\langle ... \rangle$ denote averaging over a time interval T. The stationarity and ergodicity of the radiation is a good approximation for synchrotron radiation sources [92–94].

The self-correlation of the electrical field meaning $\mathbf{s}_1 = \mathbf{s}_2 = \mathbf{s}$ and $\tau = 0$ yields the average intensity

$$\langle I\left(\mathbf{s}, t\right)\rangle = \left\langle \left|E\left(\mathbf{s}, t\right)\right|^2 \right\rangle = \Gamma\left(\mathbf{s}, \mathbf{s}, 0\right). \tag{2.2}$$

The normalized representation of the MCF is called complex degree of coherence (CDC) and is defined as

$$\gamma\left(\mathbf{s}_1, \mathbf{s}_2, \tau\right) = \frac{\Gamma\left(\mathbf{s}_1, \mathbf{s}_2, \tau\right)}{\sqrt{\Gamma\left(\mathbf{s}_1, \mathbf{s}_1, 0\right)\Gamma\left(\mathbf{s}_2, \mathbf{s}_2, 0\right)}} = \frac{\Gamma\left(\mathbf{s}_1, \mathbf{s}_2, \tau\right)}{\sqrt{\langle I\left(\mathbf{s}_1, t\right)\rangle \langle I\left(\mathbf{s}_2, t\right)\rangle}}. \tag{2.3}$$

The modulus of the CDC varies from zero for incoherent radiation to one for fully coherent radiation and is said to be partially coherent if $0 < |\gamma\left(\mathbf{s}_1, \mathbf{s}_2, \tau\right)| < 1$. The modulus of the CDC at different spatial and temporal separations $\Delta\mathbf{s} = \mathbf{s}_1 - \mathbf{s}_2$ and τ, can be experimentally accessed by performing interference experiments, e.g., Young's double pinhole experiments [79, 80, 82, 95]. The characteristic lengths, such as transverse and longitudinal coherence length, can be extracted from profiles of the

CDC. These will be discussed in detail later.

In the so-called quasi-monochromatic approximation, meaning a narrow spectral bandwidth $\Delta\lambda$ of the X-ray radiation with respect to the mean $\bar{\lambda}$, the MCF $\Gamma(\mathbf{s}_1, \mathbf{s}_2, \tau) \approx \Gamma(\mathbf{s}_1, \mathbf{s}_2, 0) = \Gamma(\mathbf{s}_1, \mathbf{s}_2)$ and CDC $\gamma(\mathbf{s}_1, \mathbf{s}_2, \tau) \approx \gamma(\mathbf{s}_1, \mathbf{s}_2, 0) = \gamma(\mathbf{s}_1, \mathbf{s}_2)$ are independent on the time delay τ. Within this approximation Eq. 2.3 transforms to [92]

$$\gamma\left(\mathbf{s}_1, \mathbf{s}_2\right) = \frac{\Gamma\left(\mathbf{s}_1, \mathbf{s}_2\right)}{\sqrt{\Gamma\left(\mathbf{s}_1, \mathbf{s}_1\right)\Gamma\left(\mathbf{s}_2, \mathbf{s}_2\right)}} = \frac{\Gamma\left(\mathbf{s}_1, \mathbf{s}_2\right)}{\sqrt{I\left(\mathbf{s}_1\right)I\left(\mathbf{s}_2\right)}}. \tag{2.4}$$

and $\Gamma(\mathbf{s}_1, \mathbf{s}_2)$ and $\gamma(\mathbf{s}_1, \mathbf{s}_2)$ are now equal-time correlation functions that describe the spatial coherence of the field. The coherence time τ_c and longitudinal coherence length of the radiation are inverse proportional to $\Delta\lambda$. If $\tau \ll \tau_\mathrm{c}$, the quasi-monochromatic approximation can be applied. This means that the longitudinal coherence length is much larger than any path length difference that occurs in the experiments. The latter is valid for the mSAXS[1] experiments at a synchrotron beamline described in this thesis, where a monochromator provides a narrow spectral bandwidth and the small scattering angles ensure small values of τ.

2.1.2 Van Cittert-Zernike theorem and Gaussian Schell-model

Within the framework of the Van Cittert-Zernike theorem the light emitting source is assumed to be fully incoherent [90, 96, 97]. It states that each point source inside the source radiates independently and no correlations appear at any distance between them. The source can be described as a thermal source with Gaussian intensity profile [92, 98, 99]. The Van Cittert-Zernike theorem can be used to predict the coherence properties of the radiation at any distance from the source [92, 100]. Thus, the characteristic transverse coherence length can be estimated. A thermal source is radiating as an incoherent source over a solid angle of 4π. However, synchrotron radiation is strongly directional with a narrow cone. Due to this confinement, the source can possess an effective degree of transverse coherence. Hence, the Van Cittert-Zernike theorem does not describe synchrotron radiation rigorously [100–102]. A detailed discussion about the applicability of different models to describe synchrotron radiation is given in [98].

A more accurate formalism is the Gaussian Schell-model (GSM), which is widely

[1]Magnetic small-angle X-ray scattering

used in the synchrotron community to describe reliably the radiation properties of partially coherent sources [92, 100–104]. In general, the GSM is based on the so-called cross spectral density function (CSD), which is the Fourier transform of the mutual coherence function with respect to τ

$$W(\mathbf{s}_1, \mathbf{s}_2, \omega) = \int \Gamma\left(\mathbf{s}_1, \mathbf{s}_2, \tau\right) \exp(-i\omega\tau) d\tau. \tag{2.5}$$

However, in quasi-monochromatic approximation, where the bandwidth is small compared to the mean frequency ω_0, the GSM reveals [90]

$$\Gamma\left(\mathbf{s}_1, \mathbf{s}_2, 0\right) = \Gamma\left(\mathbf{s}_1, \mathbf{s}_2\right) \propto W(\mathbf{s}_1, \mathbf{s}_2, \omega_0). \tag{2.6}$$

The GSM assumes the source to have a certain degree of coherence and can be used to calculate the transverse coherence length and the beam size at any distance z from the source. Further assumptions are that the source is described as a planar two-dimensional source and the source intensity distribution $I\left(\mathbf{s}\right)$ and complex degree of coherence $\gamma(\mathbf{s}_1, \mathbf{s}_2)$ are Gaussian functions. In the following, the three-dimensional position vector $\mathbf{s}$ is written as $\mathbf{s} = (\mathbf{r}, z)$, where $\mathbf{r} = (x, y)$ is a two-dimensional vector and z represents the position along the optical axis. The mutual coherence function of the source at $z = 0$ within the quasi-monochromatic GSM is then given by [93, 94, 105–108]

$$\Gamma\left(\mathbf{r}_1, \mathbf{r}_2; z = 0\right) = \sqrt{I\left(\mathbf{r}_1\right)}\sqrt{I\left(\mathbf{r}_2\right)}\gamma\left(\mathbf{r}_1 - \mathbf{r}_2\right), \tag{2.7}$$

with

$$I\left(\mathbf{r}\right) = I_0 \exp\left(-\frac{x^2}{2\sigma_{\mathrm{x}}^2} - \frac{y^2}{2\sigma_{\mathrm{y}}^2}\right), \tag{2.8}$$

$$\gamma\left(\mathbf{r}_1 - \mathbf{r}_2\right) = \exp\left(-\frac{(x_1 - x_2)^2}{2\xi_{\mathrm{T,x}}^2} - \frac{(y_1 - y_2)^2}{2\xi_{\mathrm{T,y}}^2}\right), \tag{2.9}$$

where $\sigma_{\mathrm{x,y}}$ and $\xi_{\mathrm{T,x,y}}$ are defined as the root-mean-square (rms) source size and transverse coherence length in horizontal (x) and vertical (y) directions, respectively. Additionally, the complex degree of coherence only depends on the separation of any two points within the beam $\gamma(\mathbf{r}_1, \mathbf{r}_2) = \gamma(\mathbf{r}_1 - \mathbf{r}_2) = \gamma(\Delta\mathbf{r})$ (Schell-model sources [109]).

In the framework of the GSM the source intensity distribution and the complex degree of coherence are factorizable (see Eq. 2.8 and 2.9) and can be calculated separately for the horizontal and vertical directions.

2.1.3 Spatial coherence and transverse coherence length

Spatial coherence deals with the correlation of the electric fields at two different points $\mathbf{r}_1$, $\mathbf{r}_2$ with zero delay $\tau = 0$ ($\Gamma(\mathbf{r}_1, \mathbf{r}_2, 0)$) [92]. The transverse coherence length is a measure of the spatial distance, transverse to the propagation direction, over which a certain degree of correlation of the electric fields exists. This applies both for the source and along the propagation direction.

Within the framework of the Van Cittert-Zernike theorem, the (rms) transverse coherence length of the beam from an incoherent source with Gaussian intensity distribution at a distance z from the source[2] is given by [87, 96–98]

$$\Xi(z) = \frac{\lambda z}{2\pi\sigma}. \tag{2.10}$$

As mentioned in section 2.1.2, the Van Cittert-Zernike theorem does not describe accurately the properties of X-ray radiation from undulator-based sources [100–102].

In the framework of the Gaussian Schell-model, the transverse coherence length of the source and along the propagation direction is defined as the separation at which the complex degree of coherence drops to a value of 0.6. This separation is equivalent to the (rms) width of the Gaussian. In the following, the relevant quantities to describe the X-ray beam and its spatial coherence at the source ($z = 0$) and away from the source ($z > 0$) in the framework of the quasi-monochromatic Gaussian Schell-model are discussed. For a detailed description it is referred to the literature [92, 93, 99]. The mutual coherence function at a distance z away from the source is given by [92, 93, 100, 105]

$$\Gamma(x_1, x_2, z) \propto \frac{I_0}{\Delta(z)} \exp\left(-\frac{x_1^2 + x_2^2}{4\Sigma^2(z)} - \frac{(x_1 - x_2)^2}{2\Xi^2(z)} + \frac{ik(x_1^2 - x_2^2)}{2R(z)}\right), \tag{2.11}$$

where $\Delta(z)$ is the expansion coefficient and $R(z)$ is the radius of the curvature. The same can be calculated for the y direction. The separability is a property of the GSM. The beam size $\Sigma(z)$ and the transverse coherence length $\Xi(z)$ at a distance z from the source, as well as the angular divergence of the beam θ_Σ and the coherent segment θ_Ξ (see Fig. 2.1) is given by

$$\Xi(z) = \left(\xi_{\mathrm{T,S}}^2 + \theta_\Xi^2 z^2\right)^{1/2}, \ \theta_\Xi = \frac{\lambda}{2\pi\sigma}\left(1 + p^2/4\right)^{1/2}, \tag{2.12}$$

[2]The far field condition is fulfilled.

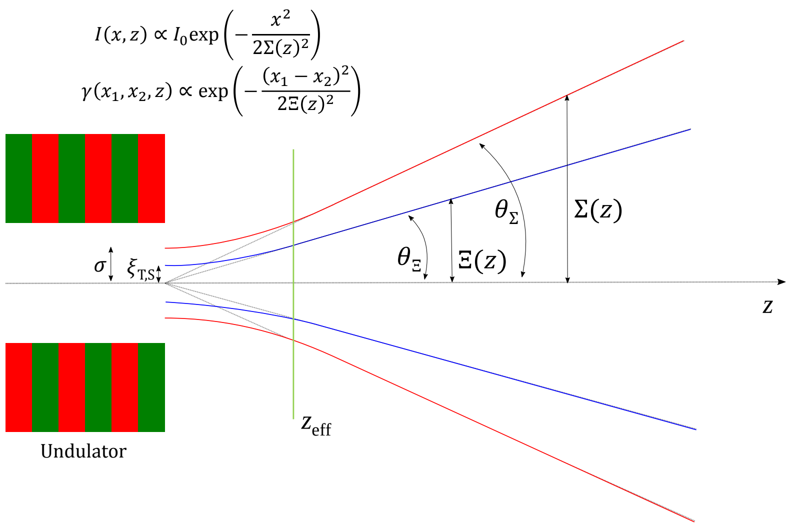

Figure 2.1: One-dimensional illustration of the propagation of Gaussian Schell-model beams in free space describing the undulator source σ, the X-ray beam via $\Sigma(z)$ and the spatial coherence properties at the source $\xi_{\mathrm{T,S}}$ and in propagation direction $\Xi(z)$. The distance z_{eff} separates the near-field and far-field region.

$$\Sigma(z) = \left(\sigma^2 + \theta_\Sigma^2 z^2\right)^{1/2}, \; \theta_\Sigma = \frac{\lambda}{2\pi\xi_{\mathrm{T,S}}}\left(1 + p^2/4\right)^{1/2}. \tag{2.13}$$

The parameter $p = \xi_{T,S}/\sigma = \Xi(z)/\Sigma(z)$ is a constant at the source and along the propagation direction z. It gives the relation between the transverse coherence length of the source and source size, and states that this relation is conserved along the propagation direction [94, 110]. In addition it is a characteristic quantity defining the degree of coherence of the source and the beam. If $p \gg 1$ or $p \ll 1$ both are considered to be coherent or incoherent, respectively. The source and the beam are partially coherent if $p = 1$.

At large distances z from an incoherent source ($p \ll 1$), the transverse coherence length $\Xi(z)$ in Eq. 2.12 resembles the expression obtained from the Van Cittert-Zernike theorem (see Eq. 2.10). At this point it becomes clear that the GSM includes the Van Cittert-Zernike theorem.

Another important quantity of the GSM is the effective distance

$$z_{\mathrm{eff}} = \frac{4\pi\sigma^2 p}{\lambda(p^2+4)^{1/2}}, \tag{2.14}$$

which marks the transition between the Fresnel and Fraunhofer region in the propagation. If the source is spatially fully coherent the effective distance is equivalent to the Rayleigh length which is known from Gaussian beams [111].

The knowledge of the transverse coherence length is not sufficient to understand how coherent the source or the X-ray beam is. In this case, a global degree of coherence (normalized degree of transverse coherence) can be introduced, which characterizes the transverse coherence properties by one number [81, 98, 100].

$$\zeta = \frac{p}{\sqrt{4+p^2}}. \tag{2.15}$$

ζ varies from zero for incoherent to one for coherent radiation. It can even be factorized and calculated separately for the horizontal ζ_{x} and vertical ζ_{y} directions. The total degree of transverse coherence is given by the product $\zeta = \zeta_{\mathrm{x}}\zeta_{\mathrm{y}}$ of both components.

A further relevant parameter is the emittance or transverse phase-space of the source, which is in the frame of the GSM defined by [93, 100]

$$\epsilon = \sigma\theta_{\Sigma} = \frac{\lambda}{4\pi\zeta}. \tag{2.16}$$

The parameter ζ in Eq. 2.16 accounts for the different degrees of spatial coherence. In case of $\zeta = 1$, i.e., fully spatial coherence, the source is said to be diffraction limited and $\epsilon = \lambda/4\pi$. This is achieved by a point source radiating spherical wavefronts where the electric fields are perfectly correlated at every point transverse to the propagation direction. In case of $\zeta \longrightarrow 0$, the source is fully incoherent and $\epsilon \gg \lambda/4\pi$. The emittance of the source can now be used together with Eq. 2.13 to give an expression for the transverse coherence length of the source of any degree of spatial coherence

$$\xi_{\mathrm{T,S}} = \frac{2\sigma}{\sqrt{\frac{16\pi^2}{\lambda^2}\epsilon^2 - 1}}. \tag{2.17}$$

The experiments presented in this thesis were conducted at the P04 beamline at PETRA III [112]. As an example, the source size $\sigma^{\mathrm{x,y}} \approx 140\ \mu\mathrm{m}$, $21\ \mu\mathrm{m}$ and angular divergence $\theta_{\Sigma}^{\mathrm{x,y}} \approx 14\ \mu\mathrm{rad}$, $13\ \mu\mathrm{rad}$ of the beamline in horizontal and vertical directions at $\lambda = 1.59$ nm can be used to calculate the coherence parameters via the equations above (see Fig. 2.2). The calculated transverse coherence lengths of the source in horizontal and vertical direction are $\xi_{\mathrm{T,S}}^{\mathrm{x}} = 18\ \mu\mathrm{m}$ and $\xi_{\mathrm{T,S}}^{\mathrm{y}} = 22\ \mu\mathrm{m}$, re-

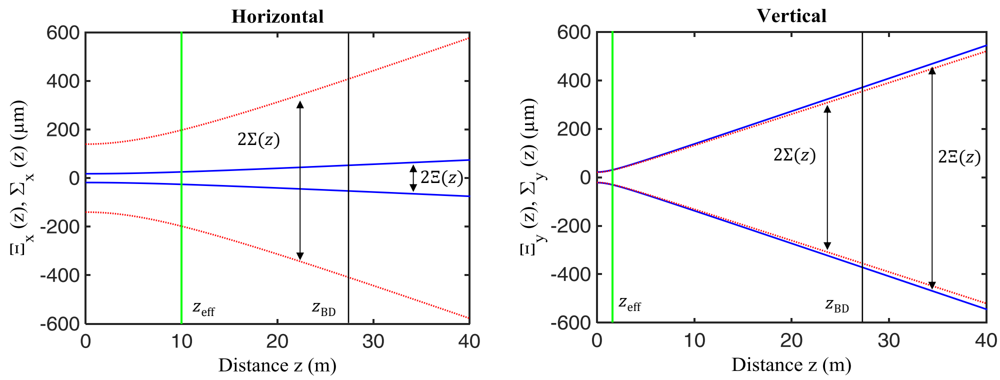

Figure 2.2: Beam size $\Sigma_{\mathrm{x,y}}$ (red dashed line) and transverse coherence length $\Xi_{\mathrm{x,y}}$ (blue solid line) in horizontal and vertical directions at different distances z from the source using the beam parameter of the beamline P04 at PETRAIII. The green solid line corresponds to the effective distance z_{eff} and the black solid line is the distance z_{BD} from the source at which the beam-defining slit of P04 is positioned.

spectively. Hence, the source is incoherent ($p = 0.13; \zeta = 0.06$) in horizontal direction and partially coherent ($p = 1.05; \zeta = 0.46$) in vertical direction. Figure 2.2 shows the transverse coherence lengths $\Xi(z)$ (blue solid line) and beam size $\Sigma(z)$ (red dashed line) in horizontal and vertical direction at different distances from the source. The green solid line represents the effective distance $z_{\mathrm{eff}}^{\mathrm{x,y}} = 10$ m, 1.6 m and the black solid line the distance $z_{\mathrm{BD}} = 27.9$ m at which the beam-defining slit of the beamline P04 is positioned. At z_{BD} the transverse coherence lengths in horizontal and vertical direction are $\Xi_{\mathrm{x}}(z = 27.9 \text{ m}) = 54\ \mu$m and $\Xi_{\mathrm{y}}(z = 27.9 \text{ m}) = 380\ \mu$m, respectively. The Gaussian beam size $\Sigma(z)$ at $z = 27.9$ m can be calculated to $\Sigma_{\mathrm{x}}(z = 27 \text{ m}) = 415\ \mu$m (0.98 mm FWHM) and $\Sigma_{\mathrm{y}}(z = 27.9 \text{ m}) = 363\ \mu$m (0.85 mm FWHM).

2.1.4 Temporal coherence and longitudinal coherence length

Temporal coherence deals with the correlation of the electric fields with $\mathbf{r}_1 = \mathbf{r}_2 = \mathbf{r}$ at different delays τ $(\Gamma(\mathbf{r}, \mathbf{r}, \tau))$ [92]. The longitudinal coherence length is a measure of the spatial distance, along the propagation direction, over which a certain degree correlation of the electric fields exists. Hence, it defines the degree of monochromaticity of the source and the beam.

The longitudinal coherence length $\xi_{\mathrm{L,S}}$ of a synchrotron source is determined by the number of undulator magnet periods N, the wavelength λ and $\Delta\lambda$ (FWHM) at λ [92]

$$\xi_{\mathrm{L,S}} = \lambda(\lambda/\Delta\lambda) = \lambda n N, \tag{2.18}$$

where n denotes the n-th harmonic of the radiation. The coherence time is given by $\tau_{\mathrm{c,S}} = \xi_{\mathrm{L,S}}/c$, where c is the speed of light. The longitudinal coherence length of radiation from the undulator (1st harmonic) at the beamline P04 at PETRA III ($N = 72$) at a wavelength of $\lambda = 1.59$ nm is $\xi_{\mathrm{L,S}} = 0.11$ μm and the coherence time results in $\tau_{\mathrm{c,S}} = 0.37$ fs. Hence, the coherence time of the source is much smaller than the (rms) electron bunch length of $\sigma_{\mathrm{Bunch}} \approx 42.5$ ps [112]. The latter proves the applicability of the stationary theory for the statistical properties of synchrotron radiation (see Eq. 2.1), as a large variety of field fluctuations arise within a single pulse.

At undulator beamlines the longitudinal coherence length of the beam can be increased by means of a monochromator (spectral filtering) providing a high resolving power $R = \lambda/\Delta\lambda$. In this case, the longitudinal coherence length is determined by $\xi_{\mathrm{L}} = \lambda R$. The resolving power of the monochromator at the P04 beamline at $\lambda = 1.59$ nm is $R \approx 3 \times 10^3$ (exit-slit size of 200 μm), which results in a longitudinal coherence length of $\xi_{\mathrm{L}} = 4.8$ μm. Hence, via spectral filtering (monochromator) the longitudinal coherence length is in this case increased by a factor of ≈ 40.

Diffraction experiments are limited by the the longitudinal coherence length as it determines the maximum optical path-length difference Δs that enables interference of diffracted beams

$$\xi_{\mathrm{L}} > \Delta s = a \sin\varphi, \tag{2.19}$$

where a is the size of the illuminated area of the sample and φ is the maximum recorded diffraction angle.

2.1.5 Influence of beamline optics on coherence properties

In the following, the influence of optical elements, such as apertures, the monochromator, and the focusing optics on the coherence properties of the X-ray beam is briefly discussed.

Beam-defining aperture

The beam-defining aperture is one of the first optical elements and is in general a pair of slits for the horizontal and vertical directions [47, 113]. Its purpose is primarily to cut out the coherent part of the X-ray beam emitted from the source. By cutting the beam with the aperture ($z = z_{\mathrm{BD}}$), the relations p and ζ for the transmitted beam $\Sigma(z > z_{\mathrm{BD}})$ are increased due to the decreased beam size, where $\Xi(z > z_{\mathrm{BD}})$ remains unaffected unless the apertures are closed to much. Thus, the degree of spatial coherence of the transmitted beam is increased inversely proportional to the amount of truncation. The beam-defining aperture is in general far away from the experimental platform and thus cutting the beam at ($z = z_{\mathrm{BD}}$) does not affect the size of the beam in the focus $\Sigma(z_{\mathrm{F}})$ at the experimental platform. However, due to the increased relations p and ζ and the property of the GSM that these relations are constant along the propagation direction in free space, $\Xi(z_{\mathrm{F}})$ in the focus increases proportional to p and ζ. Thus, cutting the beam emitted by the source results in an increase of the transverse coherence length at the experiment. In this discussion it is assumed that the beam-defining aperture only cuts Σ and not Ξ, which means that the slit width is larger than the coherent fraction of the beam. A further truncation of the beam would result in a more complicated treatment of the beam properties. An adverse side effect is that cutting the beam is always at the expense of overall transmission.

Coherence measurements at 400 eV ($\lambda = 3.1$ nm) with varying beam-defining slit openings in vertical direction have been conducted by Skopintsev et al. [79] at the P04 beamline at PETRA III, utilizing non-redundant arrays (NRAs) of apertures. They found that the transverse coherence length in vertical direction measured at the experimental platform in the focus is inversely proportional to the beam-defining slit width and proportional to ζ in the same direction. These experimental findings are in-line with the discussion about the beam properties above. They measured an increase of the transverse coherence length from 2.4 μm to 9.2 μm, an increase of the normalized degree of transverse coherence from $\zeta = 0.06$ to $\zeta = 0.25$, as well as a decrease of photon flux by a factor of four with decreasing beam-defining slit openings from 4.7 mm to 0.8 mm.

It must be pointed out, that a slit or a pinhole does not have a Gaussian transmission function. Diffraction on the sharp edges of the aperture leads to oscillations within the Gaussian intensity profile of the beam and the CDC [114, 115]. If the beam has a small transverse coherence length the edge effects are small and the CDC can be well described by the GSM. However, if the beam is highly coherent the

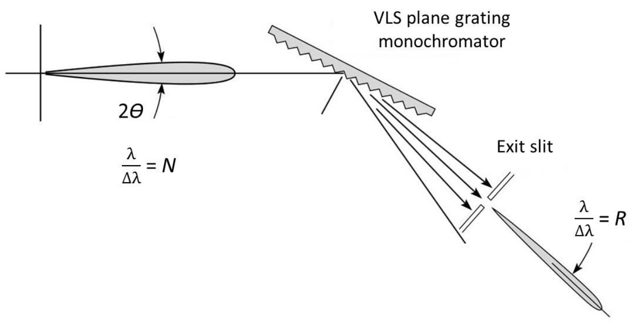

Figure 2.3: Illustration of the working principle of a monochromator together with an exit slit. The beam coming from the undulator, with a relative spectral bandwidth $\lambda/\Delta\lambda = N$ is spectrally separated and focused into the plane of the exit slit by means of the monochromator. The exit slit monochromatizes the beam via a reduction of the spectral bandwidth $\Delta\lambda$. Image taken from [47]

edge effects are notably high and the GSM overestimates the transverse coherence length slightly [115].

Monochromator and exit aperture

Monochromators used at soft X-ray synchrotron beamlines are, e.g., the plane-grating monochromator (PGM), the spherical-grating monochromator (SGM) or the variable-angle SGM [116]. The following section is discussed for the case of a varied line-space (VLS) plane-grating monochromator [117–119], as the experiments in this thesis have been conducted at the P04 Beamline at PETRA III where this type of monochromator is used [112]. In this case, the X-ray beam is directed to a varied line-space grating unit. The VLS grating focuses the beam in vertical direction into the plane of an exit aperture (see Fig. 2.3). Due to angular dispersion the beam becomes spectrally separated and the exit aperture monochromatizes the X-ray beam via a reduction of the spectral bandwidth $\Delta\lambda$. The latter reduction is tunable by adjusting the vertical exit aperture opening. Consequently, an increased longitudinal coherence length ξ_L can be achieved (see section 2.1.4). This fact is essential for experiments requiring a quasi-monochromatic beam condition.

The focusing of the beam to the position of the exit slit results in a magnified image of the source σ at that position. Truncation of the beam by decreasing the exit slit opening, in this case, results not only in an increased resolving power but also in a decreased emittance ϵ of the source (Eq. 2.16). As a result, the transverse coherence length of the source $\xi_{\mathrm{T,S}}$ is also increased, inversely proportional to the exit slit opening, and leads to an increased transverse coherence $\Xi(z_{\mathrm{F}})$ at the experimental platform. In addition, the exit slit opening has a direct impact on the size of the beam at $\Sigma(z_\mathrm{F})$. Chang et al. [80], Skopintsev et al. [79], Rose et al. [82] and Paterson et al. [120] performed coherence measurements with variable vertical exit slit openings and found an increase of the transverse coherence length $\Xi(z_\mathrm{F})$ in vertical direction inverse proportional to the exit slit openings.

Focusing mirrors

Focusing mirrors are primarily used to increase the photon flux of the X-ray beam. In the following, the case of a focusing element with a large aperture is discussed which is the case for most of the focusing optics at synchrotron beamlines [114, 121]. The large aperture approximation means that the aperture of the focusing optics is much larger than the beam size of the incident radiation. At the beamline P04 the focusing mirrors (KB system) are designed to accept an (rms) beam size of 6σ [82, 112]. In this case, the focusing optics only modify the curvature of the beam. In the framework of the Gaussian Schell-model, the (rms) beam size $\Sigma(z_\mathrm{F})$ and transverse coherence length $\Xi(z_\mathrm{F})$ in the focus can be directly related to the source parameters upstream of the focusing element [114, 121, 122] by

$$\Sigma(z_\mathrm{F}) = M_\mathrm{mag}\sigma, \;\; \Xi(z_\mathrm{F}) = M_\mathrm{mag}\xi_\mathrm{T,S} \tag{2.20}$$

with

$$M_\mathrm{mag} = \left|\frac{f}{z_\mathrm{L} - f}\right| \sqrt{\left[1 + \frac{z_\mathrm{eff}^2}{(z_\mathrm{L} - f)^2}\right]}. \tag{2.21}$$

M_mag is called magnification factor, f is the focal length and z_L is the distance from the source to the focusing element. For the case that $z_\mathrm{L} - f \gg z_\mathrm{eff}$ or $\zeta \to 0$ the magnification factor can be expressed by

$$M_\mathrm{mag} = \left|\frac{f}{z_\mathrm{L} - f}\right|. \tag{2.22}$$

The parameter p introduced in section 2.1.3, i.e., the relation between the transverse coherence length and the beam size, is constant with focusing. Hence, it is important for experiments requiring a high transverse coherence length in the focus that the p parameter is substantially high prior to focusing to prevent vanishingly small coherence lengths in the focus. Another option to obtain a higher transverse coherence length is to move out of the focus or to increase the size of the focus. However, the latter causes a loss of photon flux.

2.2 Soft X-ray resonant magnetic scattering

The following section focuses on the theory of resonant scattering at magnetic samples using soft X-rays. An introduction to X-ray absorption and the X-ray magnetic circular dichroism is given, followed by an introduction to scattering theory. In this context, the link between X-ray scattering and absorption is discussed. Subsequently, resonant magnetic scattering at magnetic domain patterns is presented, together with a brief discussion about the formation of magnetic speckle patterns in dependence on different degrees of spatial coherence of the illuminating beam.

2.2.1 X-ray absorption and optical constants

The interaction of X-ray radiation and matter can be described macroscopically by the Beer-Lambert law. It states that when X-rays passing through a material the X-ray intensity decays exponentially. The transmitted intensity can be expressed by [123]

$$I\left(E,Z,t\right)=I_0e^{-\mu_{\mathrm{x}}(E,Z)t}, \tag{2.23}$$

where t is the thickness of the material and $\mu_{\mathrm{x}}\left(E,Z\right)$ is the linear absorption coefficient which depends on the material Z and the incident photon energy $E=\hbar\omega$. The linear absorption coefficient can be represented by a penetration length λ_{x} via $\mu_{\mathrm{x}}=1/\lambda_{\mathrm{x}}$. λ_{x} is a characteristic length which brings the intensity to an attenuation by a factor $1/e$. Figure 2.4 illustrates λ_{x} as a function of photon energy in the soft X-ray range, which shows the strong absorption at the L_3 and L_2 edges of cobalt.

The same process can be treated in terms of a plane electromagnetic wave $\boldsymbol{E}(z,t)$ passing through a material represented by the complex refractive index $n(E)=1-\delta(E)+\mathrm{i}\beta(E)$. The real part $\delta(E)$ describes the refraction and the imaginary part $\beta(E)$ the absorption of the electromagnetic wave in the material. The electromagnetic wave traversing the material along the z direction is given by [47]

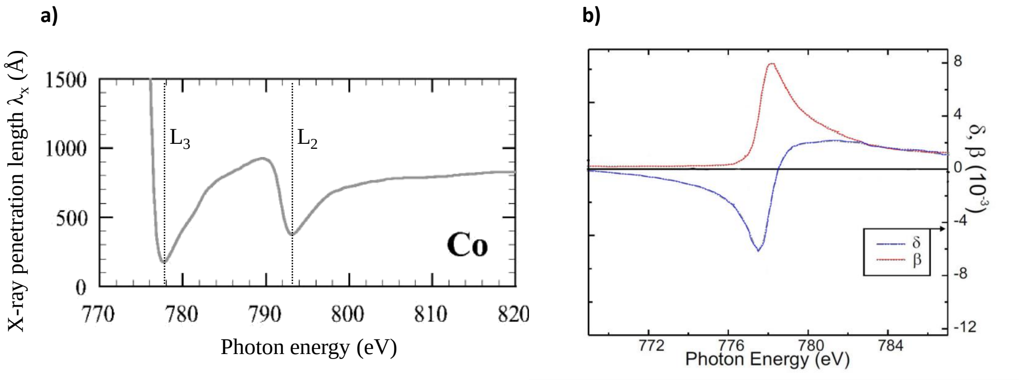

Figure 2.4: a) The X-ray penetration length λ_x of Cobalt as a function of photon energy in the soft X-ray regime. The strong absorption at 778 eV and 793 eV correspond to the (L_3) and (L_2) edges, respectively. Image taken from [124]. b) Optical constants of Cobalt at the L_3 edge. Image taken from [125].

$$
\begin{aligned}
\boldsymbol{E}(z,t) &= \boldsymbol{E}_0 e^{i(\omega n(E)z/c-\omega t)} \\
&= \boldsymbol{E}_0 e^{i\omega(z/c-t))} \underbrace{e^{-ik\delta(E)z}}_{\text{phase shift}} \underbrace{e^{-k\beta(E)z}}_{\text{absorption}},
\end{aligned}
\tag{2.24}
$$

where $k = 2\pi/\lambda$ is the wavevector and ω is the frequency. The first term in Eq. 2.24 represents the propagation in vacuum, the second term induces a phase shift represented by $\delta(E)$ and the third term describes the absorption represented by $\beta(E)$ which decreases the amplitude of the incident electromagnetic wave. By comparing Eq. 2.23 and the squared version of Eq. 2.24 a direct link between the absorption $\beta(E)$ and the linear absorption coefficient $\mu_\mathrm{x}(E)$ is found [123]

$$
\beta(E) = \frac{\mu_\mathrm{x}(E)\lambda}{4\pi} = \frac{\rho_\mathrm{a}\lambda}{4\pi}\sigma^{\mathrm{abs}}(E). \tag{2.25}
$$

The second expression in Eq. 2.25 follows from $\mu_\mathrm{x}(E) = \rho_\mathrm{a}\sigma^{\mathrm{abs}}(E)$ and connects the absorption with the X-ray absorption cross section $\sigma^{\mathrm{abs}}(E)$ which gives the number of photons absorbed per atom divided by the number of incident photons per unit area at a certain photon energy [123]. ρ_a is the atomic number density.

2.2.2 X-ray magnetic circular dichroism

The X-ray magnetic circular dichroism (XMCD) effect describes the dependency of the X-ray absorption on the helicity of circularly polarized X-rays and the magnetization orientation of a magnetic material. The first theoretical predictions of the XMCD effect can be traced back to the work of Erskine and Stern [126], whereby the first experimental realization has been performed by Schütz et al. [127]. The XMCD can be directly related to the optical Faraday effect [128], describing the rotation of linearly polarized light (in the visible range) traversing magnetic materials in external magnetic fields, and the Kerr effect [129], describing the same relation in reflection geometry. The X-ray technique allows for element-specific measurements and the determination of orbital and spin angular moments using sum rules, which is an important advantage compared to the above mentioned techniques performed at wavelengths in the visible range.

Two-step model of the XMCD effect

The XMCD effect can be described by a simple two-step model [123, 130]. In the framework of the two-step model the circularly polarized X-rays are first absorbed by the magnetic specimen and excite spin-polarized core level electrons. In a second step, the unoccupied exchange-split d-bands serve as a spin detector for the excited spin-polarized photoelectrons with respect to the magnetic moment $\boldsymbol{m}$. The exchange-splitting of the d-bands is caused by the exchange interaction of d-band electrons (Stoner model) [123, 131].

In the following the XMCD effect of transition metals at the L_3 and L_2 absorption edges are discussed in detail with regard to the two-step model. In $3d$ transition metals the $2p$ core levels are split into $2p_{3/2}$ and $2p_{1/2}$ sub-levels due to spin-orbit coupling. Circularly polarized X-rays provide a photon angular momentum given by $\boldsymbol{L}_{\mathrm{ph}}^{+} = +\hbar$ for right circular polarization and $\boldsymbol{L}_{\mathrm{ph}}^{-} = -\hbar$ for left circular polarization where the quantization axis of the angular momentum is in the direction of the wavevector k and $-k$, respectively .

In a first step, the incident circularly polarized X-rays trigger atomic core-to-valence excitations ($2p \rightarrow 3d$) by transferring their angular momentum to the photoelectrons. Due to spin-orbit coupling the angular momentum can be transferred to the spin. Hence, left- and right-circularly polarized X-rays excite photoelectrons with opposite spin owing to their opposite momentum ($\pm\hbar$) (see Fig. 2.5). The excitation of photoelectrons from the $2p_{3/2}$ and $2p_{1/2}$ states into the $3d$-states corresponds to the

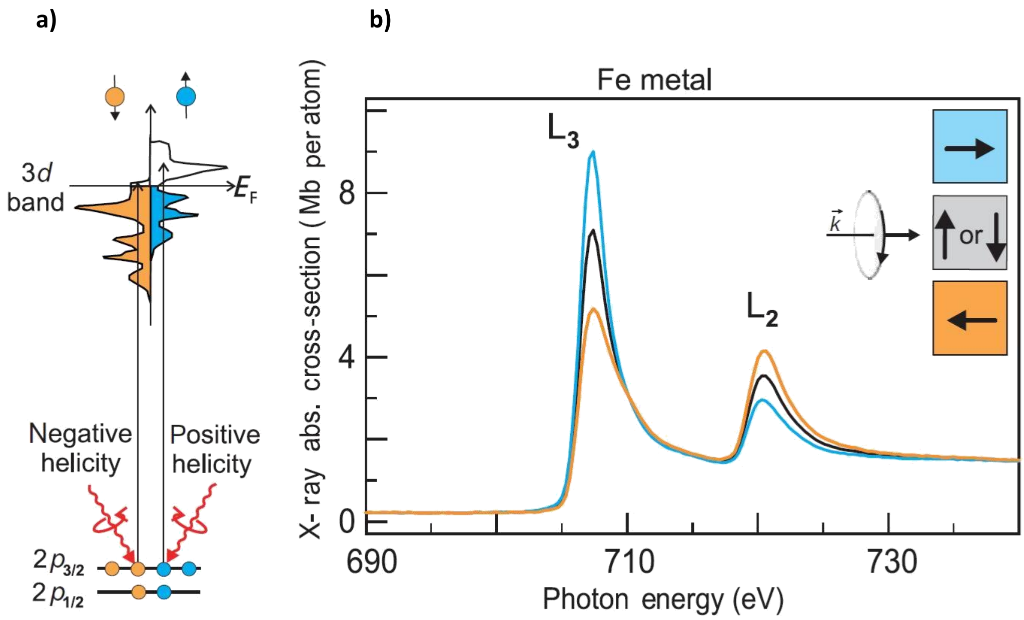

Figure 2.5: XMCD effect at the L edges of iron. a) Excitation of spin-polarized photoelectrons into the exchange-splitted d-bands of iron using X-rays with opposite helicity. b) X-ray absorption cross section of circularly polarized X-rays in the soft X-ray regime using a ferromagnetic iron sample with magnetization direction aligned with respect to the direction of the photon angular momentum. Image taken from [123].

L_3 and L_2 absorption edges where the spin polarization is opposite due to their reverse spin-orbit coupling ($L_3 \triangleq l + s$ and $L_2 \triangleq l - s$). The selection rules for dipole transitions with respect to the absorption process besides the conservation of angular momentum $\Delta l = \pm 1$ are also given by $\Delta m_l = \pm 1$ and $\Delta m_s = 0$. Thus, the spin of the excited photoelectrons is conserved for the described dipole transitions.

In a second step, the exchange-splitted $3d$-bands act as a "spin detector" for the excited spin-polarized photoelectrons. Due to the imbalance of unoccupied holes in the spin-up and spin-down $3d$-bands above the Fermi energy, the absorption is different for left- and right-circularly polarized X-rays, which results in the dichroism effect. The quantization axis of the spin detector is the magnetic moment $\boldsymbol{m}$ of the magnetic sample. Maximum XMCD occurs if the magnetization direction is aligned with respect to the direction of the photon angular momentum ($\pm k$) and by tuning the photon energy to the correct energy corresponding to the L_3 and L_2 absorption edges of the $3d$ transition metals (778 eV and 793 eV for Co, 707 eV and 720 eV for Fe, and 853 eV and 870 eV for Ni, respectively [132]). In contrast, if the magnetization direction is perpendicular to the direction of the photon angular momentum, the "up-" and "down-" spin directions cannot be distinguished (see Fig. 2.5). The transmitted XMCD intensity is given by [130]

$$I^{\pm} \propto P_{\mathrm{circ}} \cdot \boldsymbol{m} \cdot \boldsymbol{L}_{\mathrm{ph}}^{\pm} \propto P_{\mathrm{circ}} \cdot \langle \boldsymbol{m} \rangle \cos\theta, \tag{2.26}$$

where P_{circ} is the degree of circular polarization, $\boldsymbol{m}$ and $\langle \boldsymbol{m} \rangle$ are the magnetic moment and its expectation value of the $3d$-band, and θ is the angle between the direction of $\boldsymbol{L}_{\mathrm{ph}}^{\pm}$ and the magnetic moment $\boldsymbol{m}$.

The XMCD effect is in general defined as the difference of the intensities obtained from photoelectron excitations with left- and right-circularly polarized X-rays $\Delta I = I^{+} - I^{-}$. It is worth mentioning that an equal XMCD effect is obtained using only one helicity of the circular polarization and reversing the magnetization direction $\boldsymbol{M}$ by sufficiently high external magnetic fields to saturate the magnetic sample.

Taking account of the XMCD effect in ferromagnetic samples, the complex refractive index $n(E)$ (see section 2.2.1) depends on the polarization state of the illuminating radiation and has to be modified to

$$n_{\pm}(E) = 1 - (\delta(E) \pm \Delta\delta(E)) + \mathrm{i}\,(\beta(E) \pm \Delta\beta(E))\,. \tag{2.27}$$

The subscript ($\pm$) corresponds to left- and right-circular polarization. The additional contributions in the real and imaginary part of $n_{\pm}$ are the magneto-optical constants $\Delta\delta(E)$ and $\Delta\beta(E)$ which are the magnetic contributions ($\neq 0$ for ferromagnetic materials). They give rise to a variation in absorption and phase using left- and right- circularly polarized radiation [133, 134]. The magneto-optical constants depend strongly on the photon energy, similar to the usual optical constants [125, 133].

2.2.3 Introduction to scattering theory

The scattering of X-rays by an atom is described by scattering at the electron cloud. The electrons start to oscillate during the scattering process and emit spherical waves. The total scattering amplitude of the atom is given by the sum of the scattering amplitudes of all electrons. A mathematical description of the scattering process is given by the atomic form factor or scattering amplitude which is the Fourier transform of the charge density $\rho_e(\mathbf{r})$, i.e., the number density of electrons in the atom [130]

$$F_0(\boldsymbol{Q}) = -\frac{1}{e}\int \rho_e(\mathbf{r}) e^{i\boldsymbol{Q}\mathbf{r}} d\mathbf{r}, \tag{2.28}$$

where $\boldsymbol{Q} = \boldsymbol{k} - \boldsymbol{k}'$ is the momentum transfer. If the wavelength λ of the incident radiation is large compared to the atomic size (forward scattering), the atomic form factor is in good approximation given by the total number of electrons Z. The latter applies in the soft X-ray range, where the absorption edges of the $3d$ transition metals are situated (see previous sections). The non-resonant differential atomic scattering cross section, which gives the angular distribution of scattering from an atom, i.e., intensity scattered into a solid angle $d\Omega$, is expressed by

$$\left(\frac{d\sigma}{d\Omega}\right)_{\text{atom}} = r_0^2 \left|\boldsymbol{\varepsilon}\cdot\boldsymbol{\varepsilon}'\right|^2 \left|F_0(\boldsymbol{Q})\right|^2, \tag{2.29}$$

where $\boldsymbol{\varepsilon}$ and $\boldsymbol{\varepsilon}'$ are the unit polarization vectors of the incident and scattered waves and r_0 is the Thomson scattering length or classical electron radius ($= 2.82\times10^{-6}$ nm). For incident linearly polarized X-rays, $\boldsymbol{\varepsilon}$ is perpendicular to the X-ray wavevector $\boldsymbol{k}$ and for incident circularly polarized X-rays $\boldsymbol{\varepsilon}$ can be considered as a superposition of two linearly polarized X-rays.

X-ray resonant scattering can be described semiclassically through a resonant absorption and emission of a photon with energy $E = \hbar\omega$, which corresponds to the energy or resonance frequency of a harmonic oscillator. The differential atomic resonant scattering cross-section is then given by

$$\left(\frac{d\sigma}{d\Omega}\right)_{\text{atom}} = r_0^2 \left|\boldsymbol{\varepsilon}\cdot\boldsymbol{\varepsilon}'\right|^2 \Bigg|\underbrace{F_0(\boldsymbol{Q}) + F'(E) - iF''(E)}_{F(\boldsymbol{Q},E)}\Bigg|^2. \tag{2.30}$$

The additional contributions F' and F'' in comparison to Eq. 2.29 account for the refractive and absorptive contributions to the scattering process. For the case of forward scattering $F_0(\boldsymbol{Q}) = Z$, the resonant forward scattering factor $F(E)$ can be separated into $f_1(E) = Z + F(E)'$ and $f_2(E) = F(E)''$, which are called Henke-Gullikson factors [123, 135]. The optical theorem states that the imaginary part of $F(E)$ is proportional to the absorption cross section, which gives a direct link between scattering and absorption [123] (see Eq. 2.25)

$$\mathrm{Im}\left[F\left(E\right)\right]=f_2\left(E\right)=\frac{1}{2\lambda r_0}\sigma^{abs}\left(E\right). \tag{2.31}$$

In a quantum mechanical picture, the absorption of X-rays and the X-ray scattering cross section can be determined within the framework of the time-dependent perturbation theory. Within the latter theory, the incident X-ray radiation excites a transition from an initial state $|a\rangle$ to an intermediate state $|n\rangle$ and subsequently the system goes back to $|a\rangle$ via emission of a photon (resonant elastic scattering). In this case, the differential resonant elastic scattering cross section in dipole approximation is expressed by [130]

$$\left(\frac{d\sigma}{d\Omega}\right)_{\text{atom}}=r_0^2\left|F(E)\right|^2=\frac{\hbar^2\omega^4}{c^2}\alpha_{\mathrm{f}}^2\left|\sum_n\frac{\langle a\left|\mathbf{r}\cdot\boldsymbol{\varepsilon}'\right|n\rangle\langle n\left|\mathbf{r}\cdot\boldsymbol{\varepsilon}\right|a\rangle}{\hbar\omega-E_R^n+i(\Delta_n/2)}\right|^2, \tag{2.32}$$

where α_{f} is the fine structure constant, $E_R^n=E_n-E_a$ are the resonant energies and Δ_n is the energy distribution. For a detailed description and derivation of Eq. 2.32 it is referred to [123, 130].

The matrix elements in Eq. 2.32 can be calculated for a magnetic sample. For this, a quantization axis z parallel to the magnetization direction is defined. This results in the elastic resonant magnetic scattering amplitude expressed by [62, 136]

$$F\left(E\right)=\left(\boldsymbol{\varepsilon}'\cdot\boldsymbol{\varepsilon}\right)G_0+i\left(\boldsymbol{\varepsilon}'\times\boldsymbol{\varepsilon}\right)\hat{\boldsymbol{m}}G_1+\left(\boldsymbol{\varepsilon}'\cdot\hat{\boldsymbol{m}}\right)\left(\boldsymbol{\varepsilon}\cdot\hat{\boldsymbol{m}}\right)G_2, \tag{2.33}$$

where $\hat{\boldsymbol{m}}$ is the unit vector of the magnetization and $G_{0,1,2}$ are the dipole transition matrix elements. The resonant magnetic scattering factor is divided into three independent parts which show separately polarization dependent or independent interactions with respect to the magnetic moments of the sample. The fist term describes the magnetization independent interaction of photons with the electrons of the atom (charge scattering). The second term depends linearly on the magnetic moment, and the polarization dependency reveals that this part can be described analogous to the XMCD effect [62, 126, 127, 137] (see previous section). The third part depends quadratically on the magnetic moment and is given by the X-ray magnetic linear dichroism (XMLD) [138–140]. The XMLD effect is generally much smaller than the XMCD effect [123, 141]. In case of magnetic samples with out-of-plane easy-axis of magnetization the polarization vector $\boldsymbol{\varepsilon}$ is perpendicular to $\hat{\boldsymbol{m}}$ and the XMLD effect vanishes ($\boldsymbol{\varepsilon}\cdot\hat{\boldsymbol{m}}=0$). A non-vanishing XMLD contribution arises if a small in-plane component of $\hat{\boldsymbol{m}}$ exists due to a tilted sample with respect to the beam or a slightly canted magnetization direction of the sample. However, this contribution is usually small and negligible due to the quadratic dependence on $\hat{\boldsymbol{m}}$ [68, 72, 142].

The relation between X-ray scattering and X-ray absorption given in Eq. 2.31 can also be found for magnetic samples from the imaginary part of the elastic resonant magnetic scattering amplitude $F\left(E\right)$ (Eq. 2.33)

$$\begin{aligned} \mathrm{Im}\left[F\left(E\right)\right] = f_2^{\pm}\left(E\right) &= \frac{1}{2\lambda r_0}\sigma_{\pm}^{abs}\left(E\right), \\ f_2^{\pm}\left(E\right) &= f_0 \pm f_{\mathrm{m}}, \end{aligned} \tag{2.34}$$

where k_0 is the unit vector of the X-ray propagation direction. Equation 2.34 represents the case of incident circular polarization, where ($\pm$) corresponds to left- and right-circular polarization. The unit vector $\hat{\boldsymbol{m}} = \varepsilon_z$ is considered to be parallel to the surface normal of the magnetic sample. Hence, the XMLD contribution vanishes (see above). In Eq. 2.34, f_0 represents the resonant scattering at the charge distribution and f_{m} is related to the polarization-dependent XMCD effect.

Using Eq. 2.34 and Eq. 2.25, the linear absorption coefficient can be described in terms of the imaginary part of the resonant scattering factor by

$$\mu_x^{\pm}(E) = \rho_a \sigma_{\pm}^{abs}(E) = \rho_a 2\lambda r_0 f_2^{\pm}(E) = \rho_a 2\lambda r_0 \left(f_0 \pm f_{\mathrm{m}}\right). \tag{2.35}$$

The experiments performed in this thesis are all carried out at the resonances of the ferromagnetic transition metal cobalt and thus the strong resonant magnetic scattering is dominant [62]. Resonant charge scattering can distort the resonant magnetic scattering signal if both exhibit similar length scales and thus coincide in reciprocal space [65, 137]. However, the charge contribution to the resonant scattering factor can be assumed to be constant and can be neglected for the magnetic sample systems used in this thesis, as correlations of charge inhomogeneities on the length scale of the magnetic domains ≈ 100 nm do not exist in these samples (grain sizes ≤ 10 nm [143, 144]).

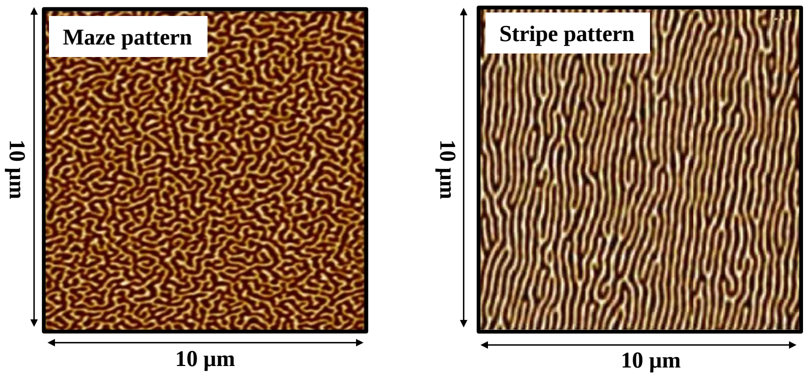

Figure 2.6: Magnetic force microscopy (MFM) images of magnetic domain patterns from a Co/Pt multilayer sample with out-of-plane easy-axis of magnetization. The left image represents the case of a disordered maze-like domain pattern and the right image of a well-ordered stripe domain pattern. The right image is taken from [145].

2.2.4 Resonant magnetic X-ray scattering at magnetic domain patterns

In the following, the resonant magnetic X-ray scattering intensity obtained from magnetic domain patterns of ferromagnetic samples with out-of-plane easy-axis of magnetization is discussed. The discussion is restricted to the case of small-angle X-ray scattering (SAXS) in transmission geometry.

Figure 2.6 illustrates magnetic force microscopy (MFM) images of two kinds of magnetic domain patterns, the disordered maze-like pattern consisting of a large variation of domain sizes and the well-ordered stripe domain pattern consisting of almost a single domain size. The domain pattern can be seen as an alternating series of up/down (light/dark areas in the MFM images) domains separated by magnetic domain walls. A detailed description of the formation of magnetic domain patterns is given in section 5.4.1.

A sketch of the geometry for magnetic small-angle scattering from these samples is shown in Fig. 2.7. The incident X-ray radiation is scattered by the magnetic sample, i.e., the magnetic domain pattern, and the scattering intensity is recorded by a CCD detector. The momentum transfer $\boldsymbol{Q} = \boldsymbol{k} - \boldsymbol{k}'$ is given by the difference of the incident $\boldsymbol{k}$ and scattered wave vector $\boldsymbol{k}'$, where for elastic scattering $|\boldsymbol{k}| = |\boldsymbol{k}'| = 2\pi/\lambda$. In the experimental geometry, the modulus of the momentum transfer is expressed by

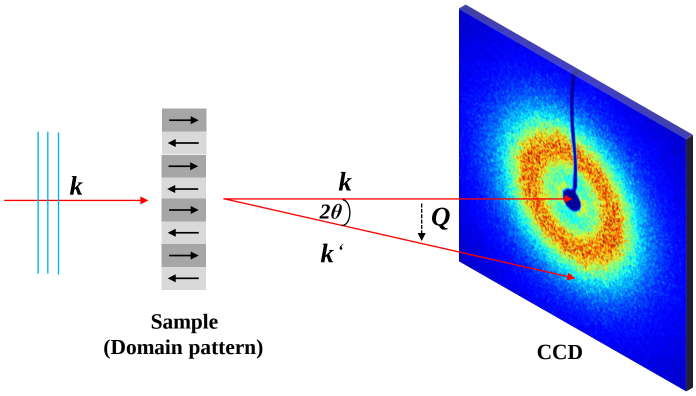

Figure 2.7: Illustration of small-angle scattering (SAXS) in transmission geometry. The momentum transfer $\boldsymbol{Q} = \boldsymbol{k}' - \boldsymbol{k}$ is given by the incident $\boldsymbol{k}$ and scattered wave vector $\boldsymbol{k}'$. The scattering from a magnetic maze domain pattern (see Fig. 2.6) shows an isotropic donut-shaped diffraction pattern.

$$|\boldsymbol{Q}| = \frac{4\pi}{\lambda} \sin\theta, \tag{2.36}$$

where 2θ is the angle between the incident and scattered wave.

In the most ordered case, the domain pattern can be described by an ensemble of identical scatterers, i.e., magnetic domains with equal width. In such systems, the magnetic domain pattern (magnetization profile) can be described by a one-dimensional model by [146, 147]

$$m\,(x) = \sum_{n=-\infty}^{\infty} f(x - nd) = f_{\mathrm{m}}(x) * \sum_{n=-\infty}^{\infty} \delta\,(x - nd), \tag{2.37}$$

where $f_{\mathrm{m}}(x)$ represents the magnetic unit cell consisting of an up and down domain pair. The sum of delta functions $\delta\,(x - nd)$ represents the basic lattice with domain period d. Hence, the complete domain pattern is expressed by a convolution of the magnetic unit cell with a lattice structure. The Fourier transform of the convolution product in Eq. 2.37 is the product of the Fourier transforms of both constituents and Eq. 2.37 is transformed to

$$\begin{aligned} F_{\mathrm{m}}(Q) &= f_{\mathrm{m}}(Q) \cdot \sum_{n=-\infty}^{\infty} \exp(-iQnd) \\ &= f_{\mathrm{m}}(Q) \cdot \frac{2\pi}{d} \sum_{n=-\infty}^{\infty} \delta\left(Q - n\frac{2\pi}{d}\right) \end{aligned} \tag{2.38}$$

where $f_{\mathrm{m}}(Q)$ is the form factor, which is thus the Fourier transform of the magnetic unit cell or shape of the scattering object. Equation 2.38 shows that a comb of delta functions in real space is also a comb of delta functions in phase space separated by the inverse period $2\pi/d$. Using Eq. 2.38 the SAXS intensity can be expressed by

$$I(Q) = |F_{\mathrm{m}}(Q)|^2 = |f_{\mathrm{m}}(Q)|^2 \cdot \left| \sum_{n=-\infty}^{\infty} \exp(-iQnd) \right|^2 = |f_{\mathrm{m}}(Q)|^2 S(Q). \tag{2.39}$$

$S(Q)$ is the so-called structure factor and accounts for the spatial configuration of the scattering objects.

In case of disordered magnetic maze domain patterns, it is not possible to describe the domain pattern by a single domain size for a magnetic unit cell and also not through a periodic magnetic lattice due to the large variation of domain sizes.

In general, the magnetic scattering intensity $I(\boldsymbol{Q})$ is expressed by the squared modulus of the Fourier transform of the scattering amplitudes F_n from the lattice sites n with position vector $\mathbf{r}_n$ [72, 142, 146, 148]

$$I(\boldsymbol{Q}) \propto \left| \sum_n F_n \exp(-i\boldsymbol{Q}\mathbf{r}_n) \right|^2 = \left| \int_V F(\mathbf{r}) \exp(i\boldsymbol{Q}\mathbf{r})\, d\mathbf{r} \right|^2, \tag{2.40}$$

where the scattering amplitude F_n is given by Eq. 2.33. All lattice sites within a magnetic domain give the same scattering amplitude and hence the sum in Eq. 2.40 runs over effective domains instead of single scatterers [142, 148]. In the second expression of Eq. 2.40, the integral ranges over the total volume V of the sample. In the resonant case with incident circularly polarized X-ray radiation the last term (XMLD) in Eq. 2.33 cancels out ($\boldsymbol{\epsilon} \cdot \hat{\boldsymbol{m}} = 0$). Additionally, the charge contribution will be neglected in the following (see section 2.2.3). The scattering intensity can thus be expressed by [63, 73, 148]

$$I(\boldsymbol{Q}) \propto \left| \int_V (\boldsymbol{k}_0 \cdot \hat{\boldsymbol{m}}(\mathbf{r}))\, G_1 \exp(i\boldsymbol{Q}\mathbf{r})\, d\mathbf{r} \right|^2 \propto \left| \int_A m_{\mathrm{z}}(\mathbf{r}) \exp(i\boldsymbol{Q}\mathbf{r})\, d\mathbf{r} \right|^2, \tag{2.41}$$

where $\boldsymbol{k}_0$ is the unit vector in the propagation direction of the incident X-ray. $\boldsymbol{k}_0$ replaces the cross product of the polarization unit vectors $(\boldsymbol{\varepsilon}' \times \boldsymbol{\varepsilon})$ in Eq. 2.33 [123]. In Eq. 2.41 the second expression results from the assumptions that $|\hat{\boldsymbol{m}}|$ = constant throughout the magnetic sample and that the X-ray radiation propagates along the z-direction, i.e., along the sample depth. A denotes the sample area and $-1 < \ m_{\mathrm{z}}(\mathbf{r}) < \ 1$ represents the local out-of-plane component of the magnetization, i.e., a two-dimensional magnetic domain pattern. From Equation 2.41 it follows that the magnetic scattering intensity $I(\boldsymbol{Q})$ is proportional to the squared modulus of the two-dimensional Fourier transform of the magnetic domain pattern $m_{\mathrm{z}}(\mathbf{r})$.

Spatial coherence and X-ray resonant magnetic scattering

So far, the spatial coherence properties of the X-ray radiation have been excluded from the discussion of the X-ray resonant magnetic scattering intensity. The following discussion provides a brief introduction and describes the effects that arise due to different degrees of spatial coherence.

In the last section it has been shown that the scattering intensity is the squared modulus of the Fourier transform of the magnetic domain pattern $m_z(\mathbf{r})$. Taking account of the spatial coherence properties of the X-ray beam, the X-ray scattering intensity can be rewritten as [90, 146, 149, 150]

$$\begin{aligned} I(\boldsymbol{Q}) &\propto \int_{-\infty}^{\infty}\int_{-\infty}^{\infty} \Gamma(\mathbf{r}_1, \mathbf{r}_2)\, m_z(\mathbf{r}_1)\, m_z{}^*(\mathbf{r}_2) \mathrm{e}^{(-i\boldsymbol{Q}(\mathbf{r}_1-\mathbf{r}_2))} d\mathbf{r}_1 d\mathbf{r}_2 \\ &\overset{\Delta\mathbf{r}=\mathbf{r}_1-\mathbf{r}_2}{\propto} \int_{-\infty}^{\infty} \left\{ \int_{-\infty}^{\infty} \Gamma(\mathbf{r}_1, \mathbf{r}_1-\Delta\mathbf{r})\, m_z(\mathbf{r}_1)\, m_z{}^*(\mathbf{r}_1-\Delta\mathbf{r}) d\mathbf{r}_1 \right\} \mathrm{e}^{(-i\boldsymbol{Q}\Delta\mathbf{r})} d\Delta\mathbf{r}, \end{aligned} \tag{2.42}$$

where $\Gamma(\mathbf{r}_1, \mathbf{r}_1 - \Delta\mathbf{r}) = \gamma(\Delta\mathbf{r})\sqrt{I(\mathbf{r}_1)}\sqrt{I(\mathbf{r}_1 - \Delta\mathbf{r})}$ is the mutual coherence function (see Eq. 2.4) in the quasi-monochromatic approximation, characterizing the spatial coherence properties of the X-ray radiation (see section 2.1). As described in section 2.1.2, $\gamma(\Delta\mathbf{r})$ is directly related to the transverse coherence length Ξ of the X-ray beam. The inner integral in Eq. 2.42 reveals the autocorrelation function of the magnetic domain pattern given by

$$P(\Delta\mathbf{r}) = \int_{-\infty}^{\infty} m_z(\mathbf{r}_1)\, m_z{}^*(\mathbf{r}_1 - \Delta\mathbf{r}) d\mathbf{r}_1. \tag{2.43}$$

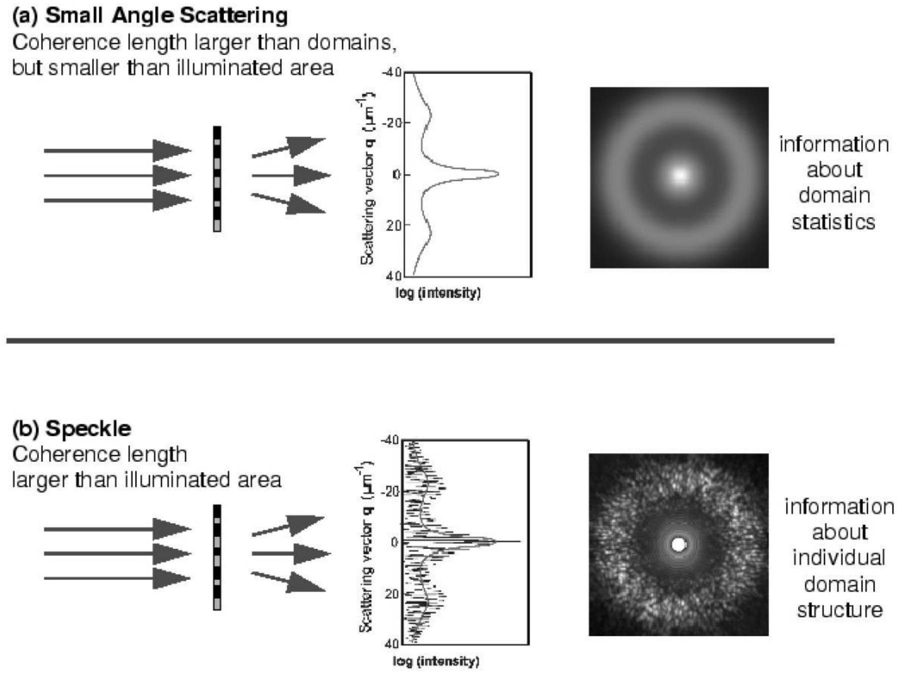

Figure 2.8: Difference between incoherent and coherent X-ray resonant magnetic scattering. The upper panel shows incoherent illumination of a magnetic maze domain pattern. In this case the transverse coherence length is much smaller than the illuminated area but larger than the spatial correlation length of the magnetic domains. Only the intensities of the scattering object are summed which results in an averaging of the properties over the illuminated area. The lower panel shows fully coherent illumination with a transverse coherence length larger than the illuminated area. The latter results in the emergence of a magnetic speckle pattern providing the exact spatial arrangement of the magnetic domains. Hence, the speckle pattern can be seen as a unique fingerprint of the magnetic domain pattern. The image is taken from [134].

$P(\Delta\mathbf{r})$ is called Patterson function or Patterson map of the magnetic domain pattern [151].

Equation 2.42 shows that the mutual coherence function acts as a weighting factor for the magnetic domain pattern used to calculate the autocorrelation function. The magnetic scattering intensity is according to that the Fourier transform of the autocorrelation function of the weighted magnetic domain pattern [149, 152].

Magnetic maze domain patterns of magnetic samples with out-of-plane easy axis of magnetization display an isotropic donut-shaped diffraction pattern, as it can be seen in Fig. 2.7 and Fig. 2.8).

Incoherent illumination of a magnetic domain pattern, i.e., the transverse coherence length of the X-ray radiation is much smaller than the illuminated area ($\sigma >> \xi_{\mathrm{T}}$; $\gamma(\Delta\mathbf{r})$ is almost zero), but larger than the correlation length of the magnetic domains, results in an averaging of the properties over the illuminated area. The diffraction pattern resembles an ensemble average over all existing domain size variations (domain periods) (see Fig. 2.8). The occurring maximum intensity of the ring structure corresponds to the mean domain size (domain period) in reciprocal space and the width of the intensity profile is related to the spatial in-plane correlation length.

Fully coherent illumination, i.e., the transverse coherence length is much larger than the illuminated area ($\xi_{\mathrm{T}} >> \sigma$, $\gamma(\Delta\mathbf{r}) = 1$), causes constructive and destructive interferences between all wavefronts from the individual scatterers of the sample. The obtained diffraction pattern exhibits additional small grainy features which are called speckles. The individual speckles have an angular width corresponding to the size of the illuminated area. The so-called speckle size is given by $S_{x,y} = \lambda z / d_{x,y}$, where z is the distance between the sample and the detector and $d_{x,y}$ is the beam size (FWHM) on the sample [120, 153]. Hence, the speckle itself depends on the size of the illuminated area, but contains no information about the magnetic domain structure. However, the arrangement of the speckles reflects a particular realization or spatial arrangement of the domain structure and can be seen as a unique fingerprint of the magnetic domain pattern. Slight changes within the domain pattern affect the complete speckle pattern.

In the partially coherent case, i.e., $\sigma \sim \xi_{\mathrm{T}}$ ($0 < \gamma(\Delta\mathbf{r}) < 1$), the fully coherent speckle pattern is blurred out and the contrast or visibility of the speckles is reduced [150, 154, 155].

The properties of a speckle pattern are in general discussed in terms of statistics. In case of partially coherent illumination, the speckle pattern can be seen as a sum of M_c statistically independent individual speckle patterns each with fully coherent illumination. The probability density function for the intensities, i.e., the distribution of intensities within the speckle pattern, is given by the gamma distribution [91, 156]

$$p_s(I) = \frac{{M_c}^{M_c} I^{M_c - 1}}{\Gamma(M_c)\langle I \rangle^{M_c}} \exp\left(-\frac{M_c I}{\langle I \rangle}\right), \tag{2.44}$$

where Γ is the gamma function and $\langle I \rangle$ is the mean intensity. The probability density function can be obtained from the speckle pattern by generating a histogram of the intensities. An important quantity of speckle statistics is the speckle contrast C, which can be seen as the visibility of the intensity variations within the speckle pattern, i.e., the normalized variance of intensity fluctuations. It can be expressed by [89, 91, 156, 157]

$$C = \frac{\sigma_I}{\langle I \rangle} = \frac{(\langle I^2 \rangle - \langle I \rangle^2)^{1/2}}{\langle I \rangle} = \frac{1}{\sqrt{M_c}}. \tag{2.45}$$

The speckle contrast is directly connected to the parameter M_c and provides information about the degree of coherence of the illuminating beam. It equals one for fully coherent ($M_c = 1$) and zero for incoherent illumination ($M_c \to \infty$).

3

COHERENT X-RAY SCATTERING EXPERIMENTAL SETUP AND SAMPLE FABRICATION

The experiments presented in this thesis were performed at the soft X-ray beamline P04 at the PETRA III storage ring at DESY in Hamburg. The beamline parameters and optical elements are briefly discussed (section 3.1). Subsequently, the coherent X-ray scattering experimental setup used for the experiments performed in this thesis is described (section 3.2). At the end, the sample fabrication procedure is briefly set out (section 3.3).

3.1 Soft X-ray beamline P04 at PETRA III

The soft X-ray beamline P04 is equipped with a 5 m long APPLE-II-type undulator consisting of $N = 72$ periods. The beamline delivers X-rays with variable polarization in the first harmonic and energies ranging from 250 to 3000 eV ($\lambda = 0.4$ nm $- 5$ nm) [112]. So far, only circular polarization is available, which is sufficient for the experiments performed in this thesis. The beamline allows for measurements using 100 % circular polarization with an integral photon flux of $P_{\text{flux}} > 10^{15}$ photons/s on the sample at a resolving power of $\lambda/\Delta\lambda = 10^4$. Figure 3.1 shows the P04 beamline setup. The emitted X-ray radiation from the undulator first passes two pairs of beam-defining apertures that are 27.9 m away from the source. With appropriate beam-defining openings the coherent volume can be selected from the beam (see section 2.1.5). The beam is then directed to a plane mirror/varied-line space (VLS) plane grating (PM/PG-U) unit, where the groove density at the center of the grating is 1200 lines/mm. The VLS grating focuses the beam in vertical direction into the plane of an exit aperture (EXSU). Due to angular dispersion the beam gets spectrally

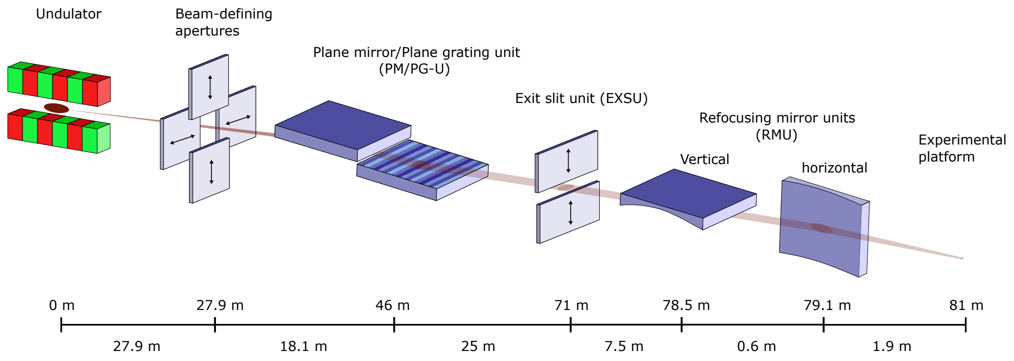

Figure 3.1: The P04 beamline setup composed of the undulator, beam-defining apertures, plane mirror/varied line-space plane grating unit, exit aperture and refocusing mirrors (KB-mirrors). The X-ray beam emitted from the undulator first passes two pairs of beam-defining apertures. Subsequently, the beam is directed to a plane mirror/VLS grating unit. The VLS grating focuses the beam in vertical direction into the plane of the exit aperture, where the beam is monochromatized. Refocussing mirror units for the horizontal and vertical direction focus the beam to the experimental platform.

separated. The exit aperture monochromatizes the beam by reducing the spectral bandwidth $\Delta\lambda$, which can be tuned by adjusting the vertical exit aperture opening. As a consequence, the resolving power $\lambda/\Delta\lambda$ and thus the longitudinal coherence length ξ_{L} can be increased. The last optical elements are two refocusing mirror units (RMU) for the horizontal and vertical direction, which are Kirkpatrick-Baez (KB) mirrors (plane-elliptical mirrors). The beam can be focused to a minimum beam size of 10 μm (FWHM) in horizontal and vertical direction at a focal distance of 1.9 m and 2.5 m, respectively. The vertical focal beam size depends on the exit aperture opening ($\approx 1/3$ of the exit slit size), but cannot be tuned to smaller sizes than 10 μm.

3.2 X-ray scattering and holographic imaging endstation

The experimental setup is specifically designed for coherent small-angle X-ray scattering (SAXS) and X-ray holographic imaging (XHM) experiments at the P04 beamline at the storage ring PETRA III (DESY). The setup is conceived to enable an alignment of the entire setup (setup axis) with respect to the optical axis of the beamline with

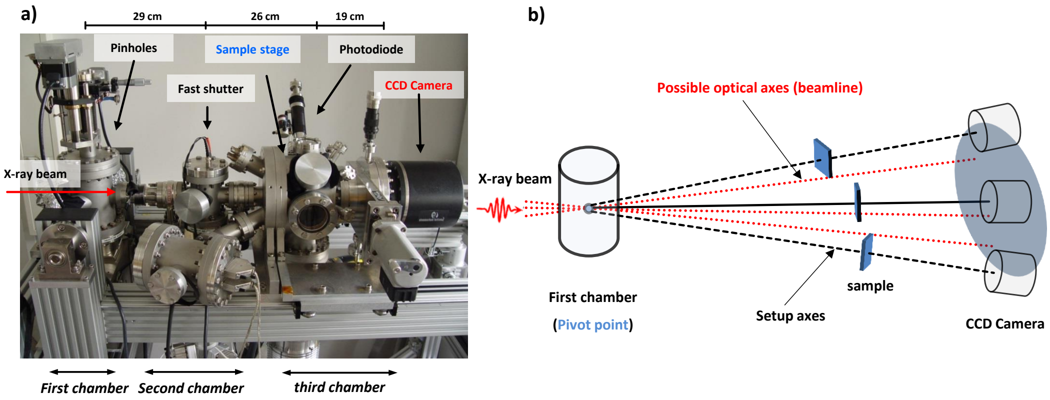

Figure 3.2: a) Image of the coherent X-ray scattering and X-ray holographic imaging setup designed for the P04 beamline at PETRA III (DESY) in Hamburg. The setup consists of three chambers. The X-ray beam coming from the left passes through a pinhole with variable diameter (first chamber), which selects the center part of the beam and ensures a high coherent volume of the beam. A fast shutter located 29 cm downstream of the pinhole is used to set the exposure time for the experiments (second chamber). 26 cm downstream of the fast shutter the beam is scattered by the sample and the scattered X-rays are detected by a CCD camera (sample-detector distance = 19 cm, third chamber). b) The second and third chamber are fixed with respect to each other and can be moved on a conical section with respect to the first chamber to align the setup (setup axis, black dashed line) to the optical axis of the beamline (red dashed lines). The blue ellipse corresponds to the base area of the cone.

sub-micrometer accuracy. It is subdivided into three vacuum chambers (see Fig. 3.2), where each can be pumped separately with a high vacuum pump. The first chamber is fixed in space and the other two chambers, which are fixed with respect to each other, can be moved on a conical section with respect to the first one due to a horizontal and vertical pivot suspension (see Fig. 3.2). The pivot point is set to the center of the first chamber, where the pinhole is located. This setup ensures normal and axial alignment of all optical components independent of beam angle. Additional circular apertures with 2 mm diameter with the frame coated with fluorescent Yttrium Aluminate Nanopowder ($Y_3Al_5O_{12} : Ce$) positioned between the chambers are used for a coarse alignment of the setup with respect to the beam (optical axes). A conical bore with a setting angle of 30° within the apertures suppresses reflections in the direction of the optical axes.

Inside the first chamber, circular apertures with variable diameters of 20 μm, 30 μm, 40 μm, 100 μm and 1 mm can be placed to the position of the beam axis using a manipulator. Its purpose is to limit the beam size to a dimension comparable

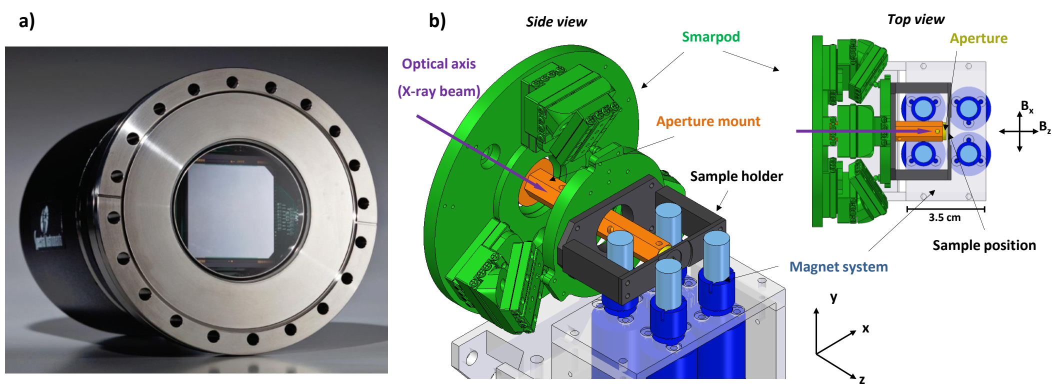

Figure 3.3: a) Image of the CCD camera from Spectral Instruments. b) Sketch of the arrangement of the Smarpod (green), the magnet system (blue) and the sample holder (black). The beam (purple arrow) is first transmitted through an elongated aperture holder with a 6 mm inner diameter. Optionally, a beam-defining aperture or a holographic mask can be mounted on the holder. Subsequently, the beam is scattered by the sample mounted on the sample holder, which in turn is attached on a piezoelectrically driven positioning system. The sample is placed at the center of the magnet system, which provides out-of-plane and in-plane fields up to ±150 mT.

to the transverse coherence length to ensure a coherent beam and to define the illuminated area on the sample [86, 158]. Inside the second chamber, a fast shutter[1] is placed to set the exposure time for the experiments. It consists of a circular aperture with 6 mm diameter and enables exposure times down to ≈ 4 ms using a Pt-Ir shutter blade. Repetition rates up to 2 Hz can be set. Inside the third chamber the magnetic samples are mounted on an aluminum sample holder, which is attached on a piezoelectrically driven positioning system[2] with nanometer accuracy (see Fig. 3.3). It enables positioning of the sample in all three dimensions with travel ranges of ±20 mm in X- and Y-direction and ±10 mm in Z-direction from its zero position. In addition, the sample can be tilted with angles of ±20° about the X- and Y-axis and ±35° about the Z-axis. Optionally, a beam-defining aperture or a holographic mask for holographic imaging experiments can be mounted on an aperture holder in front of the sample.

The sample is placed at the center of a magnet system, which consists of four rotatable diametrally magnetized NeFeB permanent magnets arranged in a quadrupolar configuration [159, 160]. In-plane and out-of-plane magnetic fields can be set up to ±150 mT. Optionally, a photo-diode located behind the sample position can be

[1] XRS6 Uni-stable X-ray Shutter, Vincent Associates.
[2] Smarpod 110.45, SmarAct GmbH.

used to measure the transmitted beam intensity.

The scattered X-rays are detected by a Peltier-cooled 16 Mpx CCD camera[3] with a pixel size of 15 x 15 μm^2 (Total chip size = 61 x 61 mm^2). The camera has four read-out ports, where read-out speeds can be set up to 2 MHz per port. The camera is protected from the high intensity direct beam by a central beam stop of 1 mm diameter.

3.3 Fabrication of Co/Pt and Co/Pd multilayers

The following section deals with the preparation of Co/Pt and Co/Pd multilayers used for the XRMS experiments. First, the fabrication methods are briefly introduced and the used fabrication parameters are specified. Subsequently, the structure and the fabrication of wedge-shaped multilayer samples used for the experiments in chapter 5 are presented.

In addition, CoPd alloys have been studied. The $Co_{35}Pd_{65}$ alloy films have been fabricated by Dr. Christian Weier from the Peter Grünberg Institut at the Forschungszentrum Jülich. They are grown at room temperature using molecular beam epitaxy (MBE) [161]. The film system is fabricated on a 50 nm thick Si_3N_4 membrane of 100 x 100 μm^2 size. First, a seed layer of 2 nm Pd is grown. On this, 40 nm of $Co_{35}Pd_{65}$ are deposited and finally capped by a 2 nm Pd layer to protect the sample from oxidation under ambient conditions.

3.3.1 ECR- and DC magnetron-sputtering techniques

For the preparation of Co/Pt and Co/Pd multilayers two different sputtering techniques are used. These are the electron-cyclotron resonance (ECR) [162] and the direct current (DC) magnetron sputtering [163] techniques. A detailed description of both techniques can be found in [144, 164, 165]. The fabrication of the Co, Pt, and Pd layers are carried out at room temperature at a base pressure of $1 \cdot 10^{-8}$ mbar. The ECR sputtering technique is used to grow a Pt seed layer for the Co/Pt and Co/Pd multilayer films. Its purpose is to initiate and ensure a pronounced (111) texture for the following Co, Pt, and Pd layers, which are grown by means of DC magnetron

[3] 1100S, Spectral Instruments.

sputtering [166]. This is caused by the higher mobility and energy (30 eV) of the ECR sputtered atoms compared to magnetron sputtering (20 eV) [144]. However, ECR sputtering causes a higher interdiffusion at the interfaces. For ECR sputtering an Ar working pressure of $3.2 \cdot 10^{-4}$ mbar and Ar^{+} ion energies of 1.2 keV are applied and a Pt deposition rate of 0.3 nm/s is obtained. DC magnetron sputtering is performed at $3.4 \cdot 10^{-3}$ mbar and ion energies of 0.3 keV for Co, 0.4 keV for Pd, and 0.5 keV for Pt. The ion current is kept constant at 50 mA for Co and 30 mA for Pt and Pd. The corresponding deposition rates are for Co 0.03 nm/s, for Pd 0.06 nm/s, and for Pt 0.07 nm/s. Investigations have shown that the combined use of an ECR sputtered Pt seed layer, which induces growth on a pronounced textured film, and subsequent DC magnetron sputtered Co, Pd, and Pt layers, which cause improved interfacial properties due to low interdiffusion, maximizes the overall perpendicular magnetic anisotropy of the Co/Pt and Co/Pd films [143, 164, 166].

3.3.2 Preparation and structure of wedge-shaped Co/Pd multilayers

The structural properties and the preparation of the wedge-shaped Co/Pd multilayer films are described in the following.

Figure 3.4 (a) illustrates the Co/Pd sample structure used for the experiments. The film system is fabricated on a 200 nm thick Si_3N_4 membrane of 1500×1500 μm^2 size, which serves as the substrate and allows for X-ray experiments in transmission geometry. First, the seed layer consisting of 4 nm ECR sputtered Pt and 3.5 nm DC magnetron sputtered Pd is grown on the substrate. The 4 nm Pt layer ensures an improved texture and the 3.5 nm Pd layer improved interfacial properties of the seed layer [165]. Studies have revealed that $\geq$ 4 nm of Pt guarantees the maximum obtainable high quality of crystallinity and interfaces [144, 166]. The use of ECR sputtered Pt instead of Pd is intended to provide a better comparability of the Co/Pd multilayers with Co/Pt multi- and single-layers which have been intensively investigated with respect to film structure, growth and magnetic properties [143, 144, 165, 166]. On the seed layer stacking a wedge-shaped multilayer film is grown which consists of an 8-fold Co/Pd bilayer $(Co_{t\text{Å}}/Pd_{10\text{Å}})_8$ where the thickness of each Co single layer is varied from $t_{\mathrm{Co,single}} = 0 - 10$ Å, and the Pd layer thickness

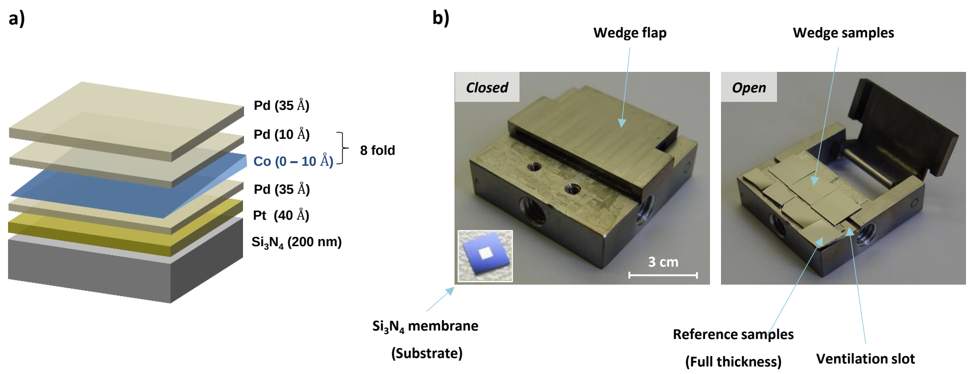

Figure 3.4: a) Layout of the 8-fold wedge-shaped Co/Pd multilayer film. b) Image of the shadow mask used for the fabrication of wedge-shaped Co layers. It consists of an Al sample holder and a Cu wedge flap. The Cu wedge flap can be opened and closed to fabricate plane or wedge-shaped films, respectively. The samples are positioned on a ventilation slot which prevents distortions of the thin substrate due to rapid pressure changes during transfer into and out of the vacuum chamber.

is kept constant[4]. The multilayer is fabricated using DC magnetron sputtering utilizing the penumbra of a shadow mask. An image of the shadow mask is shown in Fig 3.4 (b). It consists of an Al sample holder and a Cu wedge flap. The flap can be opened and closed to allow for a growth of a plane layer (Pd) and a wedge-shaped layer (Co). The shape of the wedge is caused by the penumbra which arises at the edge of the wedge flap during the deposition process. The center of the samples is positioned at the edge of the flap to assure a centered wedge-shaped layer on the substrate. A ventilation slot prevents a distortion of the thin substrate due to rapid pressure changes during transfer into and out of the vacuum chamber. At last, the Co/Pd-multilayer stack is capped by a 3.5 nm Pd layer in order to prevent oxidation of Co under ambient conditions.

[4]The 32-fold ($Co_{0.8nm}/Pt_{1.4nm}$) multilayer used in section 4.3.3 has been fabricated in the same way, except that the Co and Pt layer thicknesses are kept constant and 1 nm Pt instead of 3.5 nm Pd has been used for the seed layer stacking.

4

FOURIER ANALYSIS OF MAGNETIC SPECKLE PATTERNS FOR SPATIAL COHERENCE DETERMINATION

The knowledge of the coherence properties of X-ray radiation from synchrotron radiation sources is essential for many X-ray techniques that require highly coherent X-ray radiation. These techniques are, e.g., coherent diffractive imaging (CDI) [167–170], X-ray holographic imaging (XHM) [69, 171], Fourier transform holography (FTH) [66–68], X-ray ptychography [82, 172–174], and X-ray photon correlation spectroscopy (XPCS) [156, 175, 176]. The degree of spatial and temporal coherence has a strong impact on the performance of these experiments and consequently coherence measurements and optimizations prior to the experiments become important.

The coherence properties are described by the mutual coherence function, as it is given in section 2.1. The following deals with the mutual coherence function and complex degree of coherence in the quasi-monochromatic approximation, which means that the longitudinal coherence length is assumed to be much larger than any path-length difference that occurs in the experiments. Hence, only the spatial coherence is considered, which is characterized by the transverse coherence length of the X-ray beam.

Several techniques exist to determine the spatial coherence properties of X-ray radiation. The model experiment is the Young's double-pinhole or double-slit experiment, which measures the fringe visibility $\nu(\Delta\mathbf{r})$ or complex degree of coherence as a function of slit or pinhole separation $\Delta\mathbf{r}$[1] [80, 95, 120]. To map out the full two-dimensional complex degree of coherence, a series of double pinhole apertures with various separations and spatial orientations is required. The transverse coherence length in these experiments is defined as the pinhole or slit separation at which the

[1]In the quasi-monochromatic approximation and assuming that the intensities incident on each pinhole or slit are equal $\nu(\Delta\mathbf{r}) = (I_{\max} - I_{\min})/(I_{\max} + I_{\min}) = |\gamma(\Delta\mathbf{r})|$.

visibility or modulus of the complex degree of coherence (CDC) drops to a value of 0.6.[2] Based on these experiments, further concepts have been developed utilizing pinholes to measure coherence properties. These are, e.g., the use of uniformly redundant arrays of apertures (URA) and non-redundant arrays of apertures (NRA). The URA is composed of a pseudo-random array of pinholes, such that on a discrete grid all possible pinhole separations occur and do so for an equal number of times [84, 85, 177, 178]. The NRA is composed of an array of double-pinholes in a well defined arrangement, where each pinhole separation occurs only once [79, 179]. Both concepts allow for simultaneous measurement of many Young's double-pinhole experiments in one or two dimensions and thus reduce the expenditure of time to measure the transverse coherence length. Another method to determine the coherence properties is based on the speckle contrast determination of speckle patterns from random scatterers [86, 87, 89]. The obtained speckle contrast characterizes the spatial coherence by one quantity and can be extracted from the speckle pattern with low effort. However, the method does not allow for a direct measurement of the transverse coherence length.

In the following, a method is presented to determine the two-dimensional representation of the modulus of the complex degree of coherence and thus the transverse coherence length of the X-ray radiation directly from a single magnetic speckle pattern. It is based on the analysis of the Fourier transform of a magnetic speckle pattern, that is obtained using X-ray resonant magnetic scattering (XRMS) from a ferromagnetic sample in the multidomain state.

At first, the Fourier analysis method is described and discussed in detail (section 4.1. Subsequently, the Patterson map of a magnetic domain pattern is described, as well as its influence on the performance of the method (section 4.2. In the third section (4.3), two XRMS experiments performed at the P04 beamline at PETRA III (DESY) are presented, where the magnetic speckle pattern from a ferromagnetic $Co_{35}Pd_{65}$ alloy film and a $(Co_{0.8nm}/Pt_{1.4nm})_{32}$ multilayer film are used to extract the transverse coherence lengths. The fourth section (4.4) describes the influence of the speckle intensity and noise contributions on the extracted coherence function and the determined transverse coherence lengths. A Young's double pinhole experiment has been performed to corroborate the obtained results from the Fourier analysis method and is presented in the fifth section (4.5). At the end, the results are concluded and possible further applications of the Fourier analysis method are discussed (4.6).

[2]For a Gaussian CDC this corresponds to a separation equal to the the rms width or standard deviation σ.

4.1 The Fourier analysis method

The Fourier analysis method can be seen as a combination of the URA concept and the speckle analysis method. Within the URA concept, the CDC is obtained from the Fourier transform of the diffraction pattern from a pseudo-random distributed pinhole array (scatterers). For the speckle analysis method, a sample with randomly distributed scatterers (aerogel, colloids, etc.) is used to obtain a speckle pattern. The extracted speckle contrast C (see Eq. 2.45) is determined via calculating the normalized variance of intensity fluctuations within defined regions of the speckle pattern and characterizes the coherence properties of the beam. In the presented Fourier analysis method the CDC (see section 2.1) is obtained from the Fourier transform of a magnetic speckle pattern, that is obtained using X-ray resonant magnetic scattering from a magnetic maze domain pattern, having a broad distribution of domain sizes (magnetic scatterers). The advantage of this method is that the magnetic speckle patterns obtained from X-ray resonant magnetic scattering experiments, that are acquired during the investigation of magnetic samples, can be directly used to get additional access to the spatial coherence properties of the incident X-ray beam. Thus, no additional expensively manufactured double-pinhole or pinhole arrays have to be used to determine the coherence prior to these experiments.

The distribution of scattering intensity in an X-ray resonant magnetic scattering experiment in the detector plane is described by Eq. 2.41 and Eq. 2.42 and is given by the modulus square of the two-dimensional Fourier transform of the magnetic density of the sample $m_z(\mathbf{r})$, i.e., the magnetic domain pattern. The inverse Fourier transform of the magnetic speckle pattern yields [149, 152, 180]

$$\begin{aligned} I(\Delta\mathbf{r}) &\propto \left|\mathcal{F}^{-1}\left(\left|\mathcal{F}\left(m_z(\mathbf{r})\right)\right|^2\right)\right|, \\ &= \left|\int_{-\infty}^{\infty} \Gamma\left(\mathbf{r}_1, \mathbf{r}_1 - \Delta\mathbf{r}\right) m_z\left(\mathbf{r}_1\right) {m_z}^*\left(\mathbf{r}_1 - \Delta\mathbf{r}\right) d\mathbf{r}_1\right|. \end{aligned} \tag{4.1}$$

Within the framework of the Gaussian Schell-model, the complex degree of coherence $\gamma(\mathbf{r}_1, \mathbf{r}_2)$ and the beam intensity distribution $I(\mathbf{r})$ are assumed to be Gaussian functions and the complex degree of coherence depends only on the separation of any two point pairs within the beam ($\gamma(\mathbf{r}_1, \mathbf{r}_2) = \gamma(\mathbf{r}_1 - \mathbf{r}_2) = \gamma(\Delta\mathbf{r})$). Consequently, the source is assumed to be spatially uniform (see section 2.1.2). Substitution of Eq. 2.4

into Eq. 4.1 yields

$$I(\Delta\mathbf{r}) \propto |\gamma(\Delta\mathbf{r})| \left| \int_{-\infty}^{\infty} I(\mathbf{r}_1)^{1/2} m_z(\mathbf{r}_1) I(\mathbf{r}_1 - \Delta\mathbf{r})^{1/2} m_z{}^*(\mathbf{r}_1 - \Delta\mathbf{r}) d\mathbf{r}_1 \right|. \tag{4.2}$$

Equation 4.2 expresses that the Fourier transformed magnetic speckle pattern is the product of the modulus of the complex degree of coherence and the modulus of the product autocorrelation function of the magnetic domain pattern and the intensity distribution of the illuminating X-ray beam. It has been verified in simulations that the product autocorrelation function can be separated into the product of the Patterson function of the magnetic domain pattern and the autocorrelation function of the beam intensity distribution. The latter is feasible in the presented case, where the magnetic domain pattern is a spatially fast varying function and the intensity distribution a spatially slow varying function. The applicability of the separation has been examined using simulated data for typical length scales of magnetic domain patterns and beam intensity distributions used for magnetic small-angle X-ray scattering experiments, which reveals a good agreement. It follows that Eq. 4.2 can be expressed by

$$I(\Delta\mathbf{r}) \propto |\gamma(\Delta\mathbf{r})| \, |K(\Delta\mathbf{r})| \, |P_m(\Delta\mathbf{r})| \, . \tag{4.3}$$

$K(\Delta\mathbf{r})$ represents the autocorrelation function of the beam intensity distribution. It will be demonstrated in section 4.2 that the Patterson function $P_m(\Delta\mathbf{r})$ of a disordered magnetic maze domain pattern can be described by a constant except in the vicinity of the central region and thus contributes to Eq. 4.3 only by a multiplicative factor. Consequently, Eq. 4.3 can be used to deduce the two-dimensional representation of the complex degree of coherence $\gamma(\Delta\mathbf{r})$ in a particularly easy way, which in turn can be utilized to determine the transverse coherence lengths (ξ_{T}) of the incident X-ray beam. For this, the Fourier transformed magnetic speckle pattern is normalized by the autocorrelation function of the beam intensity distribution and subsequently by its maximum value at zero separation. The latter normalization is performed to cancel out the multiplicative factor of the Patterson function.

It is possible to describe the above analysis also in the so-called statistically stationary model, which is a limit of the Gaussian Schell-model, where the illuminating field components are uniform and planar [90]. In this model, the mutual coherence function depends only on the separation $\Delta\mathbf{r}$ of the coordinates and the beam intensity distribution is only considered by a constant intensity I_0 ($\Gamma(\mathbf{r}_1, \mathbf{r}_1 - \Delta\mathbf{r}) = I_0\gamma(\Delta\mathbf{r})$).

The statistically stationary model is often used in the literature due to its simple form, which is beneficial for analysis purposes [83, 86, 87, 90, 181]. In this model, the mutual coherence function can be rewritten as ($\Gamma(\mathbf{r}_1, \mathbf{r}_1 - \Delta\mathbf{r}) = \Gamma(\Delta\mathbf{r})$) and Eq. 4.1 yields [149]

$$\begin{aligned} I(\Delta\mathbf{r}) &\propto |\Gamma(\Delta\mathbf{r})| \left| \int_{-\infty}^{\infty} m_z(\mathbf{r}_1)\, m_z{}^*(\mathbf{r}_1 - \Delta\mathbf{r}) d\mathbf{r}_1 \right|, \\ &\propto |\Gamma(\Delta\mathbf{r})| \, |P_m(\Delta\mathbf{r})| = I_0 \, |\gamma(\Delta\mathbf{r})| \, |P_m(\Delta\mathbf{r})| \,. \end{aligned} \tag{4.4}$$

Equation 4.4 shows, similar to Eq. 4.3, that the Fourier transform of the magnetic speckle pattern is given by the product of the modulus of the complex degree of coherence of the illuminating beam and the modulus of the Patterson function of the magnetic domain pattern, multiplied simply by I_0. This result is similar to the one obtained from the URA concept[3], where the Fourier transform of the coherent diffraction pattern of a pseudo-random pinhole array results in the product of the CCD with the known autocorrelation function of the pinhole array [83–85, 178]. In [84] the authors state that the autocorrelation function should be ideally flat except for a very sharp peak at the center to obtain reliable results. This property has been found for the autocorrelation function of spatially disordered magnetic maze domain patterns, as will be demonstrated in the following section.

4.2 Patterson function of magnetic domain patterns

4.2.1 Overview and properties

The Patterson function is defined as the convolution or autocorrelation function of a function $f(\mathbf{r})$.

$$\begin{aligned} P(\Delta\mathbf{r}) &= \int_{-\infty}^{\infty} f^*\left(\mathbf{r}'\right) f\left(\mathbf{r}' - \Delta\mathbf{r}\right) d\mathbf{r}', \\ &= f^*(\mathbf{r}) * f(-\mathbf{r}), \\ &= f(\mathbf{r}) \otimes f(\mathbf{r}). \end{aligned} \tag{4.5}$$

[3]Mostly analyzed in terms of the statistically stationary model.

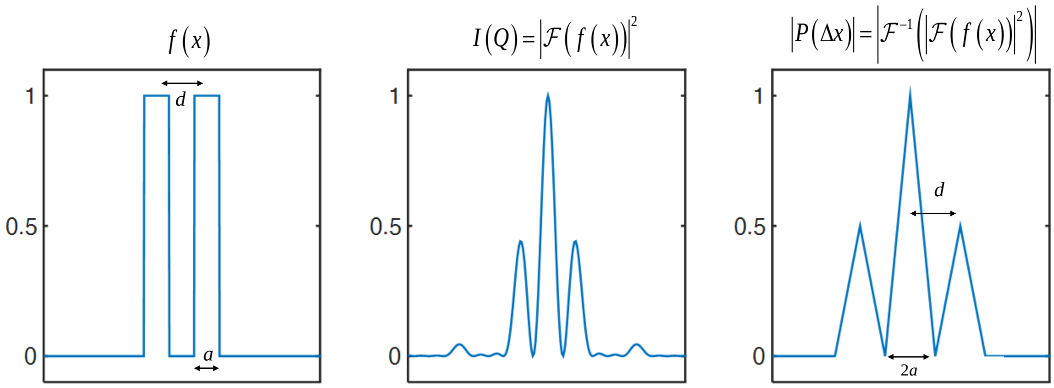

Figure 4.1: Fourier transform relationship between a double-slit structure and its corresponding Fringe pattern and Patterson function in one dimension. $I(Q)$ and $|P(\Delta x)|$ have been normalized by their maximum values.

In the field of crystallography, $f(\mathbf{r})$ is the electron density throughout the crystal. In the presented case, $f(\mathbf{r})$ is the magnetic density $m_z(\mathbf{r})$ or magnetic domain pattern, which varies as a function of the local out-of-plane component of the magnetization due to the X-ray magnetic circular dichroism (see section 2.2.2).

The main feature of the Patterson function is that its Fourier transform is the diffracted intensity[4]

$$\begin{aligned} I(\boldsymbol{Q}) &= \int_{-\infty}^{\infty} P(\Delta\mathbf{r})\, e^{-i\boldsymbol{Q}\mathbf{r}} d\mathbf{r}, \\ &= \mathcal{F}(P(\Delta\mathbf{r})). \end{aligned} \tag{4.6}$$

and by performing the inverse Fourier transform is follows

$$P(\Delta\mathbf{r}) = \mathcal{F}^{-1}(I(\boldsymbol{Q})). \tag{4.7}$$

Another important relationship between $P(\Delta\mathbf{r})$ and $f(\mathbf{r})$ is given by the autocorrelation theorem of the Fourier transform

$$I(\boldsymbol{Q}) = \mathcal{F}^*(f(\mathbf{r}))\,\mathcal{F}(f(\mathbf{r})) = |\mathcal{F}(f(\mathbf{r}))|^2 = \mathcal{F}(P(\Delta\mathbf{r})). \tag{4.8}$$

$$P(\Delta\mathbf{r}) = \mathcal{F}^{-1}\left(|\mathcal{F}(f(\mathbf{r}))|^2\right). \tag{4.9}$$

[4]Here, fully coherent illumination is assumed.

As a consequence, the Patterson function can be computed from the function $f(\mathbf{r})$ using two Fourier transforms. Figure 4.1 illustrates the Fourier transform relationships given by Eq. 4.8 and Eq. 4.9 for a double-slit structure in one dimension. The function $f(x)$ represents the transmission function of a double slit (rectangle functions). The modulus square of the Fourier transform of $f(x)$ illustrates a synthetic one-dimensional fringe pattern $I(Q)$. It is described by a sinc^2 function modulated by a constant frequency, which corresponds to the slit spacing d. $P(\Delta x)$ is the autocorrelation function of the double slit structure and can be described by triangle or Λ functions. The central Λ function represents the self-correlation of both rect functions and the two side Λ functions with half the amplitude represent the cross-correlation terms. The distance d between the peak position of the center Λ function and the peak position of the side Λ functions corresponds to the spacing of the slits. The width of all Λ functions is given by twice the slit width.

4.2.2 Application to magnetic domain patterns

In the last chapter it has been demonstrated that the CDC can be extracted from the Fourier transform of a magnetic speckle pattern (see Eq. 4.3 and Eq. 4.4). For this, it is important to know the characteristics of the Patterson function of a magnetic domain pattern, similar to the case of the URA concept. The autocorrelation function of the pinhole array in the URA concept is well known, although the pinholes are pseudo-randomly distributed[5]. However, the exact autocorrelation function of a magnetic domain pattern is not easily accessible, especially in case of a disordered maze domain pattern with a large amount of domain size variation. Real-space images obtained from high-resolution magnetic imaging techniques have to be recorded at the exact position of the illuminating beam together with an appropriate size to get a sufficient domain pattern to calculate the exact Patterson function. This would be impractical and hardly achievable.

1D Patterson function

The general properties of the Patterson function $P_m(\Delta\mathbf{r})$ from magnetic domain patterns $m_z(\mathbf{r})$ can be studied by modeling one-dimensional magnetic domain patterns with different domain size distributions. For this, an alternating sequence of $m_z = -1$

[5] URA patterns can be calculated using an algorithm described by [177] and manufactured with optical lithography techniques. The autocorrelation function as well as the URA coherent diffraction pattern can be easily simulated.

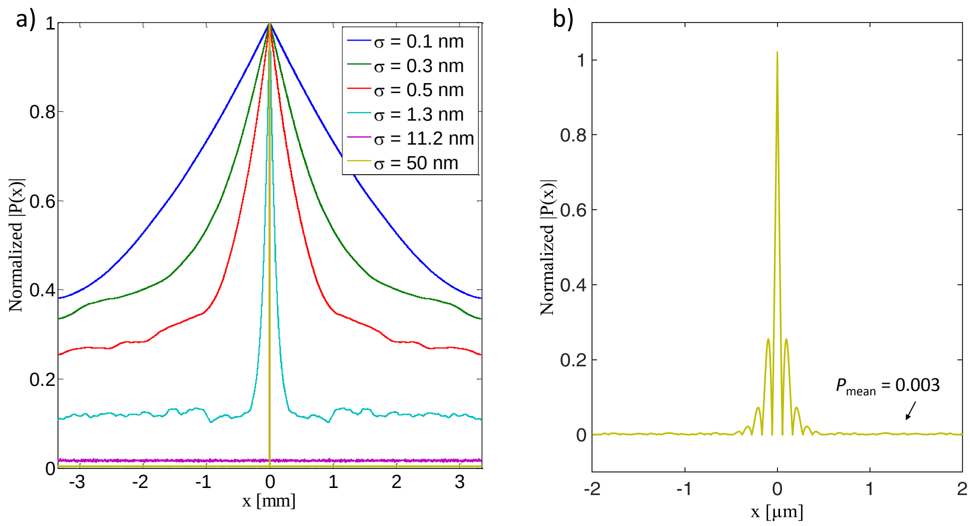

Figure 4.2: a) Normalized one-dimensional Patterson function of a synthetic one-dimensional magnetic domain pattern with gamma-distributed domain sizes for different values of the standard deviation σ of the distribution function. The average domain size has been set to 100 nm. The graphs have been smoothed with a kernel of 3 μm to suppress the strong high-frequency oscillations. The side lobe intensity varies from 0.38 to 0.003. b) Central part of the normalized one-dimensional Patterson function using a standard deviation $\sigma = 50$ nm and an average domain size of 100 nm. It shows that the dominant central part has a width of around 1 μm. It should be noted that the graph has an averaged side lobe intensity of 0.003 and is therefore non-zero.

and $m_z = 1$ values, representing M_z/M_S, is modeled to represent magnetic domains with up- and down-magnetization (see Fig. 5.7). A distribution function for the domain sizes is implemented to incorporate different domain size variations within the domain pattern. It is found that a gamma distribution can be used to describe magnetic maze domain patterns with significant domain size variations. It can also account for highly-ordered stripe domain patterns with vanishing domain size variation. For a detailed description and analysis of the used gamma distribution for the domain sizes, it is referred to section 5.3.2. The Patterson function can be obtained from the modeled one-dimensional domain pattern by using Eq. 4.9. Fig. 4.2 (a) shows the modulus of the one-dimensional Patterson function for different standard deviations σ of the gamma distribution, i.e., for different values of domain size variation within the domain pattern, using an average domain size of $D = 100$ nm. The graphs have been smoothed with a kernel of 3 μm width to suppress the strong high-frequency oscillations. Due to that the graphs display the general shape and characteristics of the modulus of the Patterson function. It can be seen from Fig. 4.2 (a) that the Patterson function has a broad and triangular-shaped structure at $\sigma = 0.1$ nm, which corresponds to an almost periodic domain pattern with almost a single domain size. With increasing amount of domain size variation, the width of the central peak decreases until it can be described by a single narrow peak ($\sigma = 50$ nm). Moreover, with increasing σ, the side lobes develop into flat planes. Figure 4.2 (b) shows the modulus of the Patterson function obtained from a domain size distribution with $\sigma = 50$ nm and an average domain size of $D = 100$ nm without smoothing the graph. It shows that the peak structure at the center is restricted to a total range of 1 μm. The side lobes are flat and show only slight fluctuations with an average value of 0.003. Similar results have been found by Asakura et al. [149] describing the Patterson function of a diffuse plate as a function of mean-square phase variations, i.e., surface-height variations and by Nugent et al. [84], describing the Patterson function of an NRA aperture.

2D Patterson function

The analysis of the Patterson function of a magnetic domain pattern can also be performed in two dimensions. For this, an MFM image of a magnetic maze domain pattern of a Co/Pt multilayer film with an average domain size of around $D = 150$ nm is utilized (Fig. 4.3 (a)). The modulus square of the Fourier transformed MFM image results in a synthetic two-dimensional diffraction pattern (Fig. 4.3 (b)). A subsequent Fourier transform of the diffraction pattern yields the two-dimensional Patterson function of the maze domain pattern (Fig. 4.3 (c)). Fig. 4.3 (c) shows that the two-dimensional Patterson function consists of a high-intensity peak structure in the center and slight intensity fluctuations on a constant side lobe in the remaining regions. An averaged one-dimensional profile of the two-dimensional Patterson function can be obtained via azimuthal averaging around the center (Fig. 4.3 (d)). Figure 4.3 shows that the azimuthally averaged Patterson function has the same signature as in the one-dimensional case, when a large variation of domain sizes within the domain pattern (maze pattern) is present (see Fig. 4.2 (b)). The peak structure in the center is also restricted to a total range of 1 μm. Furthermore, the side lobe is flat and shows slight fluctuations with an average value of 0.08.

From the one- and two-dimensional analysis of the Patterson function from magnetic domain patterns, it follows that for a maze-like domain pattern with a large variation of domain sizes, the Patterson function can be decomposed into a distinct

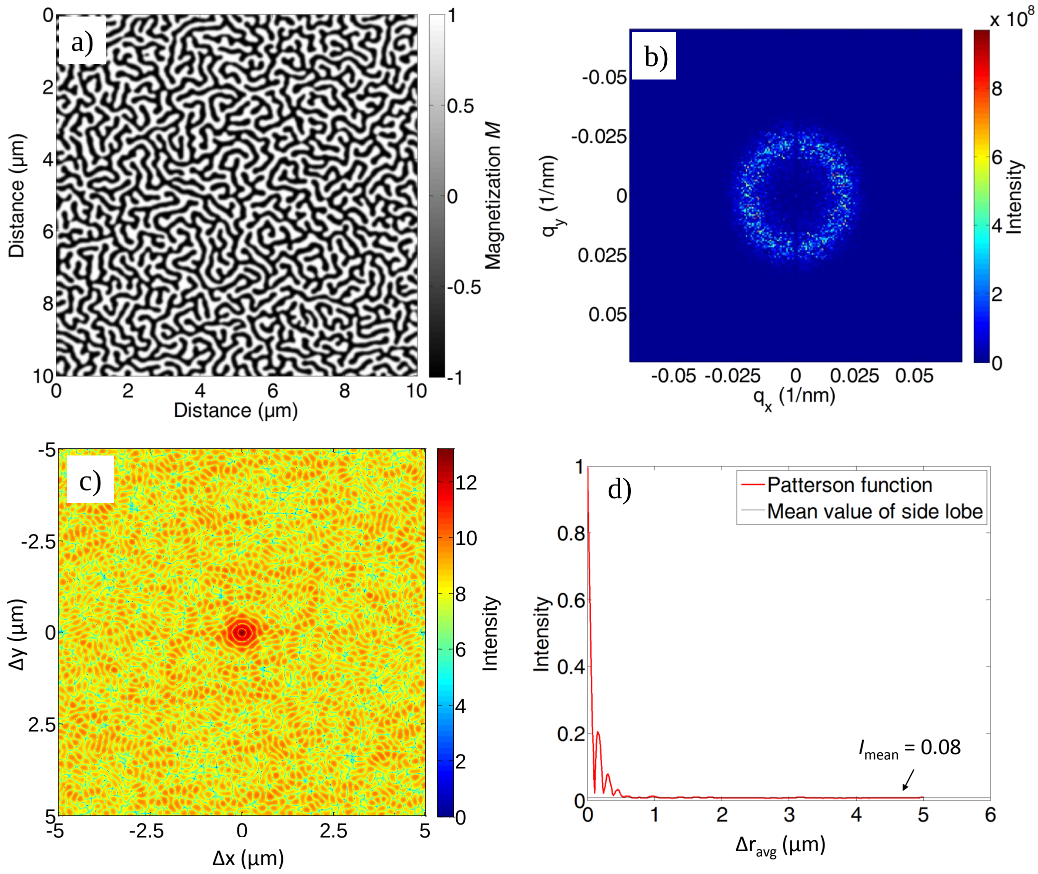

Figure 4.3: (a) Magnetic force microscope (MFM) image of a magnetic maze domain pattern with an average domain size of around 150 nm (courtesy of D. Stickler and J. Mohanty). (b) Central area of the modulus square of the Fourier transformed maze pattern showing a calculated donut-like diffraction pattern. (c) Modulus of the Fourier transformed diffraction pattern showing the Patterson map of the maze pattern (logarithmic scale). (d) Plot of the azimuthally averaged Patterson map (red solid line) yielding the high non-constant contribution of the Patterson function at the center position and a perfectly flat side lobe (black solid line).

narrow central peak ($\approx 1\ \mu$m width) and perfectly flat side lobes.

Is has been shown from the Fourier analysis method (section 4.1) that the Fourier transform of a magnetic speckle pattern can be expressed, within the Gaussian Schell-model, by the product of the modulus of the complex degree of coherence, the autocorrelation function of the beam intensity distribution and the Patterson function. In the context of the statistically stationary model, the latter is reduced to the product of the complex degree of coherence and the Patterson function. It has been shown that the Patterson function of a magnetic maze domain pattern with large variation of domain sizes is a constant, except in the vicinity of the central region. It follows, that the complex degree of coherence and hence the transverse coherence length (see section 2.1) can be extracted from the Fourier transformed magnetic speckle pattern without the knowledge of the exact shape of the Patterson function, as it is only a constant multiplicative factor in Eq. 4.3 and Eq. 4.4, except for the vicinity of the central region. Due to the fact that the high-intensity fringe-like structure in the central region only extends over a small distance it can be disregarded for the analysis.

In the following, the determination of the spatial coherence of X-ray radiation, i.e., the transverse coherence length, will be described in detail using the Fourier analysis method for two different XRMS experiments performed at the P04 beamline at PETRA III.

4.3 Determination of spatial coherence

Two XRMS experiments have been performed at the P04 beamline at PETRA III to determine the spatial coherence of X-ray radiation produced by the synchrotron radiation source. The first experiment has been carried out with the magnetic sample positioned out of the focus and the second experiment in the focus of the refocusing mirrors of P04. The experimental setup described in section 3.2 has been used for these experiments.

4.3.1 Experimental details

The first XRMS experiment (out-of-focus) has been carried out at a photon energy of 778 eV (Co L_3 absorption edge) using circularly polarized X-ray radiation and a $\mathrm{Co_{35}Pd_{65}}$ alloy sample (see section 3.3) as scattering medium. A monochromator exit slit of 200 μm has been used, resulting in a resolving power of $\lambda/\Delta\lambda \approx 3 \cdot 10^3$ at 778 eV and a longitudinal coherence length of $\xi_\mathrm{L} = 4.8$ μm (see section 3.1). The refocusing mirror unit set has been used to focus to the experimental platform in the vertical direction with a focal distance of 2.5 m and a focal size of 70 μm, which is related to the monochromator exit slit size. In the horizontal direction, the beam has been focused to a distance of about 15 m behind the setup with a focal distance of

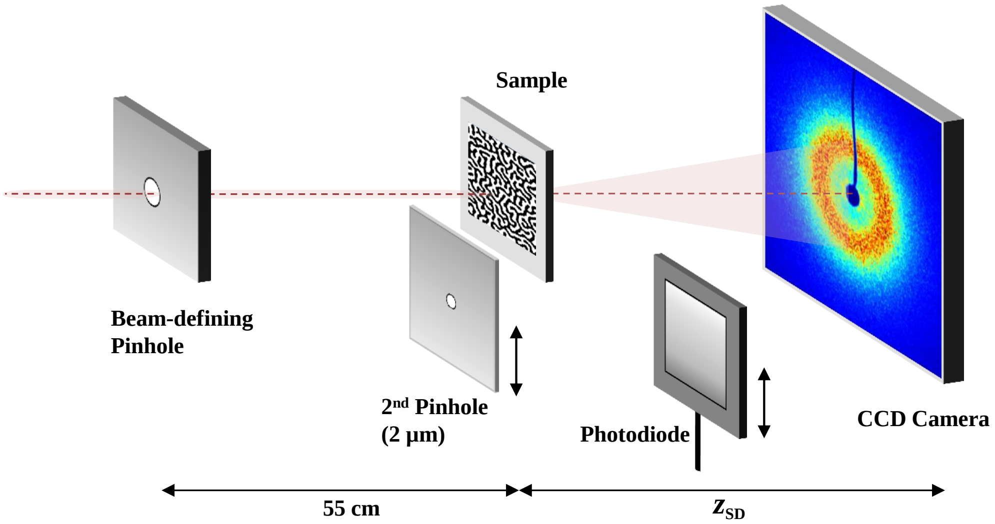

Figure 4.4: Sketch of the XRMS experiment. The beam coming from the left passes through the beam-defining pinhole, and is scattered at the sample. The scattering pattern is recorded by a CCD camera. The direct beam is blocked by a beam stop. Optionally, a second pinhole and a photodiode can be placed before and behind the sample to measure the beam size at the sample position.

16.9 m and a focal size of 100 μm[6]. The $Co_{35}Pd_{65}$ alloy sample has been placed 18 cm downstream of the vertical focus. A beam size of $\approx$ 25 μm x 49 μm FWHM (h x v) has been measured at the sample position by scanning the beam with a 2 μm pinhole mounted on the aperture mount (see Fig. 3.3 and 4.4). A sample-detector distance of $z_{\mathrm{SD}} = 1.06$ m has been used and a beam-defining 40 μm pinhole (first chamber, see Fig. 3.2). The largest path-length difference given by the dimension of the illuminated area and the maximum diffraction angle is $\Delta s = 0.7$ μm.

The second XRMS experiment (in-focus) has been performed at a photon energy of 778 eV using circularly polarized X-ray radiation and a $(Co_{0.8\mathrm{nm}}/Pt_{1.4\mathrm{nm}})_{32}$ multilayer film as scattering medium. A monochromator exit slit size of 50 μm has been used resulting in a resolving power of $\lambda/\Delta\lambda \approx 1 \cdot 10^4$ at 778 eV and a longitudinal coherence length of $\xi_{\mathrm{L}} = 15.9$ μm. The refocusing mirror unit set has been used to focus to the experimental platform in the vertical and horizontal direction with a focal distance of 2.5 m and a focal size of 17 μm and with a focal distance of 1.9 m and a focal size of 10 μm, respectively. The multilayer sample

[6] At the time of the experiment the horizontal RMU for the P04 platform was not yet installed. Instead the RMU of the PIPE platform has been used for the experiments.

has been placed in the focus. A sample-detector distance of $z_{\mathrm{SD}} = 32$ cm and a beam-defining 100 μm pinhole has been used. A beam size of ≈ 14 μm x 21 μm FWHM (h x v) has been measured at the sample position by scanning the beam with a 2 μm pinhole. The scattered X-rays are detected by a 4 Mpx CCD camera (PI-MTE 2048B) with a pixel size of 13.5 μm (Total chip size = 28 x 28 mm^2). The largest path-length difference is $\Delta s = 0.6$ μm.

The main differences of both experiments which are relevant for the coherence properties of the X-ray radiation are firstly that for the experiment (out-of-focus) the vertical component of the beam has been focused to the experimental platform of P04 and the horizontal component has been focused to the PIPE platform 16.9 m downstream of the experimental platform. Hence, the horizontal component can be considered as collimated. In the experiment (in-focus) the vertical and horizontal direction of the beam have been focused to the experimental platform of P04. Secondly, in the experiment (out-of-focus) the sample has been placed 18 cm downstream of the vertical focus, where in the experiment (in-focus) the sample has been placed in the focus. Thirdly, different exit-slit openings have been used for the experiments.

4.3.2 Determination of the transverse coherence length (out-of-focus)

In the following the determination of the transverse coherence length of the X-ray radiation used for the XRMS experiment (out-of-focus) under the above described experimental conditions is discussed. A series of magnetic diffraction patterns of the $Co_{35}Pd_{65}$ alloy sample has been recorded, each with an exposure time of 0.02 s. Each diffraction pattern has been dark-image corrected. Figure 4.5 (a) displays an averaged magnetic diffraction pattern of 50 successively recorded images. The ring structure indicates scattering from a magnetic maze domain pattern and the speckled structure within the annulus (Fig. 4.5 (a); inset) proves at least a partially coherent illumination of the magnetic sample (see Fig 2.8). The mean domain size calculated from the peak position of the radial scattering intensity profile obtained via azimuthal averaging around the center of the diffraction pattern is $D_{Q_{\max}} = \pi / Q_{\max} = 80$ nm.

Fig. 4.5 (b) shows the Fourier transform of the magnetic speckle pattern. As

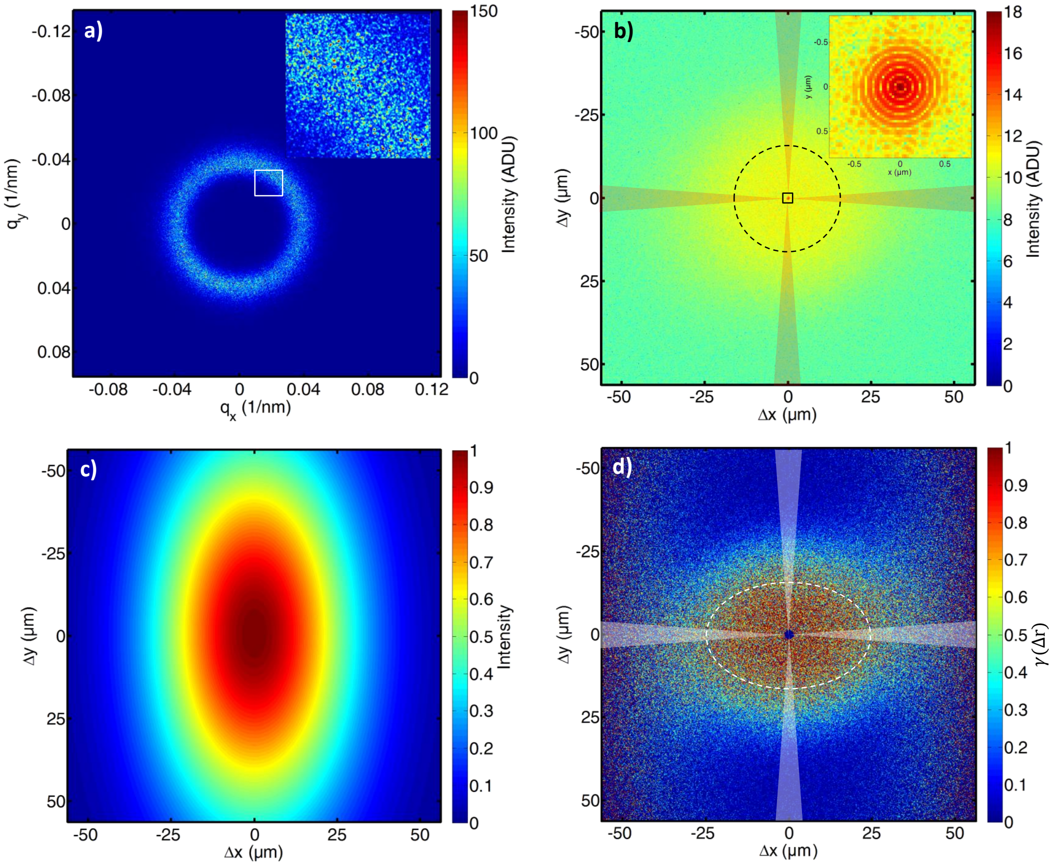

Figure 4.5: a) Magnetic diffraction pattern recorded at 778 eV photon energy from a $Co_{35}Pd_{65}$ alloy film. The inset shows a small section of the annulus revealing its speckled structure. b) FFT of the magnetic diffraction pattern (logarithmic scale). This is equivalent to the product of the modulus of $\gamma(\Delta\mathbf{r})$ with the modulus of the Patterson function $P_m(\Delta\mathbf{r})$ of the magnetic domain pattern and I_0 according to the statistically stationary model. The inset displays the center position of the image where the variation of the Patterson function is dominant. c) Autocorrelation function $K(\Delta\mathbf{r})$ of the Gaussian beam intensity distribution. $K(\Delta\mathbf{r})$ is a Gaussian profile with twice the beam width σ_B[7]. d) $\gamma(\Delta\mathbf{r})$ calculated within the Gaussian Schell-model (see text). The small red and white shaded areas in b) and d) represent the angular ranges used to determine the CDC and the transverse coherence length in the horizontal and vertical directions. The black dashed circle and white dashed ellipse in b) and d) indicate the determined transverse coherence lengths in all angular directions. In d) a mask with a diameter of 3 μm in the center has been used to mask out the high-intensity fringe pattern of the Patterson function at that position.

already discussed in section 4.1, the intensity distribution $I(\Delta\mathbf{r})$ of the Fourier-transformed speckle pattern is proportional to the modulus of the coherence function $\gamma(\Delta\mathbf{r})$. Hence, Fig. 4.5 (b) contains information about the two-dimensional spatial coherence properties and the intensity distribution of the incident X-ray beam. The high-intensity fringe-like structure in the center of the image illustrates the non-constant contribution of the Patterson function. It is only visible in the image center and has a total width of ≈ 1 μm resulting from the large variation of domain sizes. This observation is consistent with the findings presented in section 4.2.2. The Fourier-transformed speckle pattern can now be analyzed with respect to the Gaussian Schell-model (Eq. 4.3) and the statistically stationary model (Eq. 4.4).

In the framework of the statistically stationary model, Fig. 4.5 (b) equals $\gamma(\Delta\mathbf{r})$ except for a constant contribution of the Patterson function and I_0. No anisotropy of $I(\Delta\mathbf{r})$ is visible regarding its horizontal and vertical directions. Due to that, an average $\gamma(\Delta r_{\mathrm{avg}})$ can be extracted via azimuthal averaging around the center of $I(\Delta\mathbf{r})$ which thus represents the spatial coherence in all radial directions. Figure 4.6 (a) shows the extracted profile $I(\Delta r_{\mathrm{avg}})$. $\gamma(\Delta r_{\mathrm{avg}})$ is obtained from the profile by normalizing $I(\Delta r_{\mathrm{avg}})$ to its maximum value at zero separation ($\Delta r_{\mathrm{avg}} = 0$). Subsequently, the $\gamma(\Delta r_{\mathrm{avg}})$ profile is fitted with a Gaussian function $\exp\left(-\Delta r_{\mathrm{avg}}{}^2/2\xi_{\mathrm{T}}^2\right)$[8] (see Eq. 2.9) and an average transverse coherence length of $\xi_{\mathrm{T,avg}} = (15.6 \pm 0.5)$ μm is determined.

The small constant offset of $I(\Delta r_{\mathrm{avg}})$ cannot be explained by the theoretical description of the Fourier transform of the magnetic speckle pattern (see section 4.1 and Eq. 4.4), as $\gamma(\Delta r_{\mathrm{avg}})$ is, by its definition, converging to zero at large separation. It is found that the offset emerges from the readout noise of the CCD detector, which gives a constant background in the modulus of the Fourier transform even after appropriate dark image correction. The latter results in an additive contribution to the Fourier-transformed magnetic speckle pattern due to the linearity property of the Fourier transform. This issue is discussed and described in detail in section 4.4.

In order to extract $\gamma(\Delta\mathbf{r})$ along all angular directions of the two-dimensional plane, azimuthal averaging of small circle segments with an angular width of 10° has been carried out (red shaded area in Fig. 4.5 (b)). Simple line profiles show strong fluctuation due to the underlying Patterson function. The averaging has been done to improve the statistics. The results are plotted in Fig. 4.6 (b) revealing a constant transverse coherence length of $\xi_{\mathrm{T,avg}} = (15.6 \pm 0.5)$ μm in all angular directions, which is in-line with the former assumption of absent anisotropy in Fig. 4.5 (b).

[7] In the following, σ_{B} is the (rms) width of the X-ray beam at the sample position.

[8] In the following, ξ_{T} is the (rms) transverse coherence length of the X-ray beam at the sample position.

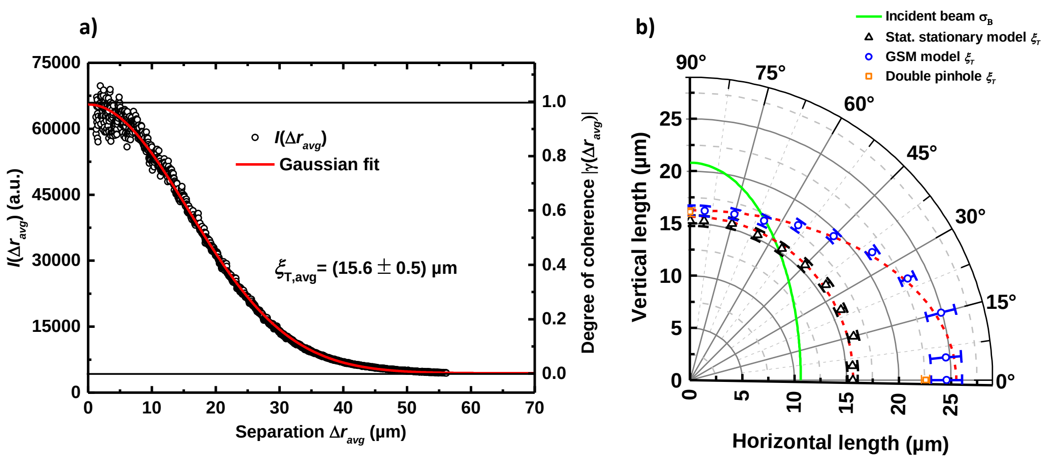

Figure 4.6: a) Averaged one-dimensional profile of $I(\Delta \mathbf{r})$ obtained via azimuthal averaging around the center of the Fourier-transformed magnetic diffraction pattern (black circles). $I(\Delta r_{\text{avg}})$ is normalized with its maximum value close to zero separation resulting in the modulus of $\gamma(\Delta r_{\text{avg}})$. Using a Gaussian fit (red line) a transverse coherence length of $\xi_{\text{T,avg}} = (15.6 \pm 0.5)$ μm is obtained. b) Polar diagram showing the transverse coherence length ξ_{T} in all axial directions determined in the frame of the statistically stationary model (black circles) and in the frame of the Gaussian Schell-model (blue circles). The red dashed lines denote the general shape along the axial directions and the green solid line represents the shape of the incident beam, characterized through its (rms) width σ_{B} in horizontal and vertical directions.

The global degree of coherence ζ (see Eq. 2.15) characterizes the transverse coherence properties of the incident X-ray beam by one number, which also accounts for the beam size. The global degree of coherence is $\zeta_{\text{v}} \approx 0.35$ in vertical and $\zeta_{\text{h}} \approx 0.59$ in horizontal direction which leads to a total degree of coherence of $\zeta = \zeta_{\text{v}}\zeta_{\text{h}} \approx 0.21$[9]. For the calculations, the transverse coherence length in vertical $\xi_{\text{T,v}} = (15.3 \pm 0.5)$ μm and horizontal direction $\xi_{\text{T,h}} = (15.6 \pm 0.5)$ μm, as well as the rms beam width in vertical $\sigma_{\text{B,v}} \approx 20.8$ μm and horizontal direction $\sigma_{\text{B,h}} \approx 10.6$ μm have been used. It will be shown in the following paragraph that this value is not exact, as the preconditions of the statistically stationary model is not fulfilled in the experiment ($\sigma_{\text{B,h}} > \xi_{\text{T,h}}$).

The data can be reanalyzed within the framework of the Gaussian Schell-model. Within the Gaussian Schell-model the beam intensity distribution of the incident X-ray beam is taken into account for the analysis. According to Eq. 4.3, the Fourier-transformed magnetic speckle pattern is normalized by $K(\Delta \mathbf{r})$, the autocorrelation

[9]Strictly speaking this is already violating the preconditions of the statistically stationary model, as a plane wave is not confined in space.

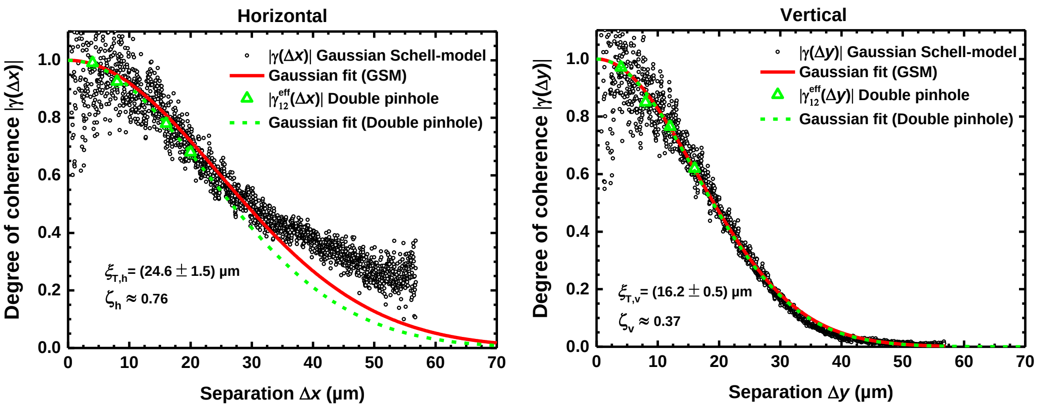

Figure 4.7: Modulus of the CDC in horizontal $\gamma(\Delta x)$ and vertical directions $\gamma(\Delta y)$ (black circles). The profiles are extracted from normalized Fourier-transformed speckle pattern (Fig. 4.5 (d)) using azimuthal averaging of small circle segments with an angular width of 10°. Using Gaussian fits (red lines), transverse coherence lengths of $\xi_{\mathrm{T,h}} = (24.6 \pm 1.5)$ μm in horizontal and $\xi_{\mathrm{T,v}} = (16.2 \pm 0.5)$ μm in vertical direction are obtained. The green triangles represent the CDC values obtained from Young's double pinhole experiment from averaged line profiles at different pinhole separations Δx and Δy (see section 4.5). Using Gaussian fits (green dashed lines), a transverse coherence length of $\xi_{\mathrm{T,h}} = (22.6 \pm 0.3)$ μm and $\xi_{\mathrm{T,v}} = (16.1 \pm 0.4)$ μm in vertical and horizontal direction is determined, respectively.

function of the square root of the Gaussian beam intensity distribution (Fig. 4.5 (c)), to obtain $\gamma(\Delta\mathbf{r})$ (see Fig. 4.5 (d)). Prior to normalization the constant offset has been subtracted from $I(\Delta\mathbf{r})$. The autocorrelation function of the square root of a Gaussian function results in a Gaussian profile with twice the beam width. The latter displays an elliptical profile according to the experimentally determined values for the beam width in horizontal and vertical directions (Fig. 4.5 (c)). The shape of the beam profile is basically not restricted to the Gaussian type in the analysis, so that the autocorrelation of the square root of any experimentally obtained beam profile can be utilized, as long as it shows no variation on the length scale of the magnetic domain pattern. After normalization $\gamma(\Delta\mathbf{r})$ can be extracted from $I(\Delta\mathbf{r})$ in all angular directions with the same procedure described above for the statistically stationary model (see Fig. 4.6). In vertical direction a transverse coherence length of $\xi_{\mathrm{T,v}} = (16.2 \pm 0.5)$ μm and in horizontal direction of $\xi_{\mathrm{T,h}} = (24.6 \pm 1.5)$ μm are obtained (Fig. 4.7). The results show a distinct asymmetry with respect to the vertical and horizontal directions, as can be clearly seen in Fig. 4.5 (d). Furthermore, an additional feature arises from the normalization that is recognizable at large separation in the horizontal direction. The non-Gaussian shape above $\Delta x = 40$ μm emerges from the first order peak of the Airy pattern of the incident beam, which appears at a radius of around 45 μm. It appears in the range of investigation due to the narrow width of the illuminating beam in the horizontal direction. The latter findings further confirms the validity of the presented normalization, since we see a well understood deviation from the assumed Gaussian beam. Due to the fact that the deviation has an impact on the complex degree of coherence in horizontal direction and hence on the transverse coherence length an increased error margin is assumed in that direction.

The global degree of coherence can be determined by means of the transverse coherence lengths in vertical and horizontal directions within the Gaussian Schell-model and yields $\zeta_{\mathrm{v}} \approx 0.36$ and $\zeta_{\mathrm{h}} \approx 0.76$. Thus, the total degree of coherence yields $\zeta = \zeta_{\mathrm{v}}\zeta_{\mathrm{h}} \approx 0.27$.

A Young's double pinhole experiment has been performed to corroborate the results from the Fourier analysis method and is described in detail in section 4.5. The results of the experiment are plotted in Fig. 4.7 and Fig. 4.6 (b), together with the results of the Fourier analysis method analyzed within the Gaussian-Schell model. From the double pinhole experiment a transverse coherence length of $\xi_{\mathrm{T,h}} = (22.6 \pm 0.3)$ μm in horizontal and $\xi_{\mathrm{T,v}} = (16.1 \pm 0.4)$ μm in vertical direction is obtained, respectively. It shows that there is really an asymmetry in the degree of coherence with respect to its horizontal and vertical axes, as it is also found from the Fourier analysis method analyzed within the Gaussian Schell-model. The results from both methods show a good agreement in horizontal as well as in vertical direction. In contrast, the analysis performed in the statistically stationary model shows only a good agreement with the results of the double pinhole experiment in the vertical direction and reveals a significant deviation in the horizontal direction. The prerequisites for applying the statistically stationary model in that direction are obviously not fulfilled. A normalization by means of the beam intensity distribution is indispensable to ensure reliable results in that direction.

The analysis of the data in the Gaussian Schell-model and statistically stationary model demonstrate that for the case that the X-ray beam size is much larger than the coherent fraction of the beam (vertical direction; see above) the coherence properties of the X-ray radiation can be well described by the statistically stationary model (see Fig. 4.6 (b)). In this case, the complex degree of coherence is the dominant contribution to the Fourier-transformed magnetic speckle pattern and consequently Eq. 4.3 and Eq. 4.4 give comparable results. However, if the beam size is small compared to the coherent fraction of the beam (horizontal direction; see above) the beam intensity distribution dominates and has to be considered in the analysis for a correct characterization of the coherence properties of the beam. In that case, the statistically stationary model underestimates the coherence properties of the X-ray beam.

Sampling considerations

The CCD detector consists of a finite number of pixels which sets restrictions to the field of view (FOV) and resolution. The detectable field of view $x_{\mathrm{FOV}} = \lambda z_{\mathrm{SD}}/s = 112\ \mu\mathrm{m}$ (see Fig 4.5 b)) is determined by the wavelength λ (1.59 nm for 778 eV), the sample-detector distance z_{SD} (1.06 m) and the pixel size of the CCD detector s (15 μm). The number of pixels $N = 4096$ defines the resolution in the space domain $x_{\mathrm{res}} = \lambda z_{\mathrm{SD}}/Ns = 27.4$ nm. The CDC can be mapped out up to a separation of $x = 112\mu\mathrm{m}/2 = 56\ \mu\mathrm{m}$ due to its centro-symmetry. Hence, it can be seen that a sufficiently large sample-detector distance and a small pixel size are prerequisites for the detection of the full two-dimensional coherence function.

4.3.3 Determination of the transverse coherence length (in-focus)

In the following the determination of the transverse coherence length of the X-ray radiation used for the XRMS experiment (In-focus) under the above-described experimental conditions is discussed. A series of magnetic diffraction patterns of the $(\mathrm{Co}_{0.8\mathrm{nm}}/\mathrm{Pt}_{1.4\mathrm{nm}})_{32}$ multilayer film has been recorded, each with an exposure time of 0.15 s. Each diffraction pattern has been dark image corrected. Fig. 4.8 (a) displays an averaged magnetic diffraction pattern of 21 successively recorded images. The ring structure indicates scattering from a magnetic maze domain pattern and the speckle structure reveals at least partially coherent illumination (Fig 4.8 (a), inset). The mean domain size calculated from the peak position of the radial scattering intensity profile obtained via azimuthal averaging around the center of the diffraction pattern is $D_{Q\mathrm{max}} = \pi/Q_{\mathrm{max}} = 96$ nm.

Figure 4.8 (b) displays the Fourier-transformed magnetic speckle pattern $I\left(\Delta\mathbf{r}\right)$. The high-intensity peak structure in the center is, as it has been shown in section 4.3.2, limited to a total width of $\approx 1\ \mu$m (Fig. 4.8 (b), inset) and illustrates the non-constant contribution of the Patterson function. The horizontal stripe structure

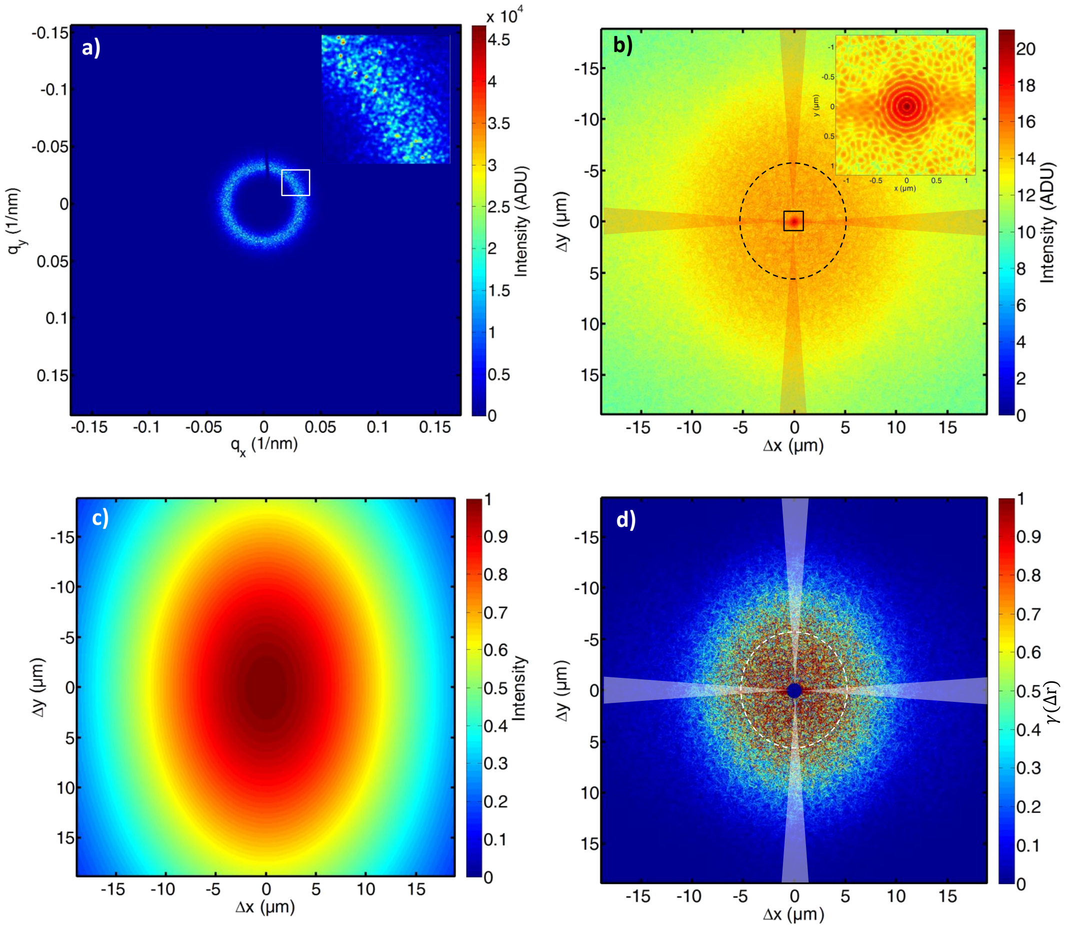

Figure 4.8: a) Magnetic diffraction pattern recorded at 778 eV photon energy from a $(Co_{0.8nm}/Pt_{1.4nm})_{32}$ multilayer film. The inset shows a small section of the annulus revealing its speckled structure. b) FFT of the magnetic diffraction pattern (logarithmic scale). This is equivalent to the product of $\gamma(\mathbf{\Delta r})$ with the modulus of the Patterson function of the magnetic domain pattern $P_m(\mathbf{\Delta r})$ and I_0 according to the statistically stationary model. The inset displays the center position of the image where the variation of the Patterson function is dominant. The horizontal stripe structure in the center constitutes the beam stop wire traversing the annulus in vertical direction in a). c) Autocorrelation function $K(\mathbf{\Delta r})$ of the Gaussian beam intensity distribution. $K(\mathbf{\Delta r})$ is a Gaussian profile with twice the beam width σ_B. d) $\gamma(\mathbf{\Delta r})$ calculated within the Gaussian Schell-model (see text). The small red and white shaded areas in b) and d) represent the angular ranges used to determine the CDC and the transverse coherence length in the horizontal and vertical direction. The black and white dashed ellipses in b) and d) indicate the determined transverse coherence lengths in all angular directions. In d) a mask with a diameter of 1.5 μm in the center has been used to mask out the high-intensity fringe pattern of the Patterson function at that position.

in the center constitutes the contribution of the beam stop wire which traverses the annulus in vertical direction (see Fig. 4.8 (a)). From Fig. 4.8 (b), a slight anisotropy of $I(\Delta\mathbf{r})$ is observed with respect to its horizontal and vertical directions. This gives rise to an elliptical shape.

In the framework of the statistically stationary model, $\gamma(\Delta\mathbf{r})$ and hence the transverse coherence length ξ_{T} can be extracted directly from the Fourier-transformed speckle pattern in all axial directions using azimuthal averaging of circle segments. Small circle segments with an angular width of 10° has been used for the analysis. The results for the transverse coherence lengths in all axial directions are plotted in Fig. 4.9 (a) and reveal a slight asymmetry with respect to the horizontal and vertical direction, as described above. The transverse coherence length in horizontal direction is $\xi_{\mathrm{T,h}} = (5.26 \pm 0.2)$ μm and in vertical direction $\xi_{\mathrm{T,v}} = (6.25 \pm 0.2)$ μm which result in values for the global degree of coherence of $\zeta_{\mathrm{h}} \approx 0.41$ in horizontal and $\zeta_{\mathrm{v}} \approx 0.33$ in vertical direction. The total degree of coherence yields $\zeta = \zeta_{\mathrm{v}}\zeta_{\mathrm{h}} \approx 0.13$.

The same procedure can be carried out to determine the transverse coherence lengths within the Gaussian Schell-model. For this, the Fourier-transformed speckle pattern is normalized by the autocorrelation function of the square root of the beam intensity distribution $K(\Delta\mathbf{r})$ (see Fig. 4.8 (c)) to obtain $\gamma(\Delta\mathbf{r})$ (see Fig. 4.8 (d)). The determined values for the transverse coherence lengths are plotted in Fig. 4.9 (a)). The complex degree of coherence in horizontal $\gamma(\Delta x)$ and vertical $\gamma(\Delta y)$ directions are shown in Fig. 4.9 (b). By fitting the data with a Gaussian function a transverse coherence length in horizontal direction of $\xi_{\mathrm{T,h}} = (5.79 \pm 0.2)$ μm and in vertical direction of $\xi_{\mathrm{T,v}} = (6.53 \pm 0.2)$ μm is obtained. The global degree of coherence is $\zeta_{\mathrm{h}} \approx 0.44$ in horizontal and $\zeta_{\mathrm{v}} \approx 0.34$ in vertical direction, respectively. Thus, the total degree of coherence is $\zeta = \zeta_{\mathrm{v}}\zeta_{\mathrm{h}} \approx 0.15$.

The Fourier analysis of the magnetic speckle pattern obtained from the XRMS experiment (In-focus) reveals, in this case, that the spatial coherence properties of the X-ray beam can be well described within the statistically stationary model in both directions (horizontal and vertical). The analysis of the data in the context of the Gaussian Schell-model reveals only a slight deviation of the transverse coherence length in both directions compared to the statistically stationary model. This is due to the fact that the transverse coherence length is much smaller than the beam width in vertical and slightly smaller in horizontal direction. Thus, $\gamma(\Delta\mathbf{r})$ is the dominant contribution in the Fourier-transformed magnetic speckle pattern $I(\Delta\mathbf{r})$. The analysis in section 4.3.2 has shown that a correction of the data is only required if the transverse coherence length is significantly larger than the (rms) beam width σ_B.

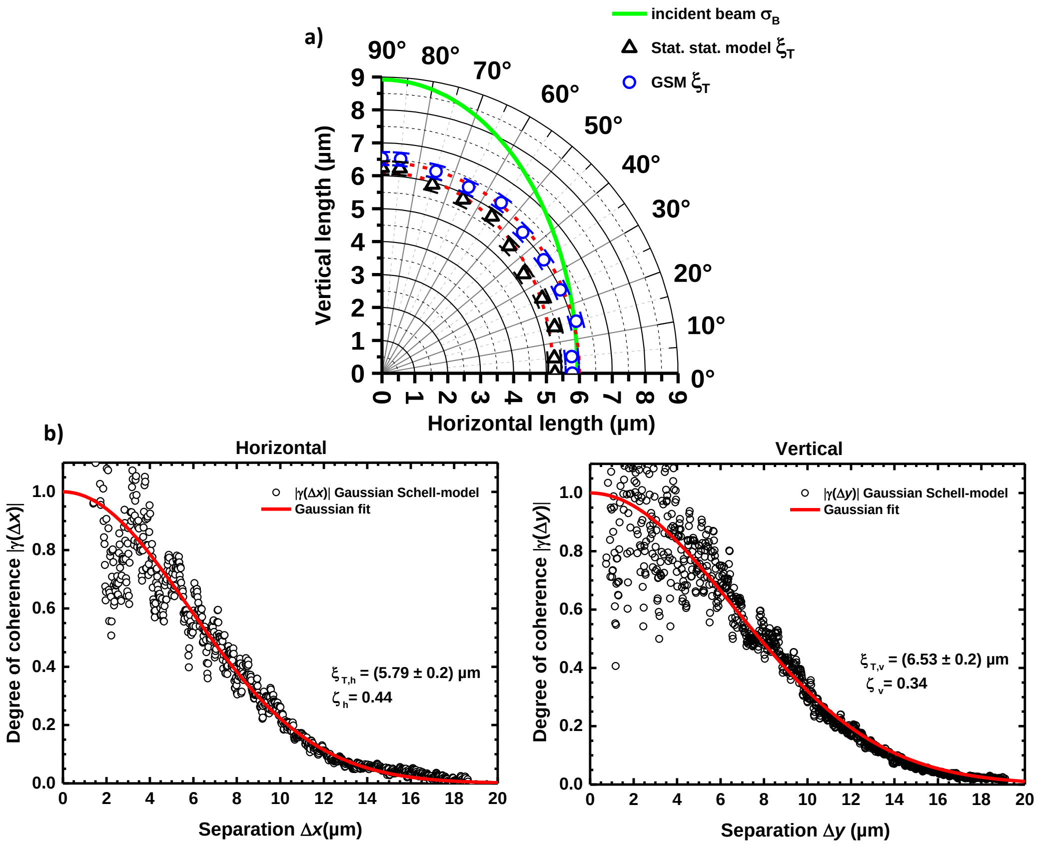

Figure 4.9: The determined transverse coherence lengths of the X-ray beam used for the XRMS experiment (in-focus). a) and b) show the polar diagram and the modulus of the CDC in horizontal $\gamma\,(\Delta x)$ and vertical $\gamma\,(\Delta y)$ directions, as it is shown for the XRMS experiment (out-of-focus) in Fig. 4.6 and Fig. 4.7 in section 4.3.2. From Gaussian fits to the CDC profiles, transverse coherence lengths of $\xi_{\mathrm{T,h}} = (5.79 \pm 0.2)$ μm in horizontal and $\xi_{\mathrm{T,v}} = (6.53 \pm 0.2)$ μm in vertical direction are obtained. In this case, as can be seen from the polar diagram, the Fourier analysis reveals only slight deviations of the transverse coherence lengths determined within the Gaussian Schell-model and the statistically stationary model. Furthermore, no deviations of the Gaussian shape of the CDC profiles, as it is found in the analysis in section 4.3.2, are apparent.

A quantitative understanding of the deviating results from the XRMS experiment (out-of-focus) and (in-focus) is not straight forward. This is due to the fact that different exit-slit openings (200 μm and 50 μm) have been used, the measurements have been performed at different positions along the beam propagation direction and in the out-of-focus experiment the X-ray beam in horizontal direction has not been focused to the experimental platform of P04. The exit-slit opening has a direct impact not only on the beam size (see section 3.1) but also on the transverse coherence length of the beam, as described in section 2.1.5. If the exit-slit openings of both experiments had the same size, the transverse coherence lengths in vertical direction could in principle be compared, as the relation between beam size and coherence length p (see section 2.1.3) or ζ (Eq. 2.15) remains unchanged along the propagation direction and with focusing (see section 2.1.5). Since the beam in horizontal direction is collimated in the out-of-focus case and focused in the in-focus, the transverse coherence lengths in that direction cannot be compared. However, both experiments can be qualitatively compared in the vertical direction. The experiments show that the transverse coherence length is significantly enhanced for measurements out of the focus, which is expected, as the transverse coherence length increases with increasing beam size. However, going out of focus involves a dramatic loss in photon flux [photons/s], which is a big disadvantage, since most experiments require a high photon flux. Therefore, most experiments are carried out in focus and hence it is important to know the coherence properties at that position, especially if high spatial coherence is required. The XRMS experiment (in-focus) shows a transverse coherence length of $\xi_{\mathrm{T,v}} = (6.53 \pm 0.2)$ μm. This coherence length is sufficient to perform CDI or XHM experiments, as the largest distances involved are typically 3-4 μm. At these separations the modulus of the CDC has values between $\gamma\,(\Delta y) = 0.87 - 0.78$. The results of the XRMS experiment (in-focus) can be compared with results from coherence measurements based on NRAs carried out at the beamline P04 [82]. The authors in [82] determined a transverse coherence length in vertical direction of $\xi_{\mathrm{T,v}} = (8.7 \pm 0.7)$ μm in the focus using an exit-slit opening of 50 μm. This value is larger than the one obtained in the experiment here. This is caused by the fact that the authors used a photon energy of 500 eV ($\lambda = 2.48$ nm) for their experiments in contrast to 778 eV ($\lambda = 1.59$ nm) for the Fourier analysis method and the transverse coherence length increases with increasing wavelength, as can be seen directly from Eq. 2.12.

4.4 Influence of speckle intensity and noise contributions on the Fourier analysis method

This section deals with the influence of speckle intensity and noise contributions on the performance of the Fourier analysis method. For this analysis, hundred single-exposure (0.02 s) magnetic speckle patterns obtained from the XRMS experiment (out-of-focus) are used. A series of averaged magnetic speckle patterns ranging from one to hundred averaged single patterns are calculated to study the effects of the detector noise and photon noise contributions. In a first step, it is convenient to calculate the speckle contrast C (see Eq. 2.45) as a function of the number of averaged speckle patterns, as it is directly related to the coherence properties of the beam (section 4.4.1). As a second step, the transverse coherence length and the constant offset (see Fig. 4.6 (b)) is determined for each averaged speckle pattern by means of the Fourier analysis method (section 4.4.2). The latter is performed within the statistically stationary model and only an average transverse coherence length $\xi_{\mathrm{T,avg}}$ is determined for the sake of simplicity.

4.4.1 Speckle contrast analysis

For the determination of the speckle contrast eight rectangular regions of interest (ROIs) of (100 x 100) pixels on the annulus of the magnetic speckle pattern have been selected (see Fig. 4.10 (b)). Each ROI exhibits a spatially uniform mean intensity of $\langle I \rangle = 34$ ADU. The speckle contrast is calculated using Eq. 2.45. Figure 4.10 (a) shows the average speckle contrast obtained from eight (100 x 100) pixel ROIs as a function of number of averaged speckle patterns N. It is found that the average speckle contrast converges from a high value of $C = 0.85$ for a single exposure speckle pattern to a constant value of $C = 0.53$ with increasing N. Figure 4.10 (c) illustrates the evolution of the speckle structure within a single ROI with increasing number of averaged speckle patterns N. The single image exhibits a grainy random-like structure with isolated high intensities in single pixels and differs significantly from the averaged speckle patterns above $N = 30$. Above $N = 30$, a concise smooth speckle structure emerges and remains unchanged with further averaging. The constant speckle contrast shown in Fig. 4.10 (a) and the unchanged speckle structure within the averaged ROIs shown in Fig. 4.10 (c) point out the temporal stability of the X-ray beam and the experimental setup during the experiment over the time span of 6.7 min (100 x (0.02 s exposure + 4 s readout time)). The single image ($N = 1$) is obviously dominated by either noise contributions of the CCD detector or photon noise.

After dark image correction, the main noise sources are Poisson noise (shot noise), readout noise and the noise associated with the dark current. The Poisson noise originates from the discrete nature of light. The readout noise is the noise of the on-chip amplifier which converts the electronic charge into an analogue voltage. The dark-current related noise is also known as thermal noise and arises due to thermal

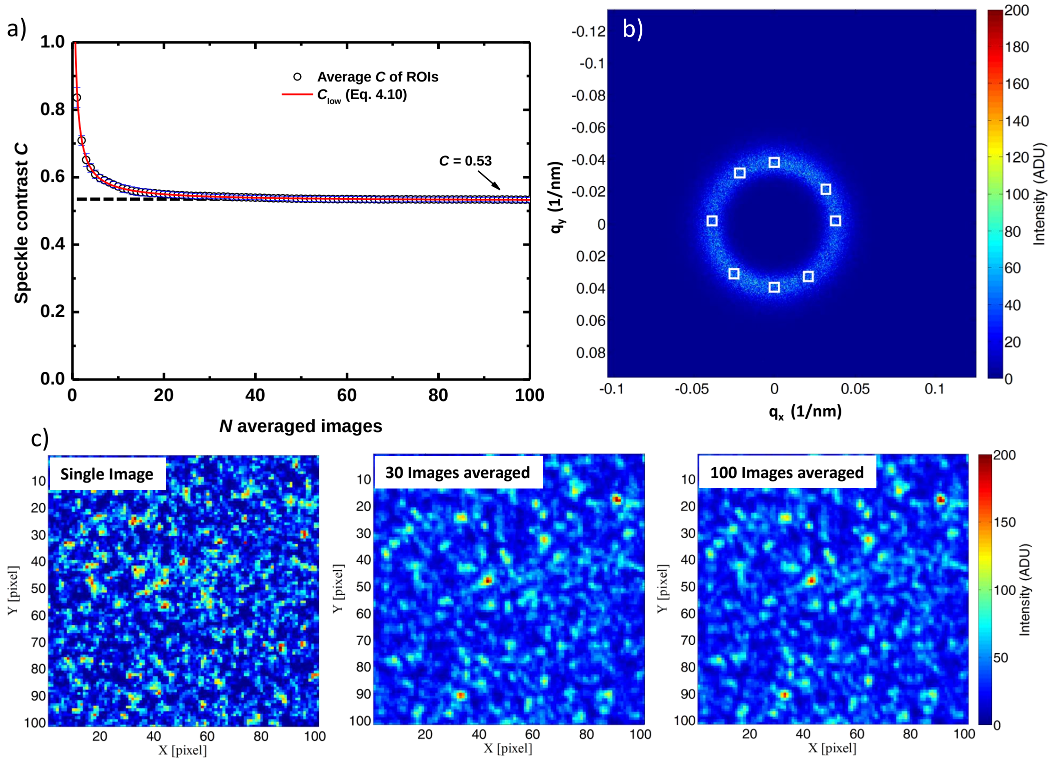

Figure 4.10: a) Averaged speckle contrast as a function of varying number of averaged magnetic speckle pattern. The speckle contrast converges to C = 0.53 for increasing number of averaged pattern. b) Magnetic speckle pattern obtained from the averaging of 50 single speckle pattern. White rectangles around the annulus denote the eight 100 x 100 pixel ROIs used for the determination of the average speckle contrast. c) ROIs of 100 x 100 pixels with varying number of averaged magnetic speckle pattern. It shows how the speckle structure develops upon averaging.

fluctuations generating electrons within the silicon chip. The readout noise present in a single image can be determined by calculating the standard deviation σ_{diff} of the intensity distribution of a difference image from two different dark images with short exposure $\sigma_{\text{single}} = \sigma_{\text{diff}}/\sqrt{2}$. With the latter procedure, a readout noise of $\sigma_{\text{single}} =$ 8.5 ADU is determined, which is consistent with the CCD camera specifications. Hence, the readout noise is only a minor noise contribution in the single image. The CCD camera was cooled down to $T = -50°C$ during the experiments, which results in thermal noise of 0.23 ADU/pixel/min and can thus be neglected.

The dominant noise contribution is the Poisson noise. Poisson noise is in contrast to readout and thermal noise not an additive contribution to the speckle pattern, but depends on the signal itself. In case of low-photon-number speckle patterns, the distribution for the number of photons per pixel k_p is given by the negative binomial distribution, that is a convolution of the Gamma and the Poisson distributions. The speckle contrast, in this case, can be described by [91, 156]

$$C_\mathrm{low} = \sqrt{C^2 + 1/(\bar{k}_\mathrm{p} N)}, \tag{4.10}$$

where $\bar{k}_\mathrm{p}$ is the mean number of photons per pixel. Equation 4.10 shows that the apparent speckle contrast is significantly enhanced for small $\bar{k}_\mathrm{p}$ due to fluctuations caused by photon counting statistics. With increasing amount of averaging the contribution vanishes and leads to the correct speckle contrast ($\approx N = 30$) and fully developed magnetic speckle patterns. From a fit of Eq. 4.10 to the data (see Fig. 4.10, red line), a mean number of photons per pixel and image $\bar{k}_\mathrm{p} = 2.19$ is obtained. The mean intensity $\langle I \rangle = 34$ ADU calculated for the ROIs[10] can be used together with the value $\bar{k}_\mathrm{p} = 2.19$ from the fit to calculate the number of ADUs per photon for the CCD camera setting, which amounts to $s = 16$ [ADU/photon]. This value seems to be quite small, so that a verification of this value via an independent procedure, e.g., using a droplet algorithm, should be carried out.

4.4.2 Influence of noise contributions on the Fourier analysis method

In this section the influence of the Poisson noise and readout noise on the parameters extracted from the Fourier analysis method, i.e., transverse coherence length $\xi_\mathrm{T,avg}$ and offset of $I(\Delta\mathbf{r})$ are discussed (see Fig. 4.6 (b)). For this, $\xi_\mathrm{T,avg}$ and the offset for a varying number of averaged magnetic speckle patterns are determined using the Fourier analysis method.

Figure 4.11 (a) shows the determined $\xi_\mathrm{T,avg}$ values as a function of averaged magnetic speckle patterns N. The shape of the curve for the average transverse coherence length behaves similarly to that of the speckle contrast (see Fig. 4.10 (a)). $\xi_\mathrm{T,avg}$ starts at a slightly increased value of $\xi_\mathrm{T,avg} = (17.2 \pm 0.5)$ μm and converges to a constant value of $\xi_\mathrm{T,avg} = (15.6 \pm 0.5)$ μm above $N \approx 10$. Thus, the transverse coherence length has a direct correlation to the speckle contrast and speckle structure, which is expected due to the fact that the information about the coherence properties is encoded in the intensity distribution, i.e., the speckle structure. The values at small N indicate an overestimation of $\xi_\mathrm{T,avg}$, which can be explained by a slight

[10]The mean intensity $\langle I \rangle$ remains unchanged with increasing number of averaged speckle patterns.

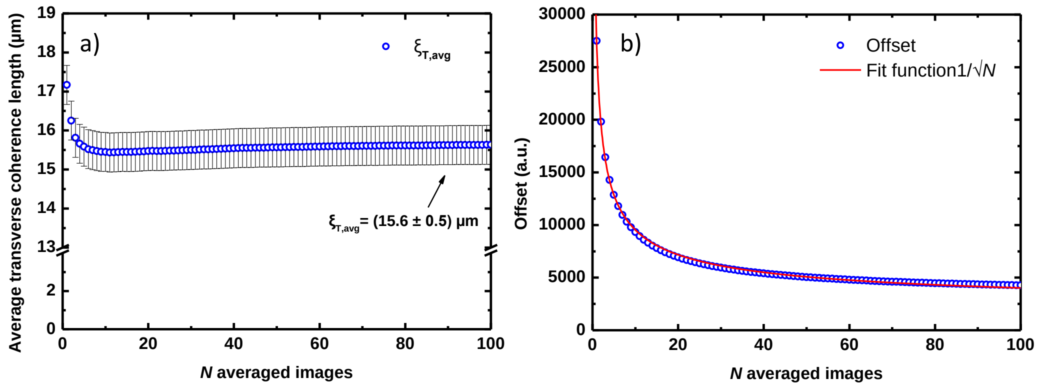

Figure 4.11: a) Transverse coherence length obtained from the Fourier analysis method from an increased number of averaged magnetic speckle pattern. b) Offset of $I\left(\Delta r_{\mathrm{avg}}\right)$ obtained from the Fourier analysis method with increased number of averaged magnetic speckle pattern.

smearing of the actual speckles due to the Poisson noise.

The offset of $I\left(\Delta r_{\mathrm{avg}}\right)$ as a function of averaged speckle pattern is shown in Fig. 4.11 (b) and a $1/\sqrt{N}$ behavior is found. The offset is expected to be independent on the speckle structure and only dependent on the underlying readout noise. The readout noise (σ) decreases due to averaging with $1/\sqrt{N}$, which is in good agreement with the behavior found for the offset of $I\left(\Delta r_{\mathrm{avg}}\right)$. Hence, the offset has a direct relation to the readout noise and can thus be reduced via averaging of many low-photon single speckle patterns or using longer exposure times for a single pattern.

The Fourier analysis method described in section 4.3.2 has been carried out using $N = 50$ averaged magnetic speckle patterns. The noise analysis in this section together with the speckle contrast analysis in the last section demonstrate that the Fourier analysis method has been conducted under stable conditions with respect to the noise contributions and speckle structure.

In summary, it can be said that deviations of the extracted parameters from the Fourier analysis method only occur for a very small signal-to-noise ratio (SNR) and can be avoided via averaging a large number of short exposure speckle patterns exhibiting small $\bar{k}_{\mathrm{p}}$ values or by choosing longer exposure times for a single speckle pattern.

4.5 Young's double pinhole experiment

In the following, a Young's double pinhole experiment is presented. The experiment has been performed to corroborate the results obtained from the Fourier analysis method demonstrated in section 4.3.2. For this, a set of double pinhole apertures has been manufactured and used to map out the complex coherence functions $\gamma(\Delta x)$ and $\gamma(\Delta y)$ in horizontal and vertical direction, respectively.

4.5.1 Fabrication of double pinhole apertures

For the fabrication of opaque optic masks with a double pinhole aperture, a $Au_{240nm}/(Pd_{120nm}/Au_{240nm})_4$ multilayer film has been sputtered onto a Si_3N_4 membrane of 500 x 500 μm^2 size and 100 nm thickness by means of a sputter-coater [69]. A focused ion beam (FIB) has been used to mill double pinholes with a diameter of 300 nm and varying pinhole separations into the multilayer [182] (see Fig. 4.12 (a)). The milling procedure has been carried out with a 20 pA Ga^+ ion beam at 30 keV using a 50 μm sized aperture.

4.5.2 Spatial coherence measurements

For the determination of the spatial coherence and to compare the results with the Fourier analysis method, the double pinhole apertures have been placed at the exact same position as the magnetic sample. In addition, a photon energy of 778 eV has been used for the experiment. Double pinhole fringe patterns with pinhole separations of $\Delta x = 4$ μm, 8 μm, 16 μm and 20 μm along the horizontal direction and $\Delta y = 4$ μm, 8 μm, 12 μm and 16 μm along the vertical direction have been recorded with the CCD. A number of 20 fringe patterns have been averaged for each separation with an exposure time of 25s per image. Figure 4.12 (b) shows the fringe pattern of a double pinhole aperture with $\Delta y = 4$ μm in vertical direction. The tilt of the pattern is caused by a tilted CCD chip with respect to the vertical axis[11]. The oval-shaped envelope of the double pinhole fringe pattern in Fig. 4.12 (b) results from an oval shape of all pinholes (see Fig. 4.12 (a)). It originates from ion beam astigmatism during fabrication and not from a different beam divergence in horizontal and vertical directions. The large sample-detector distance $z = 1.06$ m ensures a

[11] The tilt of the CCD has no influence on the performance of the Fourier analysis method as the direct FFT of the magnetic speckle pattern has revealed a symmetric $I(\Delta\mathbf{r})$ profile.

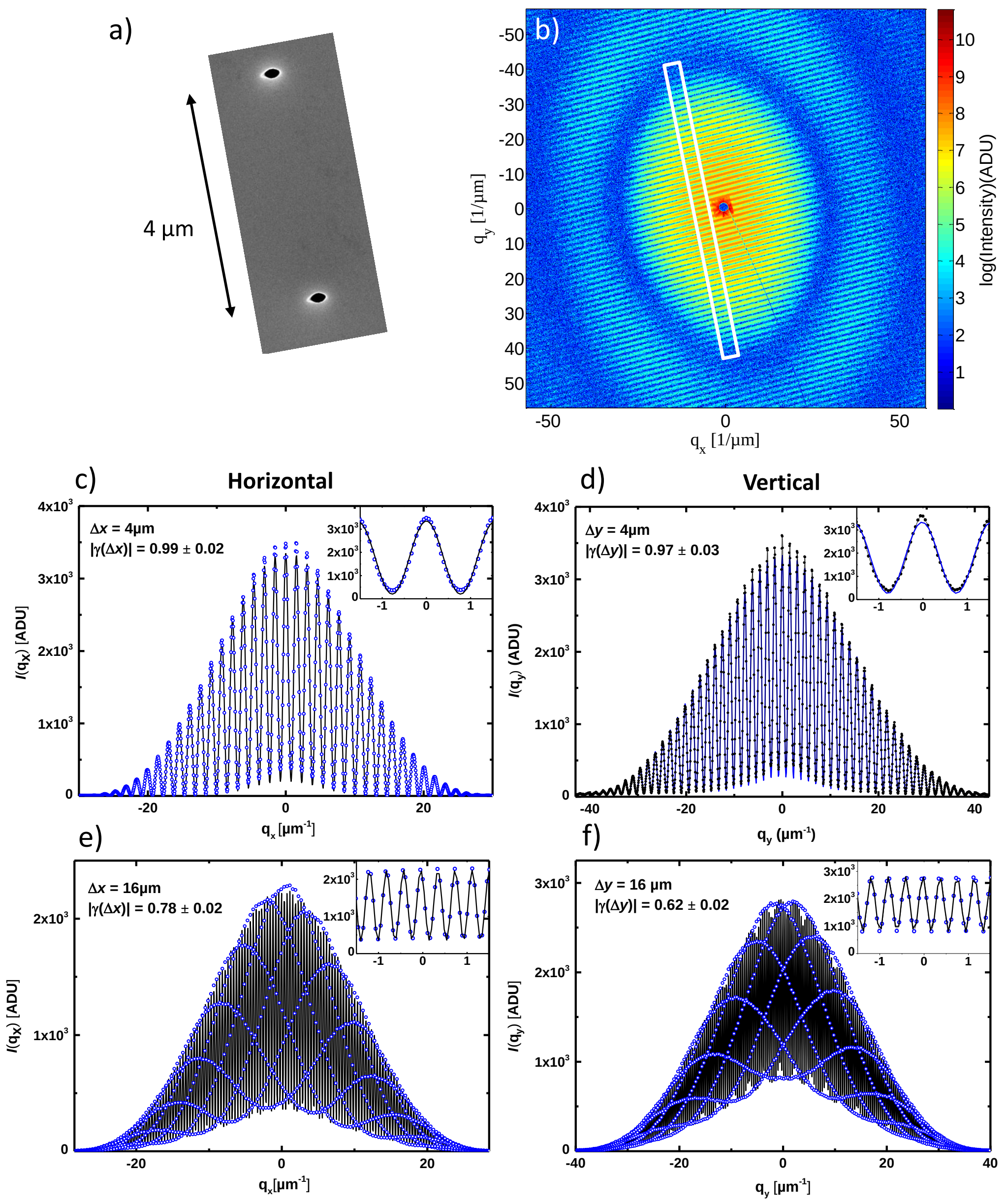

Figure 4.12: a) Scanning electron microscopy (SEM) image of a vertical double-pinhole arrangement with 4 μm pinhole separation milled into a Si_3N_4 membrane using focused ion beam (FIB). b) Fringe pattern of the double-pinhole arrangement shown in a) (logarithmic scale). The white rectangle marks the area used to extract averaged line profiles shown in c) - f). Averaged line profiles of the fringe pattern in horizontal c), e) and vertical direction d), f) for pinhole separations of Δx, $\Delta y = 4$ μm and Δx, $\Delta y = 16$ μm (blue dots) and the theoretical fit (see Eq. 4.11 (black line). The inset gives enlarged regions of the fringe pattern in the center.

sufficient sampling of the fringes (6 pixels per fringe at the largest separation $\Delta x = 20$ μm).

The intensity distribution of a double-pinhole fringe pattern can be expressed by [80, 81, 120]

$$I(q) = I_d \left[\frac{2J_1\left(a\sqrt{(q-q_{\text{off}})^2+u^2}\right)}{a\sqrt{(q-q_{\text{off}})^2+u^2}} \right]^2 \left\{1+\left|\gamma_d^{\text{eff}}\right|(\cos(dq+\alpha))\right\}, \tag{4.11}$$

where $I_d = I_1 + I_2$ is the total intensity of the individual intensities from each pinhole (I_1,I_2), J_1 is the Bessel function of first order, a is the diameter of each pinhole, q_{off} represents the q-shift of the envelope, u is the displacement of the extracted averaged profiles with respect to the center of the fringe pattern, $d = \Delta x, \Delta y$ is the pinhole separation, α describes the shift of the fringes with respect to the geometric center of the fringe pattern and γ_d^{eff} is the effective complex degree of coherence value for the separation d. The first term of Eq. 4.11 represents the Airy diffraction pattern from a single pinhole with diameter a. The second term describes the modulation of the fringe pattern, where its spatial extent is defined by the pinhole separation and its amplitude by the effective complex degree of coherence. The effective complex degree of coherence is defined by [80, 81, 120]

$$\gamma_d^{\text{eff}} = \frac{2\sqrt{I_1 I_2}}{I_1 + I_2}\gamma_d, \tag{4.12}$$

Equation 4.12 shows that if the two pinholes of the double-pinhole aperture are inhomogeneously illuminated ($I_1 \neq I_2$) the effective complex degree of coherence γ_d^{eff} extracted from the fringe pattern is reduced compared to the complex degree of coherence $\gamma_d = \gamma(\Delta x)$, $\gamma \Delta y)$. Inhomogeneous illumination can be caused by an inaccurate pinhole centering with respect to the X-ray beam or a non-uniform beam profile. It is assumed that the double pinholes are homogeneously illuminated in the experiment and thus $\gamma_d^{\text{eff}} = \gamma_d$. For this, each double pinhole aperture has been centered with respect to the beam. This has been done by taking line profiles in horizontal and vertical directions using the photodiode, obtained from scans of the apertures with respect to the beam.

For the determination of the complex degree of coherence values, averaged line profiles have been extracted from the averaged fringe patterns for each separation in the horizontal and vertical directions. Figure 4.12 c) - f) show the extracted averaged

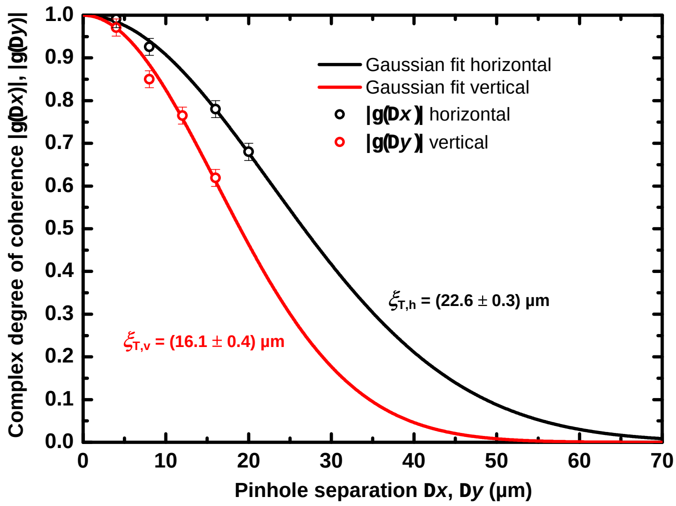

Figure 4.13: Modulus of the complex degree of coherence in horizontal $\gamma(\Delta x)$ and vertical $\gamma(\Delta y)$ direction extracted from averaged line profiles at different pinhole separations Δx, Δx. By using a Gaussian fit (red and black lines) the transverse coherence length in both directions can be calculated. A transverse coherence length of $\xi_{\mathrm{T,v}} = (16.1 \pm 0.4)$ μm and $\xi_{\mathrm{T,h}} = (22.6 \pm 0.3)$ μm in vertical and horizontal direction is determined, respectively.

line profiles in horizontal and vertical directions (blue dots) for a pinhole separation of $\Delta x, \Delta y = 4$ μm and $\Delta x, \Delta y = 20$ μm together with the theoretical fit (black lines) (see Eq. 4.11). The insets show an enlarged region of the curves in the center. A slight Gaussian-like background signal is found at the center of the fringe patterns and has been taken into account in the fit function through an additive Gaussian function. The background signal is caused by the fact that the beam-stop is slightly to small to block the whole direct beam, which is indicated by the rectangular structure in the center (projection of the membrane window).

The fringe patterns with Δx, $\Delta y = 4$ μm in horizontal and vertical direction illustrate a high visibility and thus a high complex degree of coherence. For larger separations Δx, $\Delta y = 16$ μm, the visibility decreases resulting in smaller values for the complex degree of coherence. It can be clearly seen that the visibility of the fringe pattern at $\Delta y = 16$ μm in vertical direction is slightly smaller than the one in horizontal direction, which gives rise to a smaller value of the complex degree of coherence in the vertical direction.

Figure 4.13 shows the values of the modulus of the complex degree of coherence extracted from the fringe patterns in horizontal and vertical directions as a function of separation $d = \Delta x$, Δy. The transverse coherence length for both directions is determined by using a Gaussian fit to the data [80, 81, 120]. A transverse coherence length of $\xi_{\mathrm{T,v}} = (16.1 \pm 0.4)$ μm in vertical direction and $\xi_{\mathrm{T,h}} = (22.6 \pm 0.3)$ μm in horizontal direction is obtained. The CDC profiles and determined transverse coherence lengths obtained from the double pinhole experiment have been compared with the ones obtained from the Fourier analysis method in section 4.3.2 and plotted in Fig. 4.6 and Fig. 4.7.

4.6 Conclusion and outlook

In this chapter a new method has been demonstrated to extract the two-dimensional representation of the complex coherence function and transverse coherence length from magnetic diffraction patterns. It has been found that ferromagnetic samples with magnetic maze domain patterns with large domain size variation are perfect candidates for this method, as their Patterson function is only given by an intense peak structure in the center (a few μm width) and perfectly flat side lobes. Thus, the Patterson function do not distort the complex coherence function and a determination of the transverse coherence length of the illuminated X-ray beam becomes feasible. Two experiments with different experimental geometries and beamline properties have been performed to determine the two-dimensional complex degree of coherence and transverse coherence lengths in all angular directions.

In the both experiments, the transverse coherence length has been extracted in all axial directions and analyzed within the framework of the Gaussian Schell-model and the statistically stationary model. To corroborate the results from the Fourier analysis method (out-of-focus) a Young's double pinhole experiment has been performed, using a double-pinhole arrangement in horizontal and vertical direction in the plane of the magnetic sample. It has been found from the Fourier analysis method in the framework of the statistically stationary model that the determined transverse coherence lengths show no asymmetry with respect to the horizontal $\xi_{\mathrm{T,h}} = (15.6 \pm 0.5)$ μm and vertical $\xi_{\mathrm{T,v}} = (15.3 \pm 0.5)$ μm directions. It appears that the transverse coherence length in the vertical direction is in a good agreement with the one obtained from Young´s double-pinhole direction $\xi_{\mathrm{T,v}} = (16.1 \pm 0.4)$ μm in the same direction. However, a significant deviation in the horizontal direction $\xi_{\mathrm{T,v}} = (22.6 \pm 0.3)$ μm is observed.

The data set has been reanalyzed in the frame of the Gaussian Schell model, where additionally the beam intensity distribution is taken into account for the analysis. Transverse coherence lengths in horizontal direction of $\xi_{\mathrm{T,h}} = (16.2 \pm 0.5)$ μm and in vertical direction of $\xi_{\mathrm{T,v}} = (24.6 \pm 1.5)$ μm are obtained. Both values show a perfect agreement with the findings of the Young´s double pinhole experiment. It has been found from the analysis that if the coherent fraction of the beam is small compared to the beam profiles, the statistically stationary model and the Gaussian Schell-model show almost equal results and a good agreement with the double pinhole experiment. On the contrary, if the coherent fraction of the beam is large compared to the beam size, the intensity distribution of the beam has a strong influence on the extraction of the complex degree of coherence and hence on the determination of the transverse coherence length. In the latter case, a normalization with the autocorrelation function of the beam intensity distribution is required for a correct interpretation of the coherence properties of the X-ray radiation.

In the second experiment the same analysis has been performed as described above. The main differences of both XRMS experiments are given by the fact that the second experiment has been performed in the focus of the beamline and both RMU sets have been used to focus the beam in horizontal and vertical directions, and the fact that two different exit-slit openings have been used. Within the statistically stationary model a transverse coherence length in horizontal direction of $\xi_{\mathrm{T,h}} = (5.62 \pm 0.2)$ μm and in vertical direction of $\xi_{\mathrm{T,v}} = (6.25 \pm 0.2)$ μm is obtained. Thus, a slight asymmetry exists with respect to the horizontal and vertical direction. The transverse coherence lengths in horizontal $\xi_{\mathrm{T,h}} = (5.79 \pm 0.2)$ μm and vertical direction $\xi_{\mathrm{T,v}} = (6.53 \pm 0.2)$ μm determined in the context of the Gaussian Schell-model show only a slight variation compared to the results obtained within the statistically stationary model. In this case, the transverse coherence length in vertical direction is much smaller and in horizontal direction slightly smaller than the beam size in the same directions. Thus, as described above, the beam intensity distribution has only a small impact on the extraction of the complex degree of coherence and the determination of the transverse coherence length.

It has been shown that the Fourier analysis method to extract the two-dimensional complex degree of coherence can be used to get an easy and fast access to the coherence properties of synchrotron radiation sources. It can be performed without any apertures such as double pinhole structures, non-redundant or uniformly redundant arrays of apertures. The method is in particular favorable for X-ray resonant magnetic scattering experiments, as any diffraction patterns measured in such experiments can be used directly to determine the spatial coherence of the illuminated X-ray beam. In addition, the method is applicable to various other sample systems with high degree of structural size variations along with an emerging speckle pattern.

In a future project the Fourier analysis method can be used for a full characterization of soft X-ray beamlines by changing exit-slit openings, beam-defining apertures and the wavelength. Due to the simple and fast analysis, the characterization can be carried out in a short time compared to coherence measurement using apertures. With this characterization an optimum beamline condition can be found for experiments which require highly coherent X-ray radiation.

Furthermore, the Fourier analysis method can be used to determine the spatial coherence of X-ray free-electron laser (FEL) light, especially in case of single-shot experiments.

5

X-RAY RESONANT MAGNETIC SCATTERING STUDY OF DOMAIN SIZES, DOMAIN PATTERN GEOMETRY AND ANISOTROPY IN Co/Pd MULTILAYERS

Co/Pd and Co/Pt multilayer films exhibit large perpendicular magnetic anisotropy (PMA) for Co layer thicknesses in the ultrathin regime, which is attributed to a strong surface and interface anisotropy in these systems [183–185]. These multilayers have attracted much attention especially due to their technological relevance in high areal density magnetic recording [24, 25] and are often used as model systems since they have been intensively studied in the last decades [145, 186, 187].

The formation of magnetic domains in ferromagnetic thin films with PMA is a consequence of the minimization of the total energy consisting of the magnetostatic self-energy and domain wall energy. The magnetostatic self-energy can be reduced through the creation of a series of oppositely magnetized domains separated by domain walls. The energy reduction and the associated decrease of domain size are accompanied by an increase of domain wall energy due to the growing number of domain walls [18]. The balance between both energy contributions determines the equilibrium domain size.

The magnetic domain structure can be arranged in diverse configurations such as stripe, maze or bubble domain patterns [18] and it has been found that the characteristic domain size depends strongly on domain morphology [188], film thickness [189–191] and field history [64, 192].

The magnetic microstructure links the physical properties and intrinsic energy contributions of the system with their macroscopic properties and can thus be seen as an ideal object for magnetic thin film studies. To be more precise, the investigation of the domain structure of thin ferromagnetic single- and multilayers with respect to characteristic domain sizes and pattern geometry gives access to, e.g., the magnetic anisotropy constants given the knowledge of exchange stiffness and saturation magnetization.

X-ray based techniques allow for studying magnetic domain structures by employing the circular dichroism at the absorption edges of selected magnetic elements as contrast mechanism. Real-space X-ray techniques are MTXM and STXM [49, 50, 55], while Fourier-space techniques are FTH [66–68], XHM [69, 171], X-ray ptychography [174, 193] and XRMS [62, 63, 137, 194–196]. XRMS does not provide a real-space image of the domain pattern, however, it is commonly used to obtain ensemble-averaged information from the multidomain state that naturally occurs in systems with out-of-plane easy axis of magnetization. Characteristic average properties, such as average domain size and lateral correlation length, can be extracted.
Ultrafast dynamic processes in magnetic materials are often studied utilizing XRMS in pump-probe experiments due to the high photon efficiency combined with the high photon flux available at free-electron laser sources allowing for single-shot measurements [11, 74].

The exact interpretation of the magnetic diffraction patterns and their correlation to the real-space domain structure is currently a matter of discussion and large relevance [73]. Magnetic models are required for the meaningful analysis of diffraction patterns from diverse domain structures. Models exist describing the diffraction pattern of well-aligned stripe domain patterns based on a one-dimensional periodic lattice [197]. Hellwig et al. [64] have presented an extended model to analyze scattering patterns of moderately disordered domain structures by implementing Gaussian fluctuations of the domain size. However, the interpretation of diffraction patterns from highly disordered two-dimensional maze domain patterns, where the domain walls are mostly curved and almost no straight sections occur, is still under debate. The scattering pattern of a two-dimensional domain structure obtained from micromagnetic simulation has been analyzed in [73], where a peak shift towards smaller momentum transfer Q has been found upon domain wall broadening.

In the following chapter, an XRMS experiment performed at the P04 beamline of the storage ring PETRA III is presented to investigate highly disordered magnetic maze patterns utilizing a wedge-shaped multilayer sample. As model system a wedge-grown Co/Pd multilayer film is used. The composition and fabrication procedure is presented in section 3.3.2. The Co/Pd multilayer wedge shows a thickness-driven spin-reorientation transition (SRT) from out-of-plane to in-plane orientation of magnetization that appears due to an occurring sign change of the effective first-order anisotropy constant with increasing cobalt film thickness. In the thickness range where the effective first order-anisotropy constant becomes small the domain size decreases upon thickness increase and the magnetization starts canting into the film plane. The SRT takes place via a state of canted magnetization due to a strong positive contribution of the second-order anisotropy constant, which suppresses the collapse of domain size during the SRT [198]. The investigation of the nanometer-sized domain structure of the Co/Pd multilayer film in the probed thickness range (see below) close to the spin-reorientation transition is a formidable task as the orientation of magnetization is highly susceptible to magnetic fields [199, 200]. Techniques that come along with local magnetic fields, like MFM, cannot be used to study the magnetic domain size in the range of zero crossing of the effective first-order anisotropy constant. For the investigation of the latter magnetic system all optical methods (XRMS, FTH, XHM) and electron-based techniques (SEMPA, X-PEEM, Lorentz microscopy) are most advantageous as magnetic fields are circumvented and a high spatial resolution is achieved.

The following chapter is structured as follows. First, the wedge-shaped Co/Pd multilayer sample is characterized and its thickness profile along the wedge is determined using X-ray absorption (XAS) profiles (section 5.1). Secondly, the XRMS experiment is presented, where radial scattering intensity profiles of the sample are extracted as a function of Co thickness (section 5.2). Thirdly, a model to describe highly-disordered maze domain patterns is presented that is used to interpret the evolution of the intensity profiles along the wedge (section 5.3). The model is based on random-generated synthetic one-dimensional domain patterns using gamma-distributed domain sizes to reproduce the significant domain size variations which occur in maze patterns. The modeled domain patterns are characterized by the mean domain size, the domain wall width, and the shape parameter of the distribution, which is shown to be characteristic for the domain pattern geometry. At last, a crosscheck is performed to test the model by means of an analysis of the magnetic properties of the wedge-shaped Co/Pd multilayer sample (section 5.4). Magnetic anisotropies at different Co thicknesses are determined using the mean domain sizes obtained from the model. Furthermore, the amplitudes of the intensity profiles in the Co thickness range where the magnetization canting sets in are utilized to determine the magnetic anisotropies in this regime. At the end, the results are concluded and possible further applications of the one-dimensional domain model are discussed (section 5.5).

For the experiments in the following chapter the experimental setup described in section 3.2 is used. The experiments have been performed under the same experimental conditions and geometry as described in section 4.3.1 (XRMS experiment (out-of-focus)). The only difference between the following experiment and the XRMS experiment (out-of-focus) is the sample-detector distance which has been set to $z_{\mathrm{SD}} = 19$ cm.

5.1 Sample characterization and thickness calibration using XAS and EDX

In the following the characterization of the wedge-shaped $(\mathrm{Co}_{\mathrm{t\AA}}/\mathrm{Pd}_{10\mathrm{\AA}})_8$ multilayer film is presented. The thickness of each cobalt single layer is varied from $\mathrm{t}_{\mathrm{Co,single}} = 0 - 10$ Å (see section 3.3).

The wedge sample has been demagnetized with a strong damped oscillating out-of-plane magnetic field (~ 1 Tesla) prior to the measurements. The latter procedure has been performed to transfer the magnetic domain pattern as close as possible to its magnetic ground state, as defects in the Co films can serve as pinning centers for domain walls. A proper demagnetization of the sample results in a maze-like magnetic domain pattern.

X-ray transmission profiles along the wedge have been taken with left $I_+(x)$ and right $I_-(x)$ circular polarization at a photon energy of 778 eV (Co L_3 edge). The profiles are recorded by scanning the $\mathrm{Si_3N_4}$ membrane window containing the sample with respect to the beam and measuring the transmitted intensity using a photodiode (≈ 3 cm behind the sample) (see. Fig. 5.1 (a)). An additional pinhole of 2 μm diameter directly in front of the Co/Pd sample has been used to define the spatial resolution for this measurement. The transmission profiles are displayed in Fig. 5.1 (a) (red and black lines). They show a stepwise change in intensity along the wedge between $x = 300$ μm and $x = 1000$ μm indicating the occurring circular dichroism due to changes of the local out-of-plane component of the magnetization M_{z} (magnetic domains). An additional decrease of intensity on top of the stepwise change results from the increasing total Co thickness along the wedge. An additional transmission profile $I_-(y)$ at 778 eV has been taken perpendicular to the wedge at $x = 300$ μm. It shows constant intensity (Fig. 5.1 (a); inset) and thus confirms a constant Co thickness in this direction.

The Co thickness profile $\mathrm{t}_{\mathrm{Co,total}}(x)$ along the wedge can be determined by using

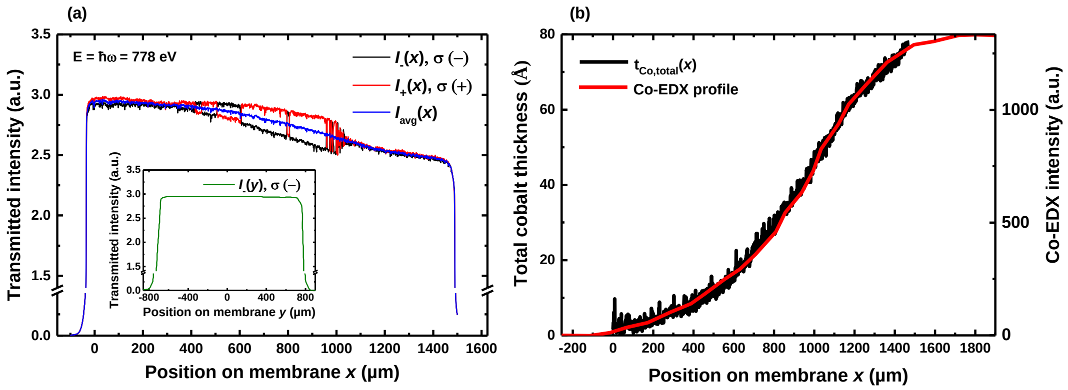

Figure 5.1: a) X-ray transmission profiles of the wedge-shape Co/Pd multilayer sample taken along the wedge at a photon energy of 778 eV with left $I_+(x)$ and right $I_-(x)$ circular polarization (red and black lines) and an averaged profile of both helicities $I_{\mathrm{avg}}(x)$ (blue line). The transmission profiles are taken by scanning the membrane window containing the sample with respect to the beam and measuring the transmitted intensity using the photodiode. The stepwise change of the profiles in intensity between $x = 300$ μm and $x = 1000$ μm indicate the occurring circular dichroism due to changes of the local out-of-plane component of the magnetization. The inset shows the transmission profile $I_-(y)$ taken perpendicular to the wedge at $x = 300$ μm (green line) which shows constant intensity and confirms a constant Co thickness in that direction. b) EDX profile (Co L_3 peak) along the wedge taken with a primary electron energy of 3 keV (red line) scaled with respect to the known thickness of 80 Å at the top of the Co/Pd wedge. Co thickness profile $\mathrm{t}_{\mathrm{Co,total}}(x)$ obtained from the average of the XAS profiles $\mu^{\pm}\mathrm{t}_{\mathrm{Co,total}}(x) = -\ln(I_{\pm}(x)/I_0)$ with opposite helicities and calibrated using the EDX profile (black line). From the calibration, a penetration length of $\lambda_{\mathrm{x}} = 1/\mu_0 = 41$ nm is obtained.

the X-ray transmission profiles ($I_{\pm}(x)$) and the Beer-lambert law under consideration of the XMCD effect

$$I_{\pm}(x) = I_0 e^{-\mu^{\pm}\mathrm{t}_{\mathrm{Co,total}}(x)} \tag{5.1}$$

with $\mu^{\pm} = \mu_0 \pm \Delta\mu$. Here, μ_0 covers the non-magnetic and $\Delta\mu$ the helicity dependent dichroic contributions. The transmission profiles are transformed into X-ray absorption (XAS) profiles via taking the logarithm $\mu^{\pm}\mathrm{t}_{\mathrm{Co,total}}(x) = -\ln(I_{\pm}(x)/I_0)$. The thickness of Pd, Pt and Si_3N_4 is constant within the film system. To eliminate the contributions from Pt, Pd, and Si_3N_4 the transmitted intensities $I_{\pm}$ are normalized with the intensity I_0 at $\mathrm{t}_{\mathrm{Co,total}}(x = 0) = 0$ Å where no Co is deposited (see Fig. 5.1). The Co thickness profile is obtained by taking the average of the XAS profiles $\mu_0\mathrm{t}_{\mathrm{Co,total}}(x) = (\mu^+\mathrm{t}_{\mathrm{Co,total}}(x) + \mu^-\mathrm{t}_{\mathrm{Co,total}}(x))/2$ (see Fig. 5.1 (b)). The averaging

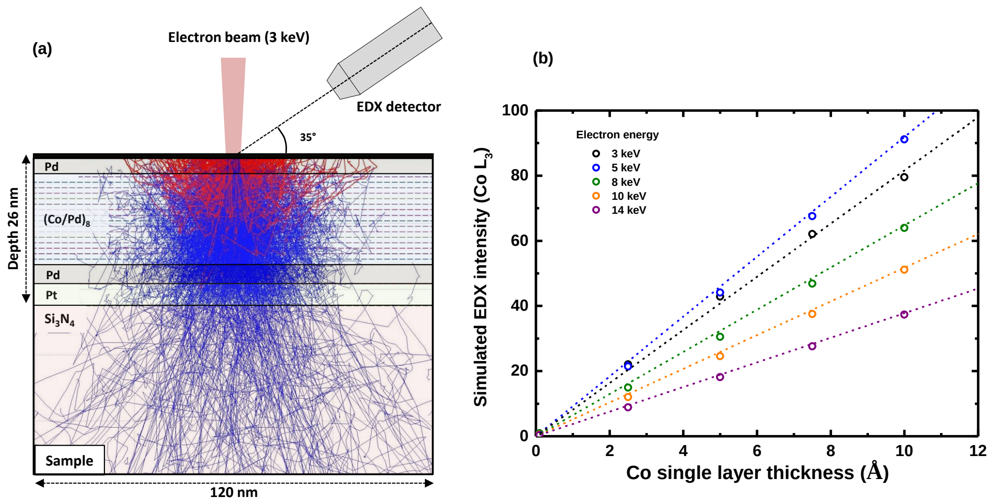

Figure 5.2: a) Layout of the EDX experiment in a SEM. Electron trajectories are simulated for the wedge-shaped $(Co_{t\text{Å}}/Pd_{1\text{Å}})_8$ multilayer with $t_{Co,single} = 10$ Å at an electron energy of 3 keV using Monte Carlo simulations [201, 202]. The interaction of the primary electrons with the sample (blue) indicate the interaction volume of the electrons. The back-scattered electrons are displayed in red. Characteristic X-rays are emitted from the whole interaction volume and detected by an EDX detector positioned at an angle of 35° with respect to the sample surface. b) Simulated EDX intensity of the Co L_3 peak as a function of the single layer Co thickness $t_{Co,single}$ of the $(Co_{t\text{Å}}/Pd_{1\text{Å}})_8$ multilayer obtained from Monte Carlo simulations. A linear behavior of the EDX intensity and Co single layer thickness for various electron energies is found.

procedure cancels out the dichroic contributions ($\Delta\mu$) so that only the resonant absorption of Co (μ_0) remains.

It can be seen from Fig. 5.1 that no plateau appears at the top of the thickness profile which is supposed to show a constant total Co thickness. Thus, the total wedge is not accessible in the X-ray investigation which is due to the limited size of the Si_3N_4 membrane window.

For comparison and calibration purposes, line profiles are taken along the wedge using energy-dispersive X-ray spectroscopy (EDX) in a scanning electron microscope (SEM) (Fig. 5.1 (b), red line). A layout of the EDX experiment is shown in (Fig. 5.2 (a)). The line profiles are taken at normal incidence with an electron energy of 3 keV at the Co L_3 peak and at an angle of 35° between sample surface and EDX detector. In Fig. 5.2 (a) a Monte Carlo simulation of the electron trajectories (blue) within the $(Co_{t\text{Å}}/Pd_{10\text{Å}})_8$ multilayer, which indicate the interaction volume, is presented for $t_{Co,single} = 10$ Å. The red trajectories represent the back-scattered electrons.

Characteristic X-rays are emitted from the whole interaction volume and detected by the EDX detector.

Monte Carlo simulations [201, 202] have been performed on the whole multilayer stack to check the linear dependency of the Co-EDX signal on Co thickness within the studied thickness range of the wedge-shaped Co/Pd multilayer film. EDX intensities of the Co L_3 peak of the EDX spectrum at various single-layer Co thicknesses (0.1 – 10 Å) and electron energies (3 - 14 keV) have been simulated (see. Fig. 5.2 (b)) using a number of $N_e = 2 \cdot 10^5$ electrons and an electron beam diameter of 5 nm. A linear dependency of the EDX intensity of the Co L_3-peak and the single layer Co thickness within the multilayer stack is found for all simulated electron energies. The overall decreasing EDX intensity with increasing electron energy originates from the fact that the region within the interaction volume, where the characteristic X-rays are emitted, is shifted to deeper regions of the film system and hence less X-rays are emitted from the Co layers.

Scaling the EDX profile with respect to the known thickness of 80 Å at the top of the wedge, the EDX profile can be utilized to calibrate the thickness profile (Fig. 5.1 (a); red line). It follows that a total Co thickness from $t_{\mathrm{Co,total}} = 1$ Å to 76 Å is accessible within the membrane window. The calibration procedure is necessary only in case of a non-existent plateau either at the onset or at the top of the wedge. From the calibration, a penetration length (see chapter 2.2.1) of $\lambda_{\mathrm{x}} = 1/\mu_0 = 41$ nm is obtained, describing the transmitted intensity via Beer-Lambert's law (Fig. 5.1 (b); black line). The penetration length is of around twice the size of the value measured in [124]. A possible explanation for the increased penetration length would be a large spectral bandwidth and hence low resolving power of the X-ray beam caused by the large exit-slit size of the monochromator (= 200 μm) used for the experiments (see chapter 4.3.1). The latter results in larger values for the penetration length. In addition, a minimal deviation (≈ 0.5 eV) of the ideal resonance (778 eV) can also cause highly increased penetration lengths. A later measurement and analysis of an equal sample system with a monochromator exit-slit size of 50 μm revealed $\lambda_{\mathrm{x}} = 1/\mu_0 = 23$ nm, which is close to the value measured in the literature [124]. This supports the above given explanation for the increased penetration length.

The magnetic XMCD asymmetry $M_{\mathrm{asym}} = (\mu_x^+ - \mu_x^-)/(\mu_x^+ + \mu_x^-)$ [130, 174, 203] of the Co/Pd multilayer film along the wedge is shown in Fig. 5.3. The magnetic asymmetry reveals changes of the magnetization profile along the wedge with a spatial resolution of 1 μm (The spatial resolution results from the convolution of the 2 μm circular aperture with a step function). The first dichroic signal appears at a Co thickness of $t_{\mathrm{Co,total}} = 8.5$ Å. Under the given experimental constraints, it can be as-

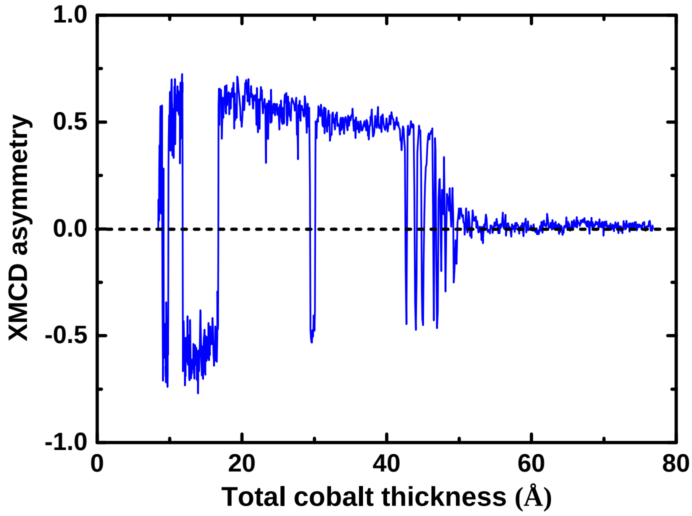

Figure 5.3: The XMCD asymmetry along the wedge at the Co L_3-edge (778 eV) calculated from the XAS profiles with left and right circular polarization (blue line).

sumed that at this Co thickness ferromagnetism occurs. The maximum of the asymmetry profile is $M_{\mathrm{asym}} \approx 0.6$ ($t_{\mathrm{Co,total}} = 11.4$ Å) and it decreases gradually towards $M_{\mathrm{asym}} \approx 0.5$ ($t_{\mathrm{Co,total}} = 43.8$ Å). The latter value for the XMCD asymmetry has also been measured by Saravanan et al. [204] for as-grown and annealed Pd(40Å)/Co(50Å)/Pd(40Å) trilayer films. Above a total Co thickness of $t_{\mathrm{Co,total}} = 46.6$ Å the dichroic contrast vanishes, which is caused by the fact that the magnetic domains become to small to be laterally resolved with the 2 μm pinhole. It is assumed that the observed change of the dichroic signal with decreasing $t_{\mathrm{Co,total}}$ is originating from an enhanced orbital angular momentum m_{orb}, which is proportional to the XMCD asymmetry [130, 205]. An enhanced orbital angular momentum has been observed in Co/Pd and Co/Pt multilayers [205–207]. Wu et al. [205] found an enhanced orbital momentum from $m_0 = 0.17\mu_B$ to $0.24\mu_B$ comparing a hcp Co thin-film sample of 25 nm thickness with a $(\mathrm{Co(4Å)/Pd(10Å)})_{11}$ multilayer. Nakajima et al. [206] report on an increasing orbital moment of Co/Pt multilayers below $t_{\mathrm{Co,single}} = 6$ Å with decreasing Co layer thickness. They assume that the Co layer is subjected to tensile stress from the Pt layer which increases for thinner Co layers. The latter gives rise to changes in the band structure. A systematic analysis of the change of orbital angular momentum with decreasing Co thickness in Co/Pt multilayers has been performed by Nakajima et al. [207]. The authors found a significant enhancement of the orbital moment from $m_0 = 0.13\mu_B$ to $0.17\mu_B$ by decreasing the Co layer thickness from $t_{\mathrm{Co,single}} = 20$ Å to 5 Å. They concluded that this effect originates from a strong Co 3d-Pt 5d interfacial hybridization which is together with the m_{orb} enhancement highly localized at the Co/Pt interfaces.

5.2 XRMS and imaging techniques to study domain sizes in Co/Pd multilayers

In the following, an X-ray resonant magnetic scattering and imaging experiment performed at a photon energy of 778 eV is presented using the wedge-shaped Co/Pd multilayer film to investigate the domain pattern evolution along the multilayer wedge. The experiment has been performed at the P04 beamline at PERTA III (DESY). The experimental conditions are described above and the experimental setup presented in section 3.2 has been used for the experiment.

5.2.1 Scanning transmission X-ray microscopy

To gain an overview of the magnetic domain pattern along the wedge, the sample is scanned in a two-dimensional plane perpendicular and parallel to the wedge using a fixed pinhole aperture with a diameter of 2 μm (see Fig. 5.4(b)). The scanning procedure is analogous to scanning transmission X-ray microscopy (STXM), however, as the scanning beam is not focused but cut with an aperture, the obtainable resolution at reasonable signal-to-noise ratio is much less. Figure 5.4(a) shows the obtained STXM image as a function of total Co thickness $t_{\mathrm{Co,total}}$. Magnetic domains are clearly visible in the range of $t_{\mathrm{Co,total}} = 40 - 50.3$ Å. It can be seen that the domain size decreases upon Co thickness increase, which is due to a decreasing effective first order anisotropy constant $K_{1,\mathrm{eff}}$, as it is described in section 5.4.1. The STXM image can be utilized to determine average domain sizes along the wedge. Average domain sizes from $D \approx 4$ μm down to 2.4 μm are found in a Co thickness range of $t_{\mathrm{Co,total}} = 46 - 49$ Å using stereologic methods [208, 209]. The latter method is based on the analysis of randomly oriented line profiles extracted from selected areas within the STXM image. Beyond a Co thickness of $t_{\mathrm{Co,total}} \approx 51$ Å the magnetic contrast vanishes, where the domains become too small to be resolved with the 2 μm pinhole (see Fig. 5.3). The spatial resolution is ≈ 1 μm, which results from the convolution of a 2 μm circular aperture with a step function.

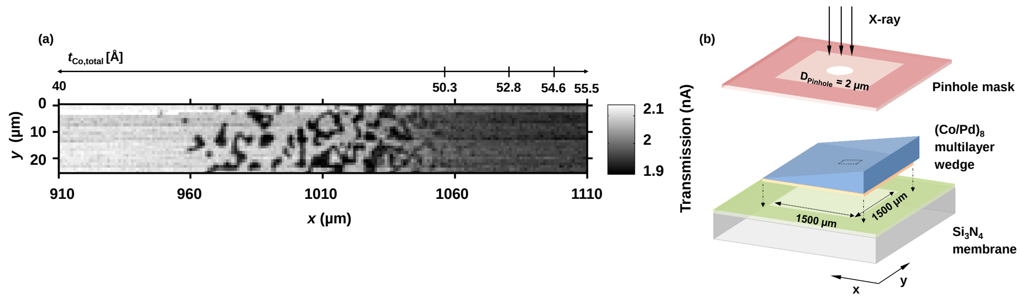

Figure 5.4: a) Scanning transmission X-ray microscopy (STXM) image taken at a photon energy of 778 eV with one helicity, which shows the domain size evolution with increasing Co thickness. b) Layout of the STXM and XRMS experiment. To obtain the two-dimensional (x-y-plane) STXM image the wedge sample is scanned along a fixed pinhole (Pinhole mask) with a pinhole diameter of 2 μm in x- and y-direction perpendicular to the beam. For the XRMS measurements the pinhole mask is detached and the wedge sample scanned with the total X-ray beam.

5.2.2 X-ray resonant magnetic scattering experiment

In order to study domain patterns with domain sizes in the nanometer range, an X-ray resonant magnetic scattering experiment at a photon energy of 778 eV has been performed. In XRMS experiments the spatial resolution is limited by the detectable momentum transfer Q and the wavelength $\lambda = 1.59$ nm. Additionally, signal-to-noise limitations are relevant due to the limited dynamic range of the CCD detector and the photon statistics, as the intensity drops strongly towards higher Q values ($I \sim 1/Q^{2..4}$; Small-angle regime [210]). The wedge-shaped Co/Pd multilayer film displays a magnetic maze domain pattern (see Fig. 5.4) to reduce dipolar energy. X-ray scattering on such patterns provides an isotropic donut-shaped magnetic diffraction pattern (see section 2.2.4). Due to the isotropy of the diffraction pattern a radial scattering intensity profile $I(Q)$ as a function of momentum transfer Q can be extracted using azimuthal averaging around the center of the diffraction pattern. The position $Q_{\max}$ of maximum intensity of the profiles $I(Q_{\max})$ in Fourier-space is roughly correlated to the ensemble-averaged domain size. Additionally, the width of $I(Q)$ corresponds to the transverse positional correlation of the magnetic domains, which is defined as the distance over which domains correlate with their neighboring domains. For a detailed description of the scattering intensity $I(Q)$ it is referred to section 2.2.4.

A series of magnetic diffraction patterns has been recorded at different Co thick-

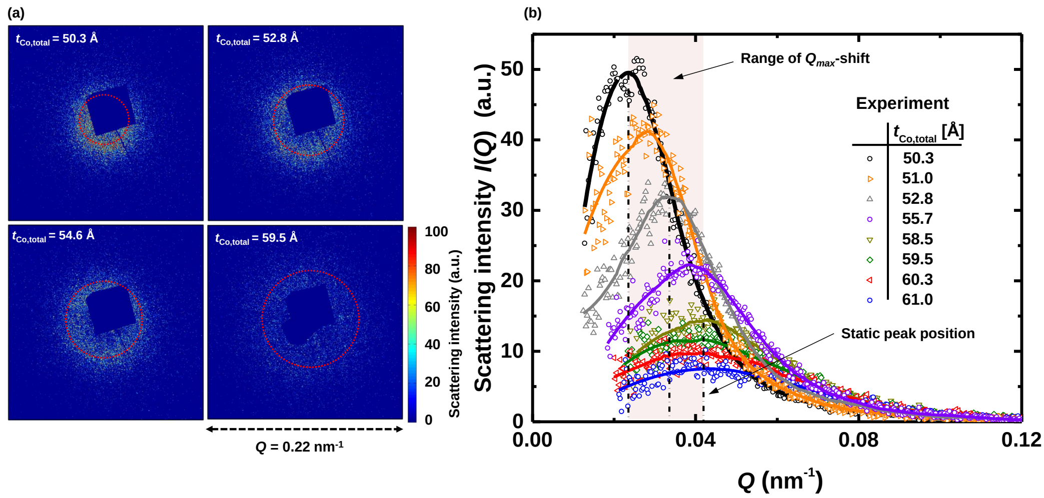

Figure 5.5: a) X-ray scattering patterns of magnetic maze domain structures. The rectangular structure in the center is used to mask out the superimposed projection image of the membrane window. Red dashed-line circles indicate the maximum of the radial scattering intensity profile for each Co thickness. b) Radial scattering intensity profiles extracted from the diffraction patterns via azimuthal averaging (colored symbols). A shift of the peak position Q_{max} (red shaded area), as well as a decrease of scattering intensity and increase of peak width are observed. Above a total Co thickness of $t_{\text{critical}} = 58.5$ Å the peak position is found to stay constant in Q while the intensity continues to drop. The solid colored lines show a smoothing of the data.

nesses using a step size of 10 μm (see Fig. 5.5). Each of the diffraction patterns is dark-image corrected and the superimposed charge scattering signal originating from the Si_3N_4 membrane window is masked out (rectangular structures in Fig. 5.5(a)). The diffraction patterns are used to extract radial scattering intensity profiles (see Fig. 5.5(b)). Fig. 5.5(b) illustrates the evolution of the profiles at different Co thicknesses along the wedge. It is found that for increasing Co thickness the peak positions Q_{max} of the profiles $I(Q)$ shift towards higher Q values within a total Co thickness range of $t_{\text{Co,total}} = 50.3 - 58.5$ Å. The peak position is commonly used to estimate the average domain size $D_{Q\text{max}} = \pi/Q_{\text{max}}$ resulting in $D_{Q\text{max}} \approx 131 - 70$ nm in the probed total Co thickness range. Additionally, a variation of the radial intensity profiles in width (FWHM) and amplitude towards larger Q values is observed. The width varies from $\Delta Q \approx 0.0246\text{nm}^{-1}$ to 0.0481 nm^{-1} corresponding to spatial in-plane correlation lengths of $2\pi/\Delta Q \approx 255$ nm to 130 nm. The latter implies that the probed maze pattern exhibits only short-range correlations. This is similar to the scattering from a static liquid, which is significantly different from the long-range correlations of stripe domains [64, 197]. Beyond $t_{\mathrm{Co,total}} = 58.5$ Å, which is named t_{critical} in the following, the peak position Q_{max} remains at the same Q, while the intensity continues to drop (see Fig. 5.5(b)).

In order to understand the evolution of the radial scattering intensity profiles on Co-thickness increase and their correlation to the real-space domain structure, a model is required that comprises the spatially disordered maze domain pattern. For slightly disordered stripe domain patterns a model has already been developed and published [64]. The model is based on a periodic lattice in which spatial disorder is included by implementing Gaussian fluctuations of the domain size to explain the finite peak width of the intensity profiles. Additionally, a linear domain wall profile is assumed. In [64] the model is used to fit the radial scattering intensity profile of a stripe domain pattern with an average domain size of $D_{Q\mathrm{max}} = 90$ nm and an in-plane correlation length of $2\pi/\Delta Q = 970$ nm. Thus, it is a long-range correlated system and differs significantly from the short-range correlated maze domain structure of the Co/Pd multilayer sample with large variation of domain sizes.

In the following, a model based on a one-dimensional domain pattern with gamma-distributed domain sizes is presented to describe strongly disordered maze domain patterns. The model is used to generate one-dimensional magnetic diffraction patterns, that have very similar intensity profiles to a disordered magnetic maze domain pattern. The former is utilized to fit the experimentally observed radial scattering intensity profiles.

5.3 Simulation of magnetic maze domain patterns

By means of micromagnetic simulations[1] in principle a model for the description of magnetic domains in maze patterns can be realized [73]. The simulation of a sufficiently large area is required to obtain reasonable statistics for the Fourier transformed domain pattern, i.e., for the magnetic diffraction pattern. However, the simulation of a large sample area in combination with high spatial resolution is often impractical due to limitations of computing time. Additionally, special procedures are needed for the extraction of the geometric parameters, e.g., average domain size and size distribution, from the simulated two-dimensional maze domain

[1] e.g., with the object oriented micromagnetic framework (OOMMF) [211] or MicroMagnum [212].

pattern. On account of the existence of an isotropic magnetic diffraction pattern (see Fig. 5.5(a)), the two-dimensional problem can be converted into a one-dimensional problem without causing a loss of information. The objective is to exploit the fact that the physical properties of the domain pattern, i.e., the domain sizes and their distribution function, are on average equal in all spatial directions. It follows, that this case allows for a one-dimensional description, as it keeps all information contained in the scattering profile. The latter issue can also be discussed in terms of a mathematical description. In this context, a two-dimensional maze domain pattern can be decomposed into a sum of stripe patterns with varying width and orientation, where each stripe pattern corresponds in Fourier space to a fixed spatial frequency and its complex conjugate partner. The azimuthal averaging procedure in Fourier space projects all orientations of the stripe patterns onto one direction leading to an averaged one-dimensional pattern. In case of an anisotropic diffraction pattern the domain size distribution is strongly dependent on the orientation and the average profile does not represent the two-dimensional pattern in all spatial directions. Hence, to good approximation a two-dimensional maze domain pattern can be described by a one-dimensional pattern if the maze structure reveals an isotropic magnetic diffraction pattern.

A further issue in relation to the simulation of maze patterns is to find a suitable domain size distribution. This issue is discussed in the following.

5.3.1 Analysis of the domain size distribution of magnetic maze domain patterns

In order to find a proper distribution function for the maze pattern, a published domain size distribution of a maze pattern [213] has been studied. Unfortunately, real-space images of the Co/Pd wedge sample in the range of investigation ($t_{\mathrm{Co,total}} = 50.3 - 61.0$ Å, see above) close to the spin-reorientation transition with high spatial resolution utilizing, e.g., MFM cannot be taken and used for the analysis. This is due to the fact that the domain structure is highly susceptible to magnetic fields. X-ray holographic microscopy (XHM) images of the domain structure could not be recorded. This is presumably caused by non-optimal optics masks at the time of the experiment. In addition, the limited size of the probed area ($\approx 1 - 3$ μm) is inappropriate to extract a representative size distribution for the domain pattern. A

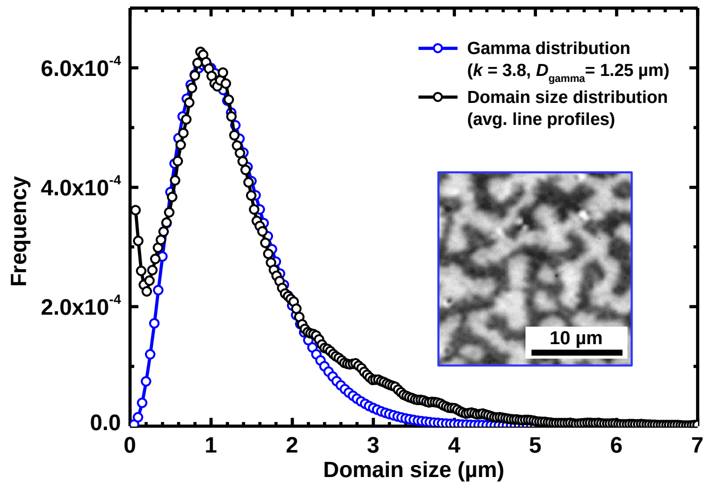

Figure 5.6: Comparison of the domain size distribution of a maze pattern from a Nd-Fe-B sample extracted from line profiles (black circles) with the probability density function of a gamma distribution (blue circles) fitted to the data. The inset shows a part of a Kerr image from this sample. The domain size distribution and the Kerr image have been taken from Fig. 2 in [213]). A good agreement of both curves is apparent. The increasing frequencies at very small domain sizes occur from wavy domain walls specific to the system (see [213]). Only in the range between 2 and 3 times the mean domain size deviations are present.

sufficiently large area is needed to obtain appropriate statistics for the domain size distribution. For the purpose of generality the domain size distribution of a maze pattern presented in [213] has been utilized for the analysis. Thielsch et al. [213] have investigated a Kerr microscopy image (100×100 μm^2) of a Nd-Fe-B sample using line profiles along different directions (Horizontal, vertical and diagonal lines) and measuring the distances between domain walls. The obtained histograms of the domain sizes reveal an equal shape of the distribution function in all measured directions, which indicates that the domain size distribution is spatially isotropic. The analysis (reproduced in Fig. 5.6 from Fig. 2(b) in [213]) yields a strongly asymmetric distribution of domain sizes which is at variance with a symmetric Gaussian peak shape. The distribution falls off faster towards small domain sizes and extends wider towards large domains. It is found that a gamma distribution can be used to describe this asymmetric distribution function properly. Comparing the extracted domain size distribution with the probability density function of the gamma distribution, a good agreement of both curves is obtained, when a mean domain size of 1.25 μm and a shape parameter of $k = 3.8$ are used. Two systematic deviations of the model can be

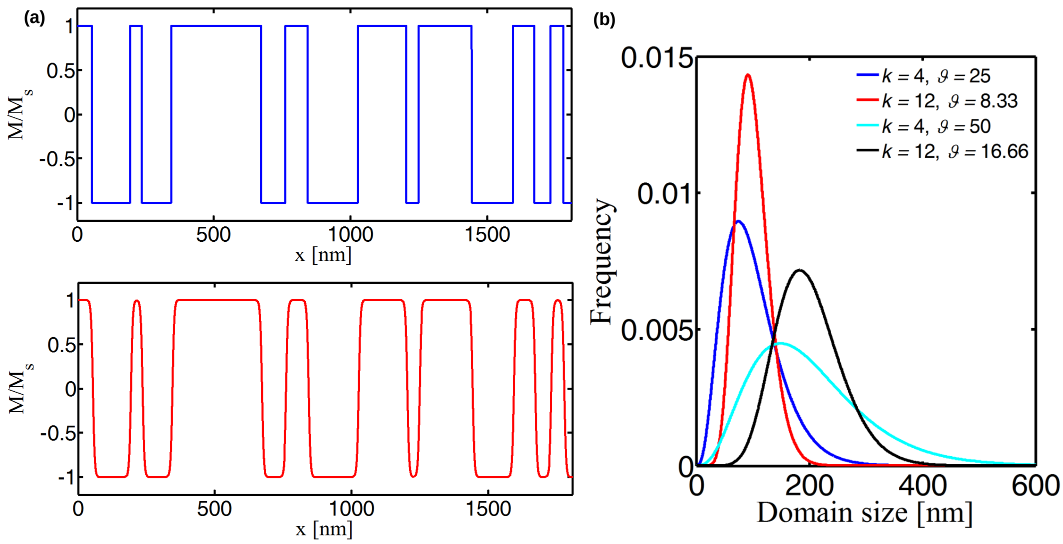

Figure 5.7: a) Section of a one-dimensional domain pattern with gamma-distributed domain sizes ($k = 4, \mu = 100$ nm) with infinitesimally sharp domain walls and b) with a hyperbolic-tangent domain wall profile with a width of 20 nm. c) Probability density function of the gamma distribution for different sets of shape parameter k and scale parameter ϑ. The probability density function develops into a Gaussian for larger values of k.

observed from the comparison. The first is a small underestimation of the frequency for domain sizes in the range of 2 to 3 times the mean value, where the total weight of this deviation is about 7%. The second is an increasing frequency at very small domain sizes. This is discussed in [213] as a consequence of wavy domain walls specific to this system. Such wavy domain walls are not observed in Co/Pd or similar Co/Pt films [49, 66, 198]. For this example it is clear that the domain size distribution of the two-dimensional maze pattern is fairly well described by a one-dimensional gamma distribution. A more complicated empirical distribution function might give a more exact agreement, but this requires an increased number of fit parameters and might thus be less meaningful. The number of parameters to describe the gamma distribution is two, just as for the case of a Gaussian description, so the complexity of the model is not increased. Hence, a gamma-distributed domain size appears to be reasonable for modeling a more realistic domain pattern in the range of the SRT.

5.3.2 Generation of a one-dimensional domain pattern with gamma-distributed domain sizes

In the following, a model to describe highly-disordered maze domain patterns is presented. It is based on random-generated one-dimensional domain patterns utilizing gamma-distributed domain sizes (see above) to reproduce the large domain size variations present in magnetic maze patterns.

The magnetic domain pattern is modeled as follows: First, the widths of all domains within the pattern are generated numerically by gamma-distributed random numbers. Subsequently, a one-dimensional array of discrete consecutive magnetic elements is generated with values of +1 or -1, indicating the local magnetization as up or down (see Fig. 5.7 (a)). The size of the individual magnetic elements is defined by the numerically generated domain widths. The total length of the array is set to several millimeters in order to increase the statistics in the model and to take into account the large number of magnetic domains within a two-dimensional maze pattern. The sampling of the array is set to 0.1 nm which defines the spatial resolution. The squared modulus of a subsequent fast Fourier transform (FFT) reveals a modeled scattering intensity profile $I(Q)$ as a function of momentum transfer Q for the generated magnetic domain pattern (see Fig. 5.8). The obtained $I(Q)$ is normalized by the length of the array, so that the intensity is independent on that length.

The probability density function (PDF) of the gamma distribution is parametrized with a scale parameter $\vartheta > 0$ and a shape parameter $k > 0$ (see Fig. 5.7 (b)) and is given by [214]

$$g\left(x\right) = \frac{x^{k-1}\exp(-x/\vartheta)}{\vartheta^{k}\Gamma(k)}, x > 0, \tag{5.2}$$

where $\Gamma(k) = \int_0^\infty t^{k-1}\exp(-k)dt$ is the gamma function. The parameter k influences the shape of the distribution function and thus affects its symmetry and width. For large shape parameter ($k \geq 12$) the PDF of the gamma distribution resembles a Gaussian with narrow peak width (see Fig. 5.7 (b)). With decreasing k, the peak shape gets increasingly asymmetric and broad. For $k \leq 1$ the PDF transforms to an exponential function. ϑ determines the dispersion of the distribution function and indicates how stretched or squeezed the distribution is. The mean value is $\mu = k \cdot \vartheta$ and the variance is $\sigma^2 = k \cdot \vartheta^2$. The PDF has the property that the ratio $\sigma/\mu = 1/\sqrt{k}$ is a constant for a given shape parameter k. This means that for a fixed k and chang-

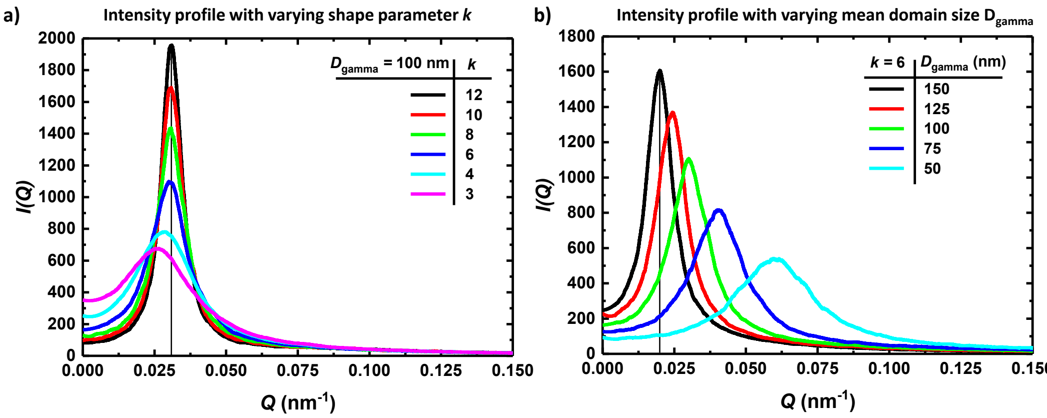

Figure 5.8: a) Intensity profiles of modeled one-dimensional domain patterns with gamma-distributed domain sizes with varying shape parameter k. The average domain size has been set to $D_{\mathrm{gamma}} = 100$ nm. With decreasing k the intensity profile gets increasingly asymmetric. b) Modeled intensity profiles with varying average domain size D_{gamma}. The shape parameter has been set to $k = 6$. The peak position of the profiles shift towards larger Q values with decreasing D_{gamma}. Additionally, the width increases together with a reduction of peak intensity, towards larger Q values.

ing μ, the standard deviation σ also changes and is thus adjusted to the mean value. The mean value corresponds to the average domain size D of the one-dimensional maze pattern, which is named D_{gamma} in the following.

Figure 5.8 illustrates the evolution of the intensity profiles obtained from generated one-dimensional domain patterns with varying shape parameter k (Fig. 5.7 (a)) and average domain size D_{gamma} (Fig. 5.7 (b)). On the one hand, it is found that the modeled intensity profile with fixed $D_{\mathrm{gamma}} = 100$ nm gets increasingly asymmetric and broad with smaller k values, together with a shift of the peak position Q_{max} towards smaller Q. The deviation of the peak positions with respect to the symmetric Gaussian profile ($k = 12$) ranges from 0.7% for $k = 10$ to 17% for $k = 3$. Furthermore, the amplitude drops upon decreasing k. On the other hand, the intensity profile with fixed $k = 6$ shifts towards larger Q with decreasing domain size D_{gamma}, as expected, due to the fact that a linear scaling in real space reflects an inverse scaling in Fourier space. In particular, in addition to the shift, a variation in width and amplitude toward larger Q is observed. The same behavior appears for any k parameter in the range of $k = 2 - 12$. The FWHM widths of the profiles ΔQ are found to be proportional to their peak position Q_{max} with $\Delta Q/Q_{\mathrm{max}} =$ constant. This relation reflects the property of the gamma PDF that $\sigma/\mu =$ constant for a fixed k. Besides, the peak intensity $I(Q_{\mathrm{max}})$ is inversely proportional to ΔQ and Q_{max} and the integral of each profile remains constant with changing D_{gamma}. Therefore, it seems that with

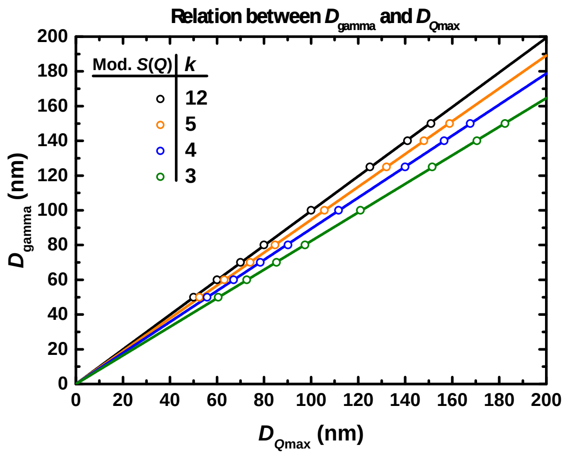

Figure 5.9: Relation between the domain size $D_{\text{gamma}} = k \cdot \vartheta$ and $D_{Q\text{max}} = \pi/Q_{\text{max}}$ for different shape parameters k (colored circles). The colored lines are linear fits to the data and reveal a linear dependency between both quantities. For $k = 12$ it is found that $D_{\text{gamma}} = D_{Q\text{max}}$. In this case, the gamma PDF resembles a Gaussian. An increasing deviation between D_{gamma} and $D_{Q\text{max}}$ with decreasing shape parameter and thus increasing asymmetry is observed.

decreasing D_{gamma} and increasing Q_{max} and ΔQ, the intensities are distributed over a larger range, resulting in a decrease of $I(Q_{\text{max}})$.

Figure 5.9 shows the relation between D_{gamma} and $D_{Q\text{max}}$ for different shape parameters k (colored circles). $D_{Q\text{max}}$ is calculated from the peak position Q_{max} of the modeled intensity profiles via $D_{Q\text{max}} = \pi/Q_{\text{max}}$, which is generally done in the literature (see e.g., [64, 72, 215]). Linear fits to the data reveal a linear dependency between both quantities (colored lines). For $k = 12$, it is found that $D_{\text{gamma}} = D_{Q\text{max}}$ and thus no deviation is observed. In this case, as described above, the gamma distribution resembles a Gaussian distribution which represents a domain pattern with high spatial order. A discrepancy of D_{gamma} and $D_{Q\text{max}}$ is observed for shape parameters $k < 12$ which increases with decreasing k and thus domain patterns with increasing spatial disorder. The discrepancy amounts to $\Delta D = (D_{Q\text{max}} - D_{\text{gamma}})/D_{\text{gamma}} = 6\%$ for $k = 5$, $\Delta D = 12\%$ for $k = 4$ and $\Delta D = 21\%$ for $k = 3$. Hence, it is found that for the case of highly disordered maze domain patterns, the average domain size of the real-space domain pattern is significantly overestimated in the framework of the generally used method.

Hellwig et al. [64] discovered a similar relation by means of an XRMS experiment. The authors found a shift of the first-order peak of the intensity profile to lower Q_{max} in the transition from a spatially aligned stripe pattern to a disordered maze pattern.

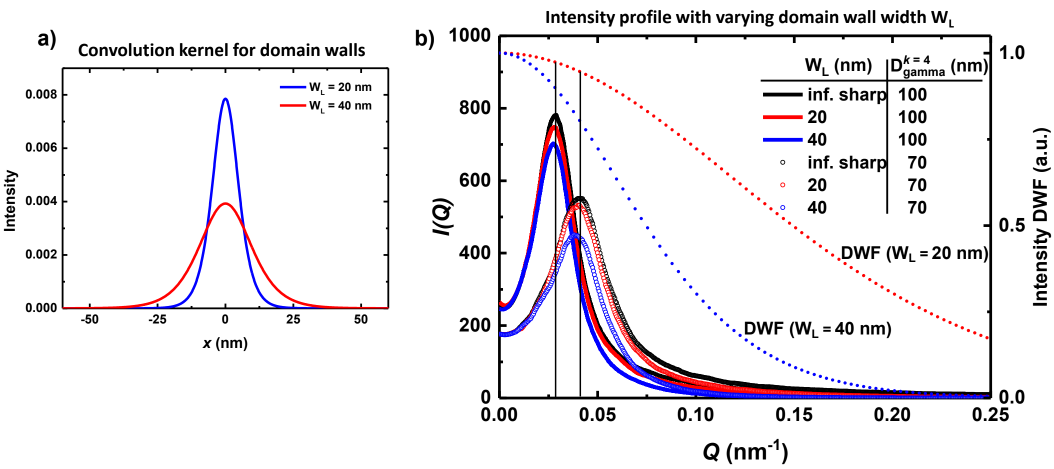

Figure 5.10: a) Convolution kernel of the domain wall profile for domain wall widths of $\mathrm{W_L} = 20$ nm and $\mathrm{W_L} = 40$ nm. b) Intensity profiles of generated one-dimensional domain patterns with gamma-distributed domain sizes with varied wall widths. The intensity profile is only slightly affected by the implementation of a finite domain wall width into the model. With increasing wall width the peak slightly shifts towards smaller Q. In addition, the width of $I(Q)$ is reduced, together with a reduction of intensity.

Miguel et al. [197] concluded that the latter implies that $Q_{\max}$ tends to overestimate the real average domain size in the disordered case and supposed that the overestimation is the reason for the observed deviation in average domain size derived from MFM and XRMS measurements.

As a further refinement to the model, a hyperbolic-tangent domain wall profile with a Bloch wall width according to the definition of Lilley [18, 216] is implemented by convolving the +/-1 stepwise transitions, i.e., the one-dimensional domain pattern with the corresponding kernel prior to performing the FFT [73] (see Fig. 5.10 (a)). The kernel is obtained from the derivative of the hyperbolic-tangent domain wall profile and is given by

$$
\begin{gathered}
f_{\text{wall}}\left(x\right) = \frac{\pi}{2\mathrm{W_L}} \frac{1}{\left(\cosh\left(\pi x/\mathrm{W_L}\right)\right)^2}. \\
\mathrm{W_L} = \pi\sqrt{\frac{A}{K}}.
\end{gathered}
\tag{5.3}
$$

$\mathrm{W_L}$ is the Bloch wall width according to Lilley [216], where A is the exchange stiffness and K is the sum of effective first $K_{1,\text{eff}}$ and second order K_2 anisotropy constants [217]. The convolution kernel is normalized such that the total sum of the kernel equals one. The reason for using a normalized kernel is to ensure that the magnetization remains unchanged by introducing finite-width domain walls (see Fig. 5.7 (a)). Fig. 5.10 (a) shows the convolution kernels for $\mathrm{W_L} = 20$ nm and $\mathrm{W_L} = 40$ nm.

The impact of finite domain walls on the modeled intensity profiles can be explained through the introduction of a domain wall factor (DWF) in Fourier space. As the intensity profile is the squared modulus of the Fourier transform of the one-dimensional domain pattern convolved with the kernel for the domain walls, the convolution property of the Fourier transform can be used to separate both contributions ($|\mathcal{F}\{M * f_{\mathrm{wall}}\}|^2 = |\mathcal{F}\{M\}|^2 \, |\mathcal{F}\{f_{\mathrm{wall}}\}|^2$). This ends up in the product of the squared modulus of the Fourier transform of the one-dimensional domain pattern and the squared modulus of the Fourier transform of the convolution kernel. The latter contribution is called domain wall factor. Figure 5.10 (b) illustrates the evolution of the intensity profiles (fixed $k = 4$ and $D_{\mathrm{gamma}} = 100$ nm and 70 nm) of a one-dimensional domain pattern with infinitely sharp domain walls (black profile) and Bloch walls with a width of $\mathrm{W_L} = 20$ nm (red profile) and $\mathrm{W_L} = 40$ nm (blue profile). The red profiles for $D_{\mathrm{gamma}} = 100$ nm and $D_{\mathrm{gamma}} = 70$ nm correspond to the product of the black profiles and the DWF with $\mathrm{W_L} = 20$ nm. The same applies to the blue profiles and the DWF with $\mathrm{W_L} = 40$ nm. It is found that the DWF shifts the peak position (black profiles) slightly towards smaller Q together with a drop of intensity. Both effects become larger with increasing domain wall width $\mathrm{W_L}$. The peak shift amounts to 0 % − 2 % in case of $\mathrm{W_L} = 20$ nm and to 2 % − 5 % in case of $\mathrm{W_L} = 40$ nm. Furthermore, the intensity drop amounts to 4 % − 7 % and 10 % − 16 % for $\mathrm{W_L} = 20$ nm and $\mathrm{W_L} = 40$ nm, respectively. The peak shift can be explained by the fact that the DWF reduces the scattering intensity below and above the peak maximum Q_{max} in an asymmetric manner. This means that the right side lobe of $I(Q)$ falls off faster towards larger Q where the left side lobe remains almost unaffected. The same behavior has been found by Pfau et al. [73] describing the influence of domain walls on magnetic diffraction patterns. A detailed description of their findings is given in [218]. The peak shift due to the DWF depends strongly on the symmetry of the intensity profile. For $k = 12$ no peak shift is observed and only the intensity decreases. A reduction of the integrated intensity of the intensity profiles in Fourier space due to the DWF is directly proportional to the reduction of the average absolute squared value of the magnetization $\left\langle |\mathrm{M}/\mathrm{M_s}|^2 \right\rangle$ within the one-dimensional domain pattern in real space.

Figure 5.11 shows the relation between D_{gamma} and $D_{Q\mathrm{max}}$ for different shape parameters k and using a domain wall width of $\mathrm{W_L} = 40$ nm within the model. It

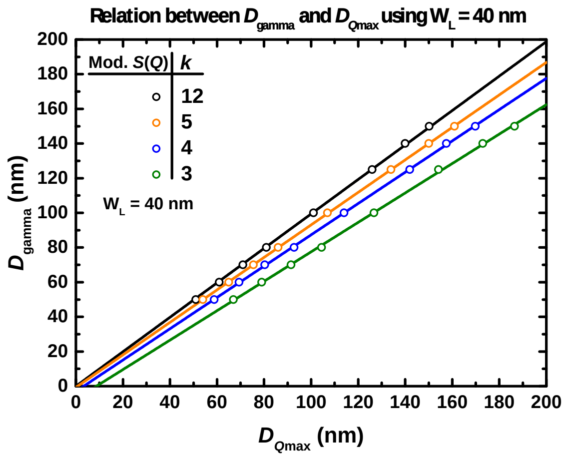

Figure 5.11: Relation between the domain size D_{gamma} and $D_{Q\mathrm{max}}$ for different shape parameters k (colored circles) and using a domain wall width of $\mathrm{W_L} = 40$ nm. Just as in case of infinitely sharp domain walls, D_{gamma} and $D_{Q\mathrm{max}}$ show a linear dependency (colored lines). For $k = 12$, the effect of the DWF on $D_{Q\mathrm{max}}$ is negligibly small and $D_{\mathrm{gamma}} = D_{Q\mathrm{max}}$ still applies. For $k < 12$, the DWF shifts the peak position towards smaller Q values and thus results in larger $D_{Q\mathrm{max}}$. This leads to slightly larger discrepancies of D_{gamma} and $D_{Q\mathrm{max}}$ compared to the case of infinitely sharp domain walls. In addition, the effect of the DWF on $D_{Q\mathrm{max}}$ increases slightly with decreasing average domain sizes D_{gamma}. This gives rise to a small shift of the linear fit function with respect to the origin.

can be seen that the linear dependency between both quantities found for the case of infinitely sharp domain walls still applies (colored lines). For $k = 12$, the shift of Q_{max} due to the DWF is negligible small and the relation $D_{\mathrm{gamma}} = D_{Q\mathrm{max}}$ remains unchanged. In this case, the DWF only reduces the intensity of the modeled intensity profiles. For, $k < 12$ the peak position Q_{max} is shifted towards smaller Q due to the DWF which results in increased $D_{Q\mathrm{max}}$ values. It follows that the discrepancy between D_{gamma} and $D_{Q\mathrm{max}}$ is further increased. The discrepancy amounts to $\Delta D = 7\% - 8\%$ for $k = 5$, $\Delta D = 14\% - 17\%$ for $k = 4$ and $\Delta D = 24\% - 33\%$ for $k = 3$. Comparing these values with the ones obtained in case of infinitely sharp domain walls, see above, it is found that the discrepancy is mainly attributed to the shift of the peak position due to the increased asymmetry for $k < 12$ (see Fig. 5.8 (a)) and thus to an increased spatial disorder of the real-space domain pattern. However, the DWF results in an additional contribution to the discrepancy which increases with decreasing shape parameter k. In addition, it is found that the contribution of the DWF to the discrepancy is also slightly increased with decreasing D_{gamma}. This is

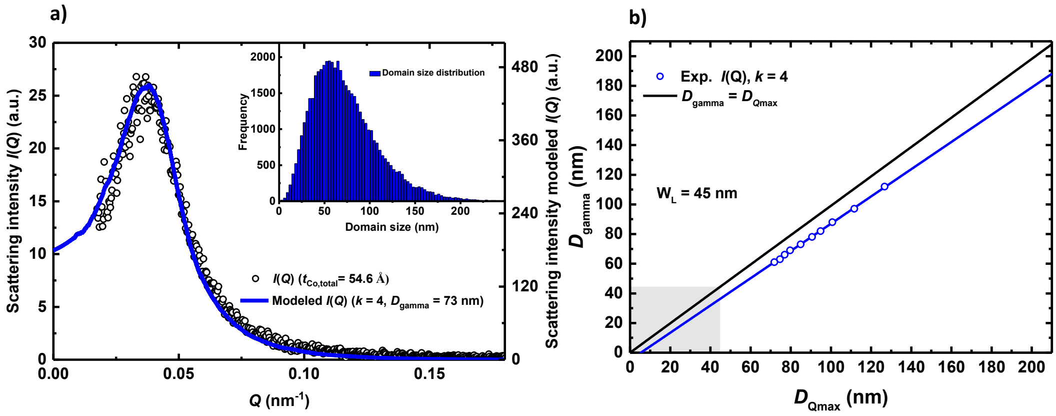

Figure 5.12: a) Radial scattering intensity profile extracted from the diffraction pattern at $t_{\mathrm{Co,total}} =$ 54.6 Å (open symbols) and the corresponding modeled intensity profile (blue solid line) obtained by an absolute squared FFT of a one-dimensional domain pattern with gamma-distributed domain sizes. A histogram of this distribution is shown in the inset. A shape parameter of $k = 4$ and an average domain size of $D_{\mathrm{gamma}} = 73$ nm are used as input parameter. b) Relation between the domain size D_{gamma} and $D_{Q\mathrm{max}}$. Values from the intensity profiles fitted to the experimental data are given by blue filled circles. The black line illustrate the Gaussian distribution where $D_{\mathrm{gamma}} = D_{Q\mathrm{max}}$. The grey area indicate the used domain wall width $\mathrm{W_L} = 45$ nm.

represented by a shift of the linear fit functions with respect to the origin which amounts to 1.4 nm for $k = 5$, 3.4 nm for $k = 4$ and 9 nm for $k = 3$.

5.3.3 Application of the 1D model to the experimental data

In the following, modeled intensity profiles of one-dimensional domain patterns with gamma-distributed domain sizes are used to fit the measured radial scattering intensity profiles obtained from the XRMS experiment (see Fig. 5.5). As an example, a comparison of the profile measured at $t_{\mathrm{Co,total}} = 54.6$ Å and the modeled profile using a scale parameter of $\vartheta = 18.3$ and a shape parameter of $k = 4$ is shown in Fig. 5.12 (a). A domain wall width of $\mathrm{W_L} = 45$ nm is assumed, which is the average value calculated in the span of $K_{1,\mathrm{eff}}$ and K_2 determined from the intensity profiles (see section 5.4.2). In the latter range, the domain wall width changes only slightly $\Delta\mathrm{W_L} \approx \pm 5$ nm and the impact on the average domain sizes and intensity profiles is thus in first approximation negligible. The modeled intensity profiles are scaled in

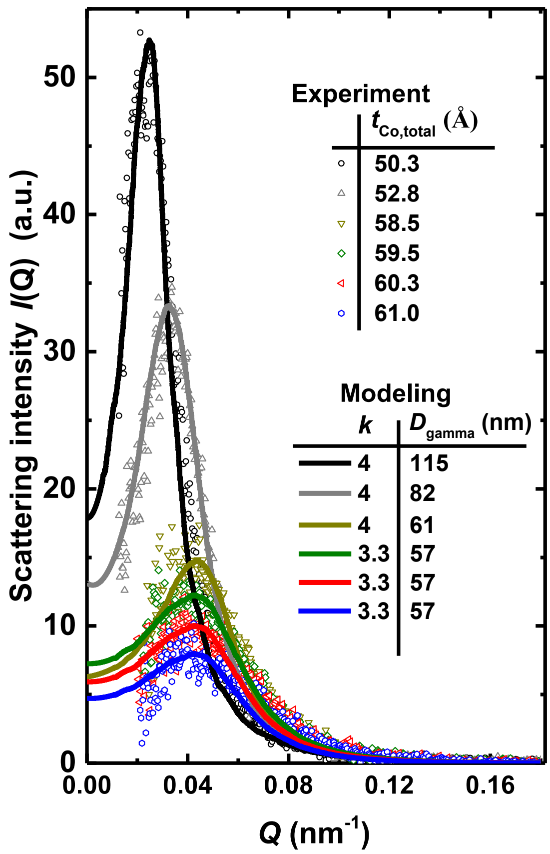

Figure 5.13: Radial scattering intensity profiles extracted from the measured diffraction patterns via azimuthal averaging (colored symbols). The solid lines are modeled intensity profiles resulting from an absolute squared FFT of one-dimensional domain patterns with gamma-distributed domain sizes.

intensity to match the measured ones. The same operation results in a good agreement of the modeled and measured intensity profiles up to a Co thickness of t_{critical}. A one-dimensional average domain size $D_{\mathrm{gamma}} = k \cdot \vartheta = 73$ nm is obtained from Fig. 5.12 (a), whereas the domain size calculated from the peak position results in $D_{Q\mathrm{max}} = 85$ nm. Thus, the analysis reveals a discrepancy between D_{gamma} and $D_{Q\mathrm{max}}$ which amounts to $\Delta D = 16\%$ in this case. The discrepancy of both values is attributed to the shift of the peak position due to the increased asymmetry for $k = 4$ on the one hand (see Fig. 5.9) and the influence of the domain wall ($\mathrm{W_L} = 45$) on the other hand (see Fig. 5.11). Figure 5.12 (b) shows the relation between D_{gamma} and $D_{Q\mathrm{max}}$ for different Co thicknesses along the wedge and reveals a linear dependency

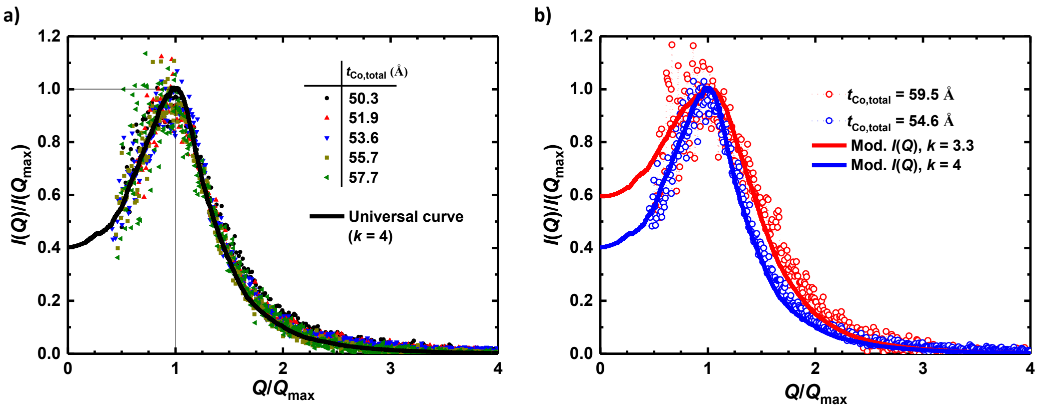

Figure 5.14: a) Normalized radial scattering intensity profiles in the thickness range of $t_{\mathrm{Co,total}} =$ 50.3 Å to 57.7 Å. Every second profile is plotted for clearer representation. The black curve displays the normalized intensity profile with a shape parameter $k = 4$ which is denoted as a universal curve for all profiles. b) Radial scattering intensity profile at $t_{\mathrm{Co,total}} = 54.6$ Å normalized to the peak maximum and position Q_{max} (blue open symbols). For comparison, a normalized profile at $t_{\mathrm{Co,total}} = 59.5$ Å is plotted (red open symbols). The widths of both profiles are different, indicating a structural change of the domain pattern at t_{critical}. The modeled data indicate a change of the shape parameter of the gamma distribution from $k = 4$ to 3.3 (red and blue lines).

of both values. In Fig. 5.12 (b) the blue filled symbols correspond to the experimental findings of all intensity profiles below t_{critical} and the blue line is a linear fit to the data. It can be seen that the linear fit function does not pass through the origin of the graph and is slightly shifted (5.9 nm). This is due to the fact that the shift of the peak position Qmax slightly increases with decreasing average domain sizes caused by the influence of the DWF, as described above (see Fig. 5.11).

The presented model reveals a good agreement of the measured and modeled intensity profiles (see Fig. 5.13). In the total Co thickness range of $t_{\mathrm{Co,total}} = 50.3 - 58.5$ Å average domain sizes of $D_{\mathrm{gamma}} = 115$ nm to 61 nm are obtained. It is found that the shape parameter k remains unchanged over this Co thickness range. The model demonstrates that the observed variation of peak widths and reduction of intensity (see Fig. 5.13 and Fig. 5.5 (b)) originates from the change of ϑ at constant k and hence from a change in average domain size D_{gamma} (see Fig. 5.8). This implies that the maze pattern is scale invariant in the above-mentioned thickness range and shows an intrinsic symmetry, represented by the shape parameter k, independent of the Co thickness or average domain size D_{gamma}. This behavior reflects the property of the gamma PDF that it is a scaled distribution where the standard deviation is scaled to the average domain size. It follows, that the probed maze patterns exhibit the same property. The latter is also evident directly from the measurements, when normalizing the measured radial scattering intensity profiles to the individual peak maxima $I(Q_{\max})$ and position $Q_{\max}$. By means of the normalization all profiles fall onto a universal curve (Fig. 5.14 (a)). A comparable behavior, i.e., a scale invariance, has been observed by Malik et al. [219]. The authors find that although the domain structure of sodium borosilicate glass evolves during phase separation, it remains scale invariant at all times leading to a universal curve for all measured intensity profiles.

One observation shown in Fig. 5.5 (b) and Fig. 5.13 has not been discussed so far. It is found that beyond a total Co thickness of $t_{\mathrm{Critical}} = 58.5$ Å the shape of the radial intensity profile remains constant in Q (Fig. 5.5 (b)). The latter involves, according to the model, that the domain size does not change anymore. However, the amplitude of the intensity profile continues to drop for the remaining three intensity profiles at $t_{\mathrm{Co,total}} = 59.5$ Å, $t_{\mathrm{Co,total}} = 60.3$ Å and $t_{\mathrm{Co,total}} = 61$ Å. From that it can be deduced that the reduction of intensity has apparently a different origin. Due to the fact that the scattering intensity depends on the square of the out-of-plane component of the magnetization M_z^2 (see Eq. 2.41), the relation of the intensity profile above t_{Critical} could be explained by a reduction of this component. The latter effect can be expected within the spin-reorientation transition, where the magnetization changes from the out-of-plane to an in-plane orientation via canting of the magnetization direction [9, 166, 198, 220, 221]. The model reveals, in addition, that the shape parameter changes from $k = 4$ to 3.3 (see Fig. 5.14 (b)) above t_{Critical} which indicates a modification of the domain size distribution and hints to changes of the magnetic microstructure. As before, the radial intensity profiles in this range are best described by an identical shape parameter $k = 3.3$. The findings indicate that not only the magnetization canting sets in but also that the domain pattern changes its characteristics. The broadening of the profile above t_{Critical} cannot be explained by a decrease of domain wall width or decreasing influence of the DWF. This is due to the fact that the symmetry of the intensity profile is only slightly affected by the DWF and would thus not result in the significant broadening shown in Fig. 5.14 (b). In addition, a further increase and not a decrease of the domain wall width in the canting regime with increasing $t_{\mathrm{Co,total}}$ is expected [217].

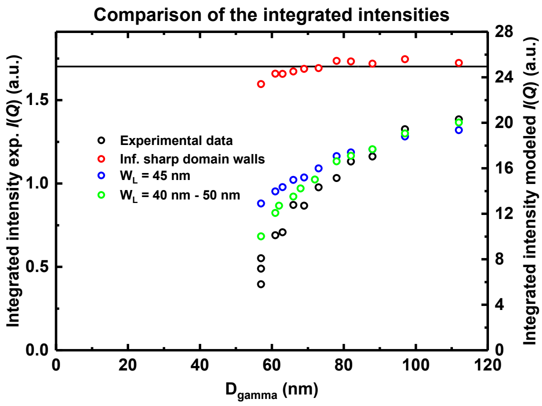

Figure 5.15: Integrated intensities of the measured and modeled intensity profiles as a function of the average domain size D_{gamma}. The black circles correspond to the intensities obtained from the experimental data. The red circles represent the integrated intensities of modeled intensity profiles with infinitely sharp domain walls, the blue circles with constant domain wall width of $\mathrm{W_L} = 45$ nm and the green circles with varying domain wall width from $\mathrm{W_L} \approx 40$ nm to 50 nm.

5.3.4 Comparison of the 1D integrated intensities of the measured and modeled intensity profiles

Figure 5.15 displays the one-dimensional integrated intensities of the measured and modeled intensity profiles as a function of the average domain sizes D_{gamma} obtained from the above analysis. The red circles correspond to the integrated intensity of modeled intensity profiles with infinitely sharp domain walls. In this case, the modeled profiles do not fit to the measured profiles. However, in this case, the integrated intensities remain constant with changing D_{gamma}, as mentioned before (see section 5.3.2). The small fluctuations of the data are caused by the use of slightly different integration ranges defined by the accessible Q-space ranges of the measured data. They occur due to slightly different masks used to mask out the superimposed projection image of the membrane window in the magnetic diffraction patterns (see Fig. 5.5 (a)). The black circles represent the integrated intensities of the measured radial scattering intensity profiles and the blue circles of their corresponding fits from the model and constant $\mathrm{W_L} = 45$ nm. A slightly different relative decrease of intensity is observed by comparing both curve shapes, where the measured data show a stronger decrease. The stronger decrease with D_{gamma} or $t_{\text{Co,total}}$ increase cannot be explained by an increasing absorption, which is not included in the model, since variations in absorption in the small probed thickness range can be neglected. One possible explanation would be a slightly stronger intensity decrease caused by an increasing domain wall width with decreasing D_{gamma}. An increasing domain wall width results in a decreasing width of the DWF and hence leads to a slightly stronger reduction of intensity (see Fig. 5.10). As mentioned before, the impact of the small change of domain wall width calculated in the span of K_1 and K_2 determined from the intensity profiles is in first approximation negligible, in particular with regard to the average domain size. However, a slightly stronger influence on the intensity can be found. The integrated intensities of modeled intensity profiles with varying domain wall width are shown in Fig. 5.15 (green circles). A stronger reduction of intensity is observed and the curve shape reveals a similar behavior to the experimental data. A second explanation for the stronger reduction of intensity in the experimental data, in particular at small D_{gamma}, could be the influence of magnetization canting on the radial intensity profiles. This will be addressed in more detail in the next chapter. The beam size has a FWHM width of 25 μm in horizontal direction and thus along the Co wedge and scan direction. The diffraction patterns are recorded with a step size of 10 μm. Hence, it can be expected that the SRT is not found to be abrupt at a certain Co thickness in the experimental data, but rather through a smeared out transition. Consequently, extracted radial intensity profiles at Co thicknesses close to the SRT can exhibit a mixed influence from a changing average domain size and diminishing out-of-plane magnetization due to canting. The intensity profile has a quadratic dependence on the out-of-plane component of the magnetization and thus small changes have a non-negligible impact. The influence of mixed contributions close to the SRT can be avoided in future experiments through the fabrication of shallower wedges, where changes of the physical properties of the sample are distributed over a larger spatial area.

5.4 Determination of magnetic anisotropy constants

In this section, the results obtained from the one-dimensional domain model are used to determine the magnetic anisotropy constants of the Co/Pd wedge sample at different Co thicknesses along the wedge. The following magnetic analysis is used as an independent consistency check of the above-described analysis of the data (section 5.3.3). For a proper understanding of the magnetic analysis a brief introduction to micromagnetism is presented, where the focus is on Co/Pd and Co/Pt thin films (section 5.4.1). Subsequently, the one-dimensional average domain sizes obtained from the above-described analysis are used to determine the first- and second-order anisotropy constants (section 5.4.2). Then, the amplitudes of the intensity profiles above t_{Critical} are utilized to determine the first-order anisotropy constants in the regime of magnetization canting (section 5.4.3). Finally, the first-order anisotropy constants are used to determine the bulk and interface anisotropy (section 5.4.4).

5.4.1 Fundamentals of micromagnetism

Free energy density and magnetic anisotropy

Properties that characterize ferromagnetic materials are the magnetic anisotropy constants K_{i}, exchange stiffness A, and saturation magnetization M_{S}. The property of ferromagnetic materials to possess a preferred orientation of magnetization (easy axis) is known as magnetic anisotropy [18, 186, 222]. The energy needed to rotate the magnetization direction from its favored easy axis to an unfavored hard axis is defined as the magnetic anisotropy energy. If only one easy axis of magnetization exists this is referred to as uniaxial anisotropy, as it is ,e.g., for hexagonal Co, where the c-axis corresponds to the easy axis of magnetization [223]. The free energy density of the system depends on the relative orientation of the magnetization direction with respect to the outstanding axis. The free energy density of a magnetic thin film with uniaxial anisotropy in second-order approximation is given by [222, 224]

$$F = K_{1,\mathrm{eff}} \sin^2 \theta + K_2 \sin^4 \theta, \tag{5.4}$$

where $K_{1,\mathrm{eff}}$ and K_2 are the effective first-order and second-order anisotropy constants. θ is the angle between the c-axis and the magnetization direction. The effective first-order anisotropy constant consists of three energy contributions with different origins and is expressed by

$$K_{1,\mathrm{eff}} = K_{1V} + \frac{2K_{1S}}{t} - \frac{\mu_0}{2} M_{\mathrm{S}}^2, \tag{5.5}$$

where K_{1V} is the volume anisotropy, K_{1S} are the surface and interface contributions of the anisotropy and t is the single-layer thickness. The last term in Eq. 5.5 represents the shape anisotropy for thin films with the saturation magnetization M_{S}. In case of Co/Pt(111) and Co/Pd(111) thin films, $K_{1,\mathrm{eff}}$ consists of the anisotropy constants K_{1V}, K_{1S}, and the shape anisotropy, since all contributions are uniaxial with regard to the stacking direction.

The volume anisotropy K_{1V} results from the coupling of the spin to the crystal lattice due to the spin-orbit coupling and is thus linked to the symmetry of the lattice. For hexagonal Co, the volume anisotropy prefers an orientation of the magnetization along the c-axis. Volume anisotropies in the range of $K_{1V} = 0.6 - 1.2$ MJ/m^3 can be found for Co/Pd(111) multilayers in the literature [186, 187, 225–227]. For fcc Co, the easy axes are along the fcc(111) directions and the corresponding cubic anisotropy constants are one order of magnitude smaller than K_{1V} for hcp Co owing to the higher symmetry of the fcc lattice [222, 224].

The surface or interface anisotropy K_{1S} is a consequence of the symmetry breaking at surfaces and interfaces [228]. The contribution of both surfaces of a thin film is considered by the prefactor 2 in Eq. 5.5. For Co/Pt(111) and Co/Pd(111) films, K_{1S} prefers an orientation of the magnetization perpendicular to the surface. For Co/Pd(111) multilayers, values in the range of $K_{1S} = 0.16 - 0.74$ mJ/m^2 are found in the literature [186, 187, 225–227].

The shape anisotropy (magnetostatic self-energy) arises from magnetic poles at the surfaces and prefers an alignment of the magnetization parallel to the surface. Thus, it counteracts the other two anisotropy contributions. Using the saturation magnetization at room temperature for Co, $M_\mathrm{S} = 1446$ kA/m [224], the shape anisotropy amounts to $\mu_0 M_\mathrm{S}^2/2 = 1.31$ MJ/m^3.

The second-order anisotropy constant K_2 has in principle also a magneto crystalline surface and volume contribution. However, for Co/Pt films it has been found experimentally that K_{2S} is almost zero and that K_2 is mainly determined by its volume contribution K_{2V} [164, 229].

As the contributions of the effective first-order anisotropy constant are competing with each other and the interface anisotropy scales inversely with the thickness of the Co layer, an easy axis parallel to the film normal can be obtained at small Co layer thicknesses, where the interface contribution is the dominant part. With increasing Co thickness the contribution of K_{1S} decreases and the shape anisotropy dominates. The latter results in a decreasing effective first-order anisotropy constant and eventually gives rise to a sign change. Thus, at larger Co layer thickness the magnetization direction favors an orientation parallel to the surface. The thickness-driven transition from an easy axis parallel to the film normal to an easy axis parallel to the surface is called thickness-driven spin-reorientation transition. For a detailed introduction to micromagnetism and magnetic anisotropies it is referred to [18, 186, 222, 223].

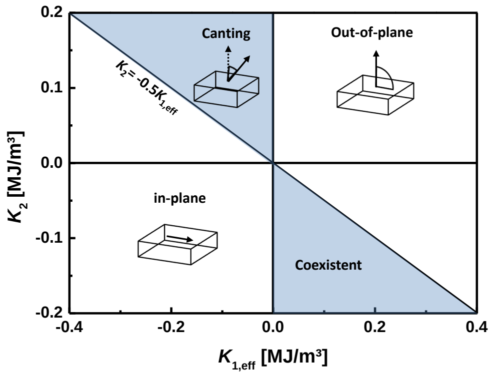

Figure 5.16: Phase diagram in anisotropy space ($K_{1,\text{eff}}/K_2$), which show different regions of the easy axis of magnetization as a function of effective first-order and second-order anisotropy constants. The blue shaded areas correspond to the regions of canted and coexistence phase.

Thickness-driven spin-reorientation transition

The thickness-driven spin-reorientation transition (SRT) in magnetic thin films describes a phase transition affected by a change of the easy axis under the variation of film thickness [9, 221]. The SRT can take place, in general, via the state of canted magnetization ($K_2 > 0$) [183, 220, 230, 231] or via the coexistence phase ($K_2 < 0$) [221, 232]. In the canted phase, the easy axis includes an angle $0° < \theta_\text{c} < 90°$ with respect to the surface normal, while θ_c decreases gradually with increasing thickness. In the coexistence phase, in-plane and out-of-plane domains coexist, while the amount of the latter decreases with increasing thickness.

In second-order approximation a phase diagram (in $K_{1,\text{eff}}/K_2$ space) can be put forward [9, 221, 233] (see Fig. 5.16) to describe the easy axis orientation depending on the effective first-order and second-order anisotropy constants. In case of $K_2 > 0$, the easy axis is parallel to the film normal for $K_{1,\text{eff}} \geq 0$ and perpendicular to the film normal for $K_{1,\text{eff}} < -2K_2$. The intermediate region $-2K_2 \leq K_{1,\text{eff}} < 0$ represents the canted phase. The canting angle θ_c in this region, i.e., the equilibrium orientation of magnetization with respect to the film normal, can be expressed in terms of the effective first and second-order anisotropy constants as follows [221, 234]

$$\sin^2\theta_\text{c} = -\frac{K_{1,\text{eff}}}{2K_2}. \tag{5.6}$$

In case of $K_2 < 0$, the easy axis is parallel to the film normal for $K_{1,\text{eff}} < -2K_2$ and perpendicular to the film normal for $K_{1,\text{eff}} \leq 0$. The intermediate region represents the coexistence phase. For Co/Pt(111) and Co/Pd(111) thin films, it has been found that the SRT proceeds via a state of canted magnetization [198, 231, 234, 235].

Magnetic domains in thin films with PMA

A magnetic thin film with PMA is able to lower the magnetostatic self-energy through the creation of magnetic domains which are separated by domain walls. The gain in dipolar energy with decreasing domain size is counterbalanced by the excess in domain wall energy. Thus, the minimum of the total energy of domain wall and dipolar energy determines the equilibrium domain size. With decreasing $K_{1,\mathrm{eff}}$, i.e., with increasing Co layer thickness (see Eq. 5.5), the domain wall energy density becomes smaller which allows for a more efficient reduction of the dipolar energy. The latter gives rise to smaller domain sizes with increasing Co layer thickness.

An analytical description of the average domain size for single layer films with PMA was first proposed by Kaplan and Gehring [188] and proven to be valid by Millev [236]. In [188], the authors deduce an analytical approximation of the infinite series for the magnetostatic energy of thin films [190] assuming that the domain wall width is much smaller than the domain size. In addition, they investigate the influence of the domain morphology on the domain size. The analytical expression for the average domain size D as a function of domain wall energy density γ_w, magnetostatic energy density E_ms and single layer thickness t is given by [188, 198]

$$D\left(\gamma_\mathrm{w}, t\right) = t \cdot B \cdot \exp\left[\frac{\pi}{2} \cdot \frac{\gamma_\mathrm{w}}{E_\mathrm{ms} \cdot t}\right], \tag{5.7}$$

where B is a geometry parameter representing the domain morphology. The geometry parameter $B = 0.955$ for a stripe, $B = 2.525$ for a checkerboard [188], and $B = 2.45$ for a maze pattern [198, 229]. The magnetostatic energy is $E_\mathrm{ms} = \mu_0 M_\mathrm{S}^2/2$ as described above.

For the case $K_{1,\mathrm{eff}} \geq 0$ and $K_2 > 0$, i.e, in the range of PMA, the domain wall energy density for Bloch walls in second-order approximation is given by [217]

$$\gamma_\mathrm{w} = 2\sqrt{AK_{1,\mathrm{eff}}}\left\{1 + \frac{K_{1,\mathrm{eff}} + K_2}{\sqrt{K_{1,\mathrm{eff}}K_2}} \arcsin\left[\sqrt{\frac{K_2}{K_{1,\mathrm{eff}} + K_2}}\right]\right\}, \tag{5.8}$$

and in the canting region ($-2K_2 \leq K_{1,\mathrm{eff}} < 0$, $K_2 > 0$) by

$$\gamma_{\mathrm{w,c}}(\theta_{\mathrm{c}}) = \frac{\pi}{2}(K_{1,\mathrm{eff}} + 2K_2)\sqrt{\frac{A}{K_2}} = \pi\sqrt{AK_2}\cos^2\theta_{\mathrm{c}}, \tag{5.9}$$

where A is the exchange stiffness. The second expression in Eq. 5.9 follows from a rearrangement of the first expression and substitution of Eq. 5.6. It gives the domain wall energy density in the canting region as a function of the canting angle θ_{c}. The magnetostatic energy is also reduced due to canting and is expressed by

$$E_{\mathrm{ms,c}}(\theta_{\mathrm{c}}) = \frac{\mu_0}{2}M_{\mathrm{S}}^2\cos^2\theta_{\mathrm{c}}. \tag{5.10}$$

Substitution of Eq. 5.9 and Eq. 5.10 into Eq. 5.7 results in an expression for the domain size D in the canting region

$$D_{\mathrm{c}}\left(K_2, t\right) = t \cdot B \cdot \exp\left[\frac{\pi^2}{\mu_0} \cdot \frac{\sqrt{AK_2}}{M_{\mathrm{S}}^2 \cdot t}\right]. \tag{5.11}$$

Equation 5.11 reveals that the domain size in the canting regime depends only on K_2 and thickness t and is independent of $K_{1,\mathrm{eff}}$ and θ_{c}. It demonstrates that a collapse of domain size for $K_{1,\mathrm{eff}} \to 0$, as it is demonstrated for the coexistence phase, is prevented [229, 237]. The change of $K_{1,\mathrm{eff}}$ only affects the canting angle (see Eq. 5.6).

The analytical solutions given above for single thin films are based on the assumptions that the approximation of the infinite series for the magnetostatic energy density is also valid for the canting phase and that the domain size is large compared to the domain wall width. According to Lilley [216], the domain wall width in second order approximation for $K_{1,\mathrm{eff}} \geq 0$ and $K_2 > 0$ is given by [217]

$$W_{\mathrm{L}} = \frac{\pi\sqrt{A}}{\sqrt{K_{1,\mathrm{eff}} + K_2}}, \tag{5.12}$$

and in the canting region ($-2K_2 \leq K_{1,\mathrm{eff}} < 0$, $K_2 > 0$) by

$$W_{\mathrm{L,c}} = \frac{2\pi\sqrt{AK_2}}{K_{1,\mathrm{eff}} + 2K_2}. \tag{5.13}$$

Equations 5.12 and 5.13 show that the applicability of the analytical approximation is strongly limited by the size of K_2. In the range of perpendicular magnetization and $K_{1,\mathrm{eff}} \to 0$, W_{L} strongly increases, where the domain size D decreases exponentially (see Eq. 5.7 and Eq. 5.8). The same applies to the canting regime where the domain wall width $W_{\mathrm{L,c}}$ is further increased when traversing the canted phase towards the range of in-plane magnetization. Thus, the larger the anisotropy constant K_2, the larger is the range of $K_{1,\mathrm{eff}}$ and thickness t where the analytical approximation gives reasonable results. It will be shown in the next section that for the Co/Pd wedge sample $K_2 = (114 \pm 24)$ kJ/m^3. This value is pretty large and thus enables a large $K_{1,\mathrm{eff}}$ range where the model is applicable.

5.4.2 Determination of anisotropy constants using the domain size of magnetic domain patterns

In the following, the domain sizes obtained from the XRMS experiment and the model described in section 5.3.3 together with the total Co thicknesses $t_{\mathrm{Co,total}}$ are used to determine the anisotropy constants $K_{1,\mathrm{eff}}$ and K_2 along the Co/Pd wedge in the range of perpendicular magnetization ($K_{1,\mathrm{eff}} \geq 0$). For this, the analytical expression for the domain size (Eq. 5.7) is used.

Equation 5.7 is defined for single layer films. A model for multilayer films has been given by Stickler et al. [198]. In case of a multilayer, the magnetostatic energy density depends on the film composition, i.e., the single layer thickness of the ferromagnetic material, the single layer thickness of the nonmagnetic interlayer, and the number of repetitions [238, 239]. It has been found that the magnetostatic energy density decreases on increase of number of repetitions [229]. The magnetostatic energy density for a fixed composition can be calculated numerically using the expression for the magnetostatic energy density in [238, 239]. In [238] and [239] infinitesimally sharp and freely movable domain walls are assumed, so that the state of minimal free energy is obtained.

For the Co/Pd multilayer wedge in the Co thickness range of $t_{\mathrm{Co,total}} = 50.3 - 58.5$ Å with average domain sizes of $D_{\mathrm{gamma}} = 115 - 61$ nm, the magnetostatic energy density normalized by the maximum magnetostatic energy results in $e_{\mathrm{d}} = E_{\mathrm{ms}}/0.5\mu_0 M_{\mathrm{S}}^2 = 0.9 - 0.84$.

The analytical expression for the domain size of multilayer films for $K_{1,\mathrm{eff}} \geq 0$ is then given by [198]

$$D\left(\gamma_{\mathrm{w}}, t_{\mathrm{total}}\right) = t_{\mathrm{total}} \cdot B \cdot \exp\left[\frac{\pi}{\mu_0} \cdot \frac{\gamma_{\mathrm{w}}}{e_{\mathrm{d}} M_{\mathrm{S}}^2 \cdot t_{\mathrm{total}}}\right], \tag{5.14}$$

where t_{total} is the total thickness of the ferromagnetic material.

For the calculation of the second-order anisotropy constant K_2 of the Co/Pd multilayer, Eq. 5.14 and the expression for the domain wall energy in Eq. 5.8 in the limit $K_{1,\mathrm{eff}} = 0$, i.e., where the system enters the canted phase, is used. At the point $K_{1,\mathrm{eff}} = 0$, Eq. 5.8 transforms to $\gamma_\mathrm{w} = \pi\sqrt{AK_2}$ and resembles Eq. 5.9 for $\theta_\mathrm{c} = 0°$. In the XRMS experiment, it is assumed that the system enters the canted phase at the thickness where the peak position Q_max of the radial intensity profile starts to remain constant, i.e., at $t_\mathrm{Critical} = 58.5$ Å with $D_\mathrm{gamma} = 61$ nm. The second-order anisotropy constant can now be calculated analytically and amounts to $K_2 = (114 \pm 24)$ kJ/m^3. For the calculation, the exchange stiffness of Co $A = 31.4$ pJ/m [240], $B = 2.45$ [198] and $e_\mathrm{d} = 0.84$ have been used.

To calculate the first-order anisotropy constant $K_{1,\mathrm{eff}}$ in the range of perpendicular magnetization ($t_\mathrm{Co,total} = 50.3 - 57.7$ Å) it is assumed that $K_2 = (114 \pm 24)$ kJ/m^3 is constant in this small Co thickness range. Using Eq. 5.14, the domain sizes $D_\mathrm{gamma} = 115 - 61$ nm and $e_\mathrm{d} = 0.9 - 0.84$, domain wall energies ranging from $\gamma_\mathrm{w} = (8.4 \pm 0.6)$ mJ/m^2 to (6.1 ± 0.6) mJ/m^2 are calculated analytically. The obtained domain wall energies and Eq. 5.8 can now be used to calculate the $K_{1,\mathrm{eff}}$ values numerically. The obtained first-order anisotropies vary from $K_{1,\mathrm{eff}} = (71 \pm 26)$ kJ/m^3 to (3 ± 15) kJ/m^3 over the total Co thickness range of $t_\mathrm{Co,total} = 50.3 - 57.7$ Å. The $K_{1,\mathrm{eff}}$ values are plotted in an $K_{1,\mathrm{eff}} \cdot t_\mathrm{Co,single}$ vs. $t_\mathrm{Co,single}$ diagram in Fig. 5.18.

5.4.3 Magnetization canting

It has been shown that the average domain size does not vary above t_Critical (see Fig. 5.17). In this case, the magnetic system can further decrease its magnetostatic energy density on thickness increase via canting the magnetization (SRT; see above). It is assumed in first approximation that the decrease of the magnetic scattering amplitudes above t_Critical results from the reduction of the out-of-plane component of magnetization M_z due to canting ($-2K_2 \leq K_{1,\mathrm{eff}} < 0$). The scattering signal is proportional to the square of the cosine of the canting angle θ_c

$$\frac{S_\mathrm{c}}{S_0} = \frac{|M_\mathrm{z,c}|^2}{|M_\mathrm{s}|^2} = \cos^2\theta_\mathrm{c}, \tag{5.15}$$

where S_c is the scattering amplitude with canting and S_0 with perpendicular magnetization. The starting point of the canting (normal component of $M = M_\mathrm{s}$) is set to t_Critical. Using the integrated intensities of the corresponding radial intensity profiles the canting angles can be calculated using Eq. 5.15. Canting angles from $\theta_\mathrm{c} = 19.8°$ to $37.0°$ are determined. Using the canting angles, a constant $K_2 = (114 \pm 24)$ kJ/m^3

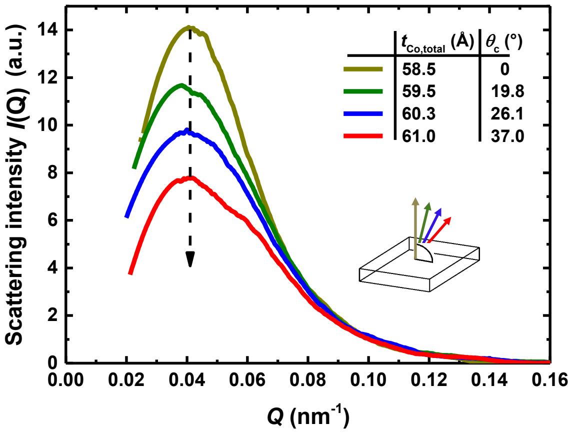

Figure 5.17: Radial scattering intensity profiles extracted from the diffraction patterns in the Co thickness range of $t_{\mathrm{Co,total}} = 58.5 - 61.0$ Å (canting region). The profiles have been smoothed for a better representation. It is assumed that the decrease of the scattering amplitude is caused by a reduction of the out-of-plane component of magnetization due to canting. The inset shows a sketch of the easy axis of magnetization as a function of canting angle θ_{c} calculated from the scattering amplitudes at different Co thicknesses $t_{\mathrm{Co,total}}$.

and Eq. 5.6, the first-order anisotropy $K_{1,\mathrm{eff}}$ in the canting regime can be calculated. The obtained first-order anisotropy constants are ranging from $K_{1,\mathrm{eff}} = (-26 \pm 21)$ kJ/m^3 to (-83 ± 25) kJ/m^3.

5.4.4 Determination of K_{1V} and K_{1S}

The results of the magnetic analysis for $K_{1,\mathrm{eff}}$ (see sections 5.4.2 and 5.4.3) can be plotted in a $K_{1,\mathrm{eff}} \cdot t_{\mathrm{Co,single}}$ vs. $t_{\mathrm{Co,single}}$ graph (see Fig. 5.18). The dependence of $K_{1,\mathrm{eff}} \cdot t_{\mathrm{Co,single}}$ on thickness $t_{\mathrm{Co,single}}$ should give a straight line if the driving parameter is the thickness (Eq. 5.5; [186]). The data below t_{Critical} fit well a line while the $K_{1,\mathrm{eff}}$ values in the canting regime ($K_{1,\mathrm{eff}} < 0$) deviate considerably from the former line. However, as the investigated Co thickness range is extremely small one can rule out substantial changes of the film structure and a linear dependence should be expected. In the thickness range below t_{Critical} the slope of the plot gives the volume anisotropy $K_{1V} = (0.93 \pm 0.04)$ MJ/m^3 while the intercept gives twice the interface anisotropy $K_{1S} = (0.14 \pm 0.02)$ mJ/m^2. These values are in the span of the reported values of Co/Pd(111) (see section 5.4.1). In particular, the values are in very good agreement with measurements of Carcia et al. [225] who found a volume

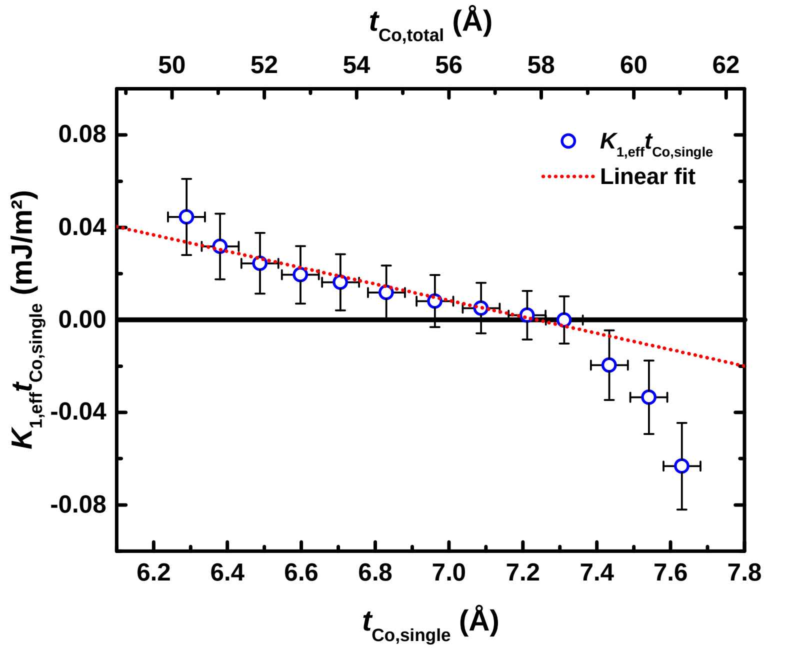

Figure 5.18: $K_{1,\text{eff}} \cdot t_{\text{Co,single}}$ versus Co thickness of the Co/Pd multilayer. The values $K_{1,\text{eff}} \cdot t_{\text{Co,single}} > 0$ (blue dots) are calculated using the analytical expression in Ref. [198] (see text), and a linear fit is shown. The values $K_{1,\text{eff}} \cdot t_{\text{Co,single}} < 0$ are calculated using the integrated scattering amplitudes and the expression for the canting angle (Eq. 5.6).

anisotropy of $K_{1V} = 0.94$ MJ/m^3 and an interface anisotropy of $K_{1S} = 0.16$ mJ/m^2 as well as an SRT occurring at $t_{\text{Co,single}} = 7.8$ Å for Co/Pd multilayers. Their samples have been prepared via rf sputtering of Co and Pd onto unheated glass and Kapton substrates. They account the high value of K_{1V} in comparison to the crystallographic value of hcp Co ≈ 0.5 MJ/m^3 for tensile strain due to the lattice mismatch between Co and Pd (9.1%) and thus for additional magnetoelastic contributions to the volume anisotropy. An in-depth discussion about the anisotropy constants is beyond the scope of this thesis and requires intensive structure investigations of the Co/Pd multilayers.

For $t > t_{\text{Critical}}$, the $K_{1,\text{eff}}$ values determined via scattering intensities do not match to the linear fit of the data for $t < t_{\text{Critical}}$. It is assumed that a change of microstructure represented by the change of the shape parameter k is the reason for the deviations. Additionally, it is assumed that due to the spatial extend of the beam profile the SRT is not found to be abrupt in the experimental data which makes it difficult to find the onset of the canting process (see section 5.3.4).

This has a strong influence on the determination of the magnetic anisotropies via scattering intensities and can thus be also a reason for the deviations above t_{Critical}.

5.5 Conclusion and Outlook

X-ray resonant magnetic scattering experiments on a wedge-shaped Co/Pd multilayer sample have been performed to study a locally varying disordered magnetic maze domain pattern. Radial scattering intensity profiles extracted from magnetic diffraction patterns reveal variations of the peak position, width, and intensity. A simple, one-dimensional model for the magnetization profile has been demonstrated to describe the observed radial distribution of the X-ray scattering intensity. It is found that a one-dimensional model using gamma-distributed domain sizes gives a very good agreement with the experimental findings. In the range of perpendicular magnetization the intensity profile of the maze pattern is best described by a fixed shape parameter $k = 4$, which implies a scale-invariance of the maze domain pattern in this range and hence an intrinsic symmetry, independent of the thickness or domain size variation. Introducing the new shape parameter into the domain model allows for the prediction and comparison of intrinsic symmetry properties of magnetic domain patterns. In addition, slight changes of the symmetry caused by external excitations, e.g., THz- or IR-radiation [73, 241, 242], can be mapped out with the model.

One important result is a discrepancy of 16% in the presented case when comparing the average domain size calculated from the peak value of the radial scattering intensity profile with the fitted domain size from the model. Further simulations have shown that the discrepancy increases with decreasing shape parameter and hence with increasing asymmetry of the domain size distribution. Therefore the commonly used method overestimates the average domain size of the real space domain pattern for the case of the disordered maze domain pattern. Above $k = 12$ the discrepancy vanishes and the gamma-distribution resembles a Gaussian distribution.

For larger thicknesses $t > t_{\text{Critical}}$ (supposed to be the transition to the canted phase) the shape parameter has to be changed from $k = 4$ to 3.3 to describe the scattering reasonably well. The different shape parameter hints to changes of the magnetic microstructure.

As a proof of principle, the obtained information from the scattering experiment, e.g., average domain size and scattering intensity, are used to determine thickness-dependent magnetic anisotropies of the Co/Pd multilayer wedge. The magnetic analysis proves the model to be correct in the range of perpendicular orientation of magnetization ($t < t_{\mathrm{Critical}}$). The magnetic properties (K_{1V}, K_{1S}) that come out of the analysis are in a good agreement with published results. However, for $t > t_{\mathrm{Critical}}$, the obtained anisotropy values do not smoothly match the anisotropies calculated below t_{Critical}. We obtain different slopes in the $K_{1,\mathrm{eff}} \cdot t_{\mathrm{Co,single}}$ vs. $t_{\mathrm{Co,single}}$ graph. Such a change of slope could be a growth-related property of the system [187, 230, 243]. However, the coincidence with the thickness where the model is changed rather hints at a problem of the description in the canting range or at the transition. It is assumed that the reason for the observed deviation is a change of the magnetic microstructure above t_{Critical}, indicated by a change of k within the model. In addition, experimental constraints, e.g., a limited beam size, can lead to a smeared out transition region between out-of-plane and canting in the experimental data, which make it difficult to determine the exact onset of the canting process. The anisotropies and canting angles are determined using the relative change of the integrated intensities in the canting region with respect to the onset, and thus depend strongly on its integrated intensity value. An imprecisely determined onset can thus also be a reason for the observed deviation.

In future projects the model in combination with the magnetic analysis can be applied to study the evolution of magnetic maze domain pattern in FEL-, infrared- or THz-pump and FEL-probe experiments. The impact of the excitations on the magnetic domain pattern can be analyzed with regard to geometry, domain wall or intensity changes. The additionally obtained information can lead to a better understanding of the response of the magnetic system and the correlation between real-space and reciprocal-space. Due to the high sensitivity and lateral resolution of the XRMS technique small variations of domain size can be resolved. Thus, the model allows for the determination of magnetic anisotropies in a thickness range of only a few Angstrom which is a big advantage in relation to laser-based methods such as magneto-optical Kerr effect (MOKE) or Kerr-microscopy.

BIBLIOGRAPHY

[1] J. Heremans, "Solid state magnetic field sensors and applications", *J. Phys. D: Appl. Phys.*, **26**, 1149 (1993)

[2] M. H. Kryder, "Magnetic thin films for data storage", *Thin Solid Films*, **216**, 174 (1992)

[3] D. A. Thompson and J. S. Best, "The future of magnetic data storage techology", *IBM J. Res. Develop.*, **44**, 311 (2000)

[4] O. Cugat, J. Delamare, and G. Reyne, "Magnetic micro-actuators and systems (MAGMAS)", *IEEE Trans. Magn.*, **39**, 3607 (2003)

[5] D. Niarchos, "Magnetic MEMS: Key issues and some applications", *Sensor Actuat. A-Phys.*, **109**, 166 (2003)

[6] B. D. Terris and T. Thomson, "Nanofabricated and self-assembled magnetic structures as data storage media", *J. Phys. D: Appl. Phys.*, **38**, R199 (2005)

[7] C. Chappert, A. Fert, and F. N. Van Dau, "The emergence of spin electronics in data storage", *Nat. Mater.*, **6**, 813 (2007)

[8] N. S. Kiselev, A. N. Bogdanov, R. Schäfer, and U. K. Rößler, "Chiral skyrmions in thin magnetic films: New objects for magnetic storage technologies?", *J. Phys. D: Appl. Phys.*, **44**, 392001 (2011)

[9] B. Miao, Y. Millev, L. Sun, B. You, W. Zhang, and H. Ding, "Thickness-driven spin reorientation transition in ultrathin films", *Sci. China - Phys. Mech. Astronomy*, **56**, 70 (2013)

[10] G. P. Zhang, T. Latta, Z. Babyak, Y. H. Bai, and T. F. George, "All-optical spin switching: A new frontier in femtomagnetism - A short review and a simple theory", *Mod. Phys. Lett. B*, **30**, 16300052 (2016)

[11] B. Vodungbo, B. Tudu, J. Perron, R. Delaunay, L. Müller, M. H. Berntsen, G. Grübel, G.and Malinowski, C. Weier, J. Gautier, G. Lambert, P. Zeitoun, C. Gutt, E. Jal, A. H. Reid, P. W. G., N. Jaouen, G. L. Dakovski, S. Moeller, M. P. Minitti, A. Mitra, S. Carron, B. Pfau, C. von Korff Schmising, M. Schneider, S. Eisebitt, and J. Lüning, "Indirect excitation of ultrafast demagnetization", *Sci. Rep.*, **6**, 18970 (2016)

[12] D. Sander, "The magnetic anisotropy and spin reorientation of nanostructures and nanoscale films", *J. Phys.: Condens. Matter*, **16**, R603 (2004)

[13] J. Teixeira, R. A. Silva, J. Ventura, A. Pereira, F. Carpinteiro, J. Araújo, J. Sousa, S. Cardoso, R. Ferreira, and P. Freitas, "Domain imaging, MOKE and magnetoresistance studies of CoFeB films for MRAM applications", *Mater. Sci. Eng. B*, **126**, 180 (2006)

[14] N. Biziere, C. Gatel, R. Lassalle-Balier, M. C. Clochard, J. E. Wegrowe, and E. Snoeck, "Imaging the Fine Structure of a Magnetic Domain Wall in a Ni Nanocylinder", *Nano Lett.*, **13**, 2053 (2013)

[15] R. Streubel, P. Fischer, F. Kronast, V. P. Kravchuk, D. D. Sheka, Y. Gaididei, O. G. Schmidt, and D. Makarov, "Magnetism in curved geometries", *J. Phys. D: Appl. Phys.*, **49**, 363001 (2016)

[16] I. Manke, N. Kardjilov, R. Schäfer, A. Hilger, M. Strobl, M. Dawson, C. Grünzweig, G. Behr, M. Hentschel, C. David, A. Kupsch, A. Lange, and J. Banhart, "Three-dimensional imaging of magnetic domains", *Nat. Commun.*, **1**, 125 (2010)

[17] J. McCord, "Progress in magnetic domain observation by advanced magneto-optical microscopy", *J. Phys. D: Appl. Phys.*, **48**, 333001 (2015)

[18] A. Hubert and R. Schäfer, *Magnetic Domains: The Analysis of Magnetic Microstructure*, (Springer-Verlag (2009), ISBN 978-3-540-85054-0)

[19] C.-G. Stefanita, *From Bulk to Nano: The Many Sides of Mangetism*, (Springer Series in Material Science (2008), ISBN 978-3-540-70548-2)

[20] W. Kuch, "Magnetic Imaging", in "Magnetism: A Synchrotron Radiation Approach", (Springer-Verlag (2006), ISBN: 978-3-540-33241-1)

[21] H. Hopster and H. P. Oepen, *Magnetic Microscopy of Nanostructures*, (Springer-Verlag (2005), ISBN: 978-3-540-40186-5)

[22] U. Hartmann, *Magnetic Multilayers and Giant Magnetoresistance: Fundamentals and Industrial Applications*, (Springer-Verlag, Springer Series in Surface Sciences (2010), ISBN: 978-3-662-04121-5)

[23] B. D. Terris, T. Thomson, and G. Hu, “Patterned media for future magnetic data storage”, *Microsyst. Technol.*, **13**, 189 (2007)

[24] H. Coufal and C. D. Dhar, L.and Mee, “Materials for Magnetic Data Storage: The Ongoing Quest for Superior Magnetic Materials”, *MRS Bulletin*, **31**, 374 (2006)

[25] S. N. Piramanayagam, “Perpendicular recording media for hard disk drives”, *J. Appl. Phys.*, **102**, 011301 (2007)

[26] M. H. Kryder and C. S. Kim, “After Hard Drives - What Comes Next?”, *IEEE Trans. Magn.*, **45**, 3406 (2009)

[27] R. H. Victora, S. M. Morgan, K. Momsen, E. Cho, and M. F. Erden, “Two-Dimensional Magnetic Recording at 10 Tbits/in2””, *IEEE Trans. Magn.*, **48**, 1697 (2012)

[28] D. Suess, T. Schrefl, R. Dittrich, M. Kirschner, F. Dorfbauer, G. Hrkac, and J. Fidler, “Exchange spring recording media for areal densities up to 10 Tbit/in2”, *J. Magn. Magn. Mater.*, **290**, 551 (2005)

[29] T. Li, A. Patz, L. Mouchliadis, J. Yan, T. A. Lograsso, I. E. Perakis, and J. Wang, “Femtosecond switching of magnetism via strongly correlated spin-charge quantum excitations”, *Nature*, **496**, 69 (2013)

[30] A. Kirilyuk, A. V. Kimel, and T. Rasing, “Ultrafast optical manipulation of magnetic order”, *Rev. Mod. Phys.*, **82**, 2731 (2010)

[31] P. C. D. Hobbs, D. W. Abraham, and H. K. Wickramasinghe, “”Magnetic force microscopy with 25 nm resolution””, *Appl. Phys. Lett.*, **55**, 2357 (1989)

[32] G. N. Phillips, M. Siekman, L. Abelmann, and J. C. Lodder, “High resolution magnetic force microscopy using focused ion beam modified tips”, *Appl. Phys. Lett.*, **81**, 865 (2002)

[33] M. Futamoto, T. Hagami, S. Ishihara, K. Soneta, and M. Ohtake, "Improvement of Magnetic Force Microscope Resolution and Application to High-Density Recording Media", *IEEE Trans. Magn.*, **49**, 2748 (2013)

[34] K. Nagano, K. Tobari, M. Ohtake, and M. Futamoto, "Effect of Magnetic Film Thickness on the Spatial Resolution of Magnetic Force Microscope Tips", *J. Phys. Conf. Ser.*, **303**, 012014 (2011)

[35] R. Wiesendanger, "Spin mapping at the nanoscale and atomic scale", *Rev. Mod. Phys.*, **81**, 1495 (2009)

[36] M. R. Scheinfein, J. Unguris, M. H. Kelley, D. T. Pierce, and R. J. Celotta, "Scanning electron microscopy with polarization analysis (SEMPA)", *Rev. Sci. Instrum.*, **61**, 2501 (1990)

[37] H. P. Oepen and R. Frömter, "Scanning Electron Microscopy with Polarisation Analysis", in "Handbook of Magnetism and Advanced Magnetic Materials", (John Wiley & Sons, Inc. (2007), ISBN: 978-0-470-02217-7)

[38] K. Koike, "Spin-polarized scanning electron microscopy", *Microscopy*, **62**, 177 (2013)

[39] R. Frömter, F. Kloodt, S. Rößler, A. Frauen, P. Staeck, D. R. Cavicchia, L. Bocklage, V. Röbisch, E. Quandt, and H. P. Oepen, "Time-resolved scanning electron microscopy with polarization analysis", *Appl. Phys. Lett.*, **108**, 142401 (2016)

[40] A. Petford-Long and J. Chapman, "Lorentz Microscopy", in H. Hopster and H. P. Oepen (Editors), "Magnetic Microscopy of Nanostructures", (Springer-Verlag (2005), ISBN: 978-3-540-40186-5)

[41] C. Phatak, A. Petford-Long, and M. De Graef, "Recent advances in Lorentz microscopy", *Curr. Opin. Solid. St. M.*, **20**, 107 (2016)

[42] S. McVitie, D. McGrouther, S. McFadzean, D. MacLaren, K. O'Shea, and M. Benitez, "Aberration corrected Lorentz scanning transmission electron microscopy", *Ultramicroscopy*, **152**, 57 (2015)

[43] H. S. Park, J. S. Baskin, and A. H. Zewail, "4D Lorentz Electron Microscopy Imaging: Magnetic Domain Wall Nucleation, Reversal, and Wave Velocity", *Nano Lett.*, **10**, 3796 (2010)

[44] J. McCord and A. Hubert, "Normalized Differential Kerr Microscopy An Advanced Method for Magnetic Imaging", *Phys. Status Solidi A*, **171**, 555 (1999)

[45] A. Laraoui, M. Albrecht, and J.-Y. Bigot, "Femtosecond magneto-optical Kerr microscopy", *Opt. Lett.*, **32**, 936 (2007)

[46] F. de Bergevin and M. Brunel, "Diffraction of X-rays by magnetic materials. I. General formulae and measurements on ferro- and ferrimagnetic compounds", *Acta Crystallogr. A*, **37**, 314 (1981)

[47] D. Attwood, *Soft X-rays and Extreme Ultraviolet Radiation*, (Cambridge University Press (1999), ISBN: 978-0-521-02997-1)

[48] P. Fischer, G. Denbeaux, T. Ono, T. Okuno, T. Eimüller, D. Goll, and G. Schütz, "Study of magnetic domains by magnetic soft x-ray transmission microscopy", *J. Phys. D: Appl. Phys.*, **35**, 2391 (2002)

[49] P. Fischer, "X-Ray Imaging of Magnetic Structures", *IEEE Trans. Magn.*, **51**, 1 (2015)

[50] P. Fischer, G. Schutz, G. Schmahl, P. Guttmann, and D. Raasch, "Imaging of magnetic domains with the X-ray microscope at BESSY using X-ray magnetic circular dichroism", *Z. Phys. B*, **101**, 313 (1996)

[51] M. J. Robertson, C. J. Agostino, A. T. N'Diaye, G. Chen, M.-Y. Im, and P. Fischer, "Quantitative x-ray magnetic circular dichroism mapping with high spatial resolution full-field magnetic transmission soft x-ray spectro-microscopy", *J. Appl. Phys.*, **117**, 17D145 (2015)

[52] A. L. D. Kilcoyne, T. Tyliszczak, W. F. Steele, S. Fakra, P. Hitchcock, K. Franck, E. Anderson, B. Harteneck, E. G. Rightor, G. E. Mitchell, A. P. Hitchcock, L. Yang, T. Warwick, and H. Ade, "Interferometer-controlled scanning transmission X-ray microscopes at the Advanced Light Source", *J. Synchrotron Radiat.*, **10**, 125 (2003)

[53] J. Raabe, G. Tzvetkov, U. Flechsig, M. Böge, A. Jaggi, B. Sarafimov, M. G. C. Vernooij, T. Huthwelker, H. Ade, D. Kilcoyne, T. Tyliszczak, R. H. Fink, and C. Quitmann, "PolLux: A new facility for soft x-ray spectromicroscopy at the Swiss Light Source", *Rev. Sci. Instrum.*, **79**, 113704 (2008)

[54] P. Fischer, T. Eimüller, G. Schütz, G. Denbeaux, A. Pearson, L. Johnson, D. Attwood, S. Tsunashima, M. Kumazawa, N. Takagi, M. Köhler, and G. Bayreuther, "Element-specific imaging of magnetic domains at 25 nm spatial resolution using soft x-ray microscopy", *Rev. Sci. Instrum.*, **72**, 2322 (2001)

[55] W. Chao, B. D. Harteneck, J. A. Liddle, E. H. Anderson, and D. T. Attwood, "Soft X-ray microscopy at a spatial resolution better than 15 nm", *Nature*, **435**, 1210 (2005)

[56] D.-H. Kim, P. Fischer, W. Chao, E. Anderson, M.-Y. Im, S.-C. Shin, and S.-B. Choe, "Magnetic soft x-ray microscopy at 15 nm resolution probing nanoscale local magnetic hysteresis (invited)", *J. Appl. Phys.*, **99**, 08H303 (2006)

[57] S. Kasai, P. Fischer, M.-Y. Im, K. Yamada, Y. Nakatani, K. Kobayashi, H. Kohno, and T. Ono, "Probing the Spin Polarization of Current by Soft X-Ray Imaging of Current-Induced Magnetic Vortex Dynamics", *Phys. Rev. Lett.*, **101**, 237203 (2008)

[58] M. Bolte, G. Meier, B. Krüger, R. Drews, A.and Eiselt, L. Bocklage, S. Bohlens, T. Tyliszczak, A. Vansteenkiste, B. Van Waeyenberge, K. W. Chou, A. Puzic, and H. Stoll, "Time-Resolved X-Ray Microscopy of Spin-Torque-Induced Magnetic Vortex Gyration", *Phys. Rev. Lett.*, **100**, 176601 (2008)

[59] J. Feng and A. Scholl, "Photoemission Electron Microscopy (PEEM)", in "Science of Microscopy", (Springer-Verlag (2007), ISBN: 978-0-387-25296-4)

[60] T. Kinoshita, K. Arai, K. Fukumoto, T. Ohkochi, M. Kotsugi, F. Guo, T. Muro, T. Nakamura, H. Osawa, T. Matsushita, and T. Okuda, "Observation of Micro-Magnetic Structures by Synchrotron Radiation Photoelectron Emission Microscopy", *J. Phys. Soc. Jpn.*, **82**, 021005 (2012)

[61] C. M. Schneider, A. Krasyuk, S. A. Nepijko, A. Oelsner, and G. Schönhense, "Accessing fast magnetization dynamics by XPEEM: Status and perspectives", *J. Magn. Magn. Mater.*, **304**, 6 (2006)

[62] J. P. Hannon, G. T. Trammell, M. Blume, and D. Gibbs, "X-Ray Resonance Exchange Scattering", *Phys. Rev. Lett.*, **61**, 1245 (1988)

[63] K. Chesnel, M. Belakhovsky, S. Landis, J. C. Toussaint, S. P. Collins, G. van der Laan, E. Dudzik, and S. S. Dhesi, "X-ray resonant magnetic scattering study

of the magnetic coupling in Co/Pt nanolines and its evolution under magnetic field", *Phys. Rev. B*, **66**, 024435 (2002)

[64] O. Hellwig, G. Denbeaux, J. Kortright, and E. E. Fullerton, "X-ray studies of aligned magnetic stripe domains in perpendicular multilayers", *Physica B*, **336**, 136 (2003)

[65] J. B. Kortright, "Resonant soft X-ray and extreme ultraviolet magnetic scattering in nanostructured magnetic materials: Fundamentals and directions", *J. Electron Spectrosc.*, **189**, 178 (2013)

[66] S. Eisebitt, J. Lüning, W. F. Schlotter, M. Lörgen, O. Hellwig, W. Eberhardt, and J. Stöhr, "Lensless imaging of magnetic nanostructures by X-ray spectro-holography", *Nature*, **432**, 885 (2004)

[67] S. Schaffert, B. Pfau, J. Geilhufe, C. M. Günther, M. Schneider, C. von Korff Schmising, and S. Eisebitt, "High-resolution magnetic-domain imaging by Fourier transform holography at 21 nm wavelength", *New J. Phys.*, **15**, 093042 (2013)

[68] S. Streit-Nierobisch, D. Stickler, C. Gutt, L.-M. Stadler, H. Stillrich, C. Menk, R. Frömter, C. Tieg, O. Leupold, H. P. Oepen, and G. Grübel, "Magnetic soft x-ray holography study of focused ion beam-patterned Co/Pt multilayers", *J. Appl. Phys.*, **106**, 083909 (2009)

[69] D. Stickler, R. Frömter, H. Stillrich, C. Menk, C. Tieg, S. Streit-Nierobisch, M. Sprung, C. Gutt, L.-M. Stadler, O. Leupold, G. Grübel, and H. P. Oepen, "Soft x-ray holographic microscopy", *Appl. Phys. Lett.*, **96**, 042501 (2010)

[70] T. Wang, D. Zhu, B. Wu, C. Graves, S. Schaffert, T. Rander, L. Müller, B. Vodungbo, C. Baumier, D. P. Bernstein, B. Bräuer, V. Cros, S. de Jong, R. Delaunay, A. Fognini, R. Kukreja, S. Lee, V. López-Flores, J. Mohanty, B. Pfau, H. Popescu, M. Sacchi, A. B. Sardinha, F. Sirotti, P. Zeitoun, M. Messerschmidt, J. J. Turner, W. F. Schlotter, O. Hellwig, R. Mattana, N. Jaouen, F. Fortuna, Y. Acremann, C. Gutt, H. A. Dürr, E. Beaurepaire, C. Boeglin, S. Eisebitt, G. Grübel, J. Lüning, J. Stöhr, and A. O. Scherz, "Femtosecond Single-Shot Imaging of Nanoscale Ferromagnetic Order in Co/Pd Multilayers Using Resonant X-Ray Holography", *Phys. Rev. Lett.*, **108**, 267403 (2012)

[71] C. von Korff Schmising, B. Pfau, M. Schneider, C.-M. Günther, M. Giovannella, J. Perron, B. Vodungbo, L. Müller, F. Capotondi, E. Pedersoli, N. Mahne, J. Lüning, and S. Eisebitt, "Imaging Ultrafast Demagnetization Dynamics after a Spatially Localized Optical Excitation", *Phys. Rev. Lett.*, **112**, 217203 (2014)

[72] C. Gutt, S. Streit-Nierobisch, L.-M. Stadler, B. Pfau, C. M. Günther, R. Könnecke, R. Frömter, A. Kobs, D. Stickler, H. P. Oepen, R. R. Fäustlin, R. Treusch, J. Feldhaus, E. Weckert, I. A. Vartanyants, M. Grunze, A. Rosenhahn, T. Wilhein, S. Eisebitt, and G. Grübel, "Single-pulse resonant magnetic scattering using a soft x-ray free-electron laser", *Phys. Rev. B*, **81**, 100401 (2010)

[73] B. Pfau, S. Schaffert, L. Müller, C. Gutt, A. Al-Shemmary, F. Büttner, R. Delaunay, S. Düsterer, S. Flewett, R. Frömter, J. Geilhufe, E. Guehrs, C. Günther, R. Hawaldar, M. Hille, N. Jaouen, A. Kobs, K. Li, J. Mohanty, H. Redlin, W. Schlotter, D. Stickler, R. Treusch, B. Vodungbo, M. Kläui, H. Oepen, J. Lüning, G. Grübel, and S. Eisebitt, "Ultrafast optical demagnetization manipulates nanoscale spin structure in domain walls", *Nat. Commun.*, **3**, 1100 (2012)

[74] L. Müller, C. Gutt, B. Pfau, S. Schaffert, J. Geilhufe, F. Büttner, J. Mohanty, S. Flewett, R. Treusch, S. Düsterer, H. Redlin, A. Al-Shemmary, M. Hille, A. Kobs, R. Frömter, H. P. Oepen, B. Ziaja, N. Medvedev, S.-K. Son, R. Thiele, R. Santra, B. Vodungbo, J. Lüning, S. Eisebitt, and G. Grübel, "Breakdown of the X-Ray Resonant Magnetic Scattering Signal during Intense Pulses of Extreme Ultraviolet Free-Electron-Laser Radiation", *Phys. Rev. Lett.*, **110**, 234801 (2013)

[75] E. Beaurepaire, J.-C. Merle, A. Daunois, and J.-Y. Bigot, "Ultrafast Spin Dynamics in Ferromagnetic Nickel", *Phys. Rev. Lett.*, **76**, 4250 (1996)

[76] B. Koopmans, G. Malinowski, F. Dalla Longa, D. Steiauf, M. Fahnle, T. Roth, M. Cinchetti, and M. Aeschlimann, "Explaining the paradoxical diversity of ultrafast laser-induced demagnetization", *Nat. Mater.*, **9**, 259 (2010)

[77] M. Battiato, K. Carva, and P. M. Oppeneer, "Superdiffusive Spin Transport as a Mechanism of Ultrafast Demagnetization", *Phys. Rev. Lett.*, **105**, 027203 (2010)

[78] A. Eschenlohr, M. Battiato, P. Maldonado, N. Pontius, T. Kachel, K. Holldack, R. Mitzner, A. Föhlisch, P. M. Oppeneer, and C. Stamm, "Ultrafast spin transport as key to femtosecond demagnetization", *Nat. Mater.*, **12**, 332 (2013)

[79] P. Skopintsev, A. Singer, J. Bach, L. Müller, B. Beyersdorff, S. Schleitzer, O. Gorobtsov, A. Shabalin, R. P. Kurta, D. Dzhigaev, O. M. Yefanov, L. Glaser, A. Sakdinawat, G. Grübel, R. Frömter, H. P. Oepen, J. Viefhaus, and I. A. Vartanyants, "Characterization of spatial coherence of synchrotron radiation with non-redundant arrays of apertures", *J. Synchrotron Radiat.*, **21**, 722 (2014)

[80] C. Chang, P. Naulleau, E. Anderson, and D. Attwood, "Spatial coherence characterization of undulator radiation", *Opt. Commun.*, **182**, 25 (2000)

[81] A. Singer, F. Sorgenfrei, A. P. Mancuso, N. Gerasimova, O. M. Yefanov, J. Gulden, T. Gorniak, T. Senkbeil, A. Sakdinawat, Y. Liu, D. Attwood, S. Dziarzhytski, D. D. Mai, R. Treusch, E. Weckert, T. Salditt, A. Rosenhahn, W. Wurth, and I. A. Vartanyants, "Spatial and temporal coherence properties of single free-electron laser pulses", *Opt. Express*, **20**, 17480 (2012)

[82] M. Rose, P. Skopintsev, D. Dzhigaev, O. Gorobtsov, T. Senkbeil, A. von Gundlach, T. Gorniak, A. Shabalin, J. Viefhaus, A. Rosenhahn, and I. Vartanyants, "Water window ptychographic imaging with characterized coherent X-rays", *J. Synchrotron Radiat.*, **22**, 819 (2015)

[83] R. Rick, A. Scherz, W. F. Schlotter, D. Zhu, J. Lüning, and J. Stöhr, "Optimal signal-to-noise ratios for soft x-ray lensless imaging", *Opt. Lett.*, **34**, 650 (2009)

[84] K. A. Nugent and J. E. Trebes, "Coherence measurement technique for short-wavelength light sources", *Rev. Sci. Instrum.*, **63**, 2146 (1992)

[85] J. J. A. Lin, D. Paterson, A. G. Peele, P. J. McMahon, C. T. Chantler, K. A. Nugent, B. Lai, N. Moldovan, Z. Cai, D. C. Mancini, and I. McNulty, "Measurement of the Spatial Coherence Function of Undulator Radiation using a Phase Mask", *Phys. Rev. Lett.*, **90**, 074801 (2003)

[86] D. L. Abernathy, G. Grübel, S. Brauer, I. McNulty, G. B. Stephenson, S. G. J. Mochrie, A. R. Sandy, N. Mulders, and M. Sutton, "Small-Angle X-ray Scattering Using Coherent Undulator Radiation at the ESRF", *J. Synchrotron Radiat.*, **5**, 37 (1998)

[87] A. R. Sandy, L. B. Lurio, S. G. J. Mochrie, A. Malik, G. B. Stephenson, J. F. Pelletier, and M. Sutton, "Design and characterization of an undulator beamline optimized for small-angle coherent X-ray scattering at the Advanced Photon Source", *J. Synchrotron Radiat.*, **6**, 1174 (1999)

[88] F. Lehmkühler, C. Gutt, B. Fischer, M. A. Schroer, M. Sikorski, S. Song, W. Roseker, J. Glownia, M. Chollet, S. Nelson, K. Tono, T. Katayama, M. Yabashi, T. Ishikawa, A. Robert, and G. Grübel, "Single Shot Coherence Properties of the Free-Electron Laser SACLA in the Hard X-ray Regime", *Sci. Rep.*, **4**, 5234 (2014)

[89] C. Gutt, P. Wochner, B. Fischer, H. Conrad, M. Castro-Colin, S. Lee, F. Lehmkühler, I. Steinke, M. Sprung, W. Roseker, D. Zhu, H. Lemke, S. Bogle, P. H. Fuoss, G. B. Stephenson, M. Cammarata, D. M. Fritz, A. Robert, and G. Grübel, "Single Shot Spatial and Temporal Coherence Properties of the SLAC Linac Coherent Light Source in the Hard X-Ray Regime", *Phys. Rev. Lett.*, **108**, 024801 (2012)

[90] K. A. Nugent, "Coherent methods in the X-ray sciences", *Adv. Phys.*, **59**, 1 (2010)

[91] J. W. Goodman, *Speckle Phenomena in Optics: Theory and Applications*, (Roberts & Company (2007), ISBN: 978-1-936-22114-1)

[92] L. Mandel and E. Wolf, *Optical Coherence and Quantum Optics*, (Cambridge University Press (1995), ISBN: 978-0-521-41711-2)

[93] A. Singer, *Coherence properties of third and fourth generation x-ray sources. Theory and experiment*, Ph.D. thesis, Universität Hamburg (2012)

[94] A. T. Friberg and R. J. Sudol, "The Spatial Coherence Properties of Gaussian Schell-model Beams", *Opt. Acta*, **30**, 1075 (1983)

[95] T. Young, "The Bakerian Lecture: On the Theory of Light and Colours", *Phil. Trans. R. Soc. Lond.*, **92**, 12 (1802)

[96] P. H. van Cittert, "Die Wahrscheinliche Schwingungsverteilung in Einer von Einer Lichtquelle Direkt Oder Mittels Einer Linse Beleuchteten Ebene", *Physica*, **1**, 201 (1934)

[97] F. Zernike, "The concept of degree of coherence and its application to optical problems", *Physica*, **5**, 785 (1938)

[98] G. Geloni, E. Saldin, E. Schneidmiller, and M. Yurkov, "Transverse coherence properties of X-ray beams in third-generation synchrotron radiation sources", *Nucl. Instrum. Meth. A*, **588**, 463 (2008)

[99] J. Goodman, *Statistical Optics*, (John Wiley & Sons, Inc. (2000), ISBN: 978-0-471-39916-2)

[100] I. A. Vartanyants and A. Singer, "Coherence properties of hard x-ray synchrotron sources and x-ray free-electron lasers", *New J. Phys.*, **12**, 035004 (2010)

[101] R. Coïsson, "Spatial coherence of synchrotron radiation", *Appl. Opt.*, **34**, 904 (1995)

[102] R. Coïsson and S. Marchesini, "Gauss-schell sources as models for synchrotron radiation", *J. Synchrotron Radiat.*, **4**, 263 (1997)

[103] M. R. Howels and B. M. Kincaid, "The properties of undulator radiation", in "New Directions in Research with Third-Generation Soft X-Ray Synchrotron Radiation Sources", (Kluver Academic Publishers (1994), ISBN: 978-94-010-4375-5)

[104] Y. Takayama, N. Takaya, T. Miyahara, S. Kamada, W. Okamoto, T. Hatano, R. Tai, and Y. Kagoshima, "Spatial coherence of undulator radiation beyond the van Cittert-Zernike theorem", *Nucl. Instrum. Meth. A*, **441**, 565 (2000)

[105] Z. Zhang, *Analysis and synthesis of three-dimensional illumination using partial coherence*, Ph.D. thesis, Stanford University (2011)

[106] F. Gori, M. Santarsiero, G. Piquero, R. Borghi, A. Mondello, and R. Simon, "Partially polarized Gaussian Schell-model beams", *J. Opt. A: Pure Appl. Opt.*, **3**, 1 (2001)

[107] S. Ocko, "A Study of the Transverse Coherence Properties of the LCLS", (2009, http://www.slac.stanford.edu/cgi-wrap/getdoc/slac-tn-10-013.pdf)

[108] D. Pelliccia, A. Y. Nikulin, H. O. Moser, and K. A. Nugent, "Experimental characterization of the coherence properties of hard x-ray sources", *Opt. Express*, **19**, 8073 (2011)

[109] A. Schell, "A technique for the determination of the radiation pattern of a partially coherent aperture", *IEEE Trans. Antenn. Propag.*, **15**, 187 (1967)

[110] A. T. Friberg and R. J. Sudol, "Propagation parameters of gaussian Schell-model beams", *Opt. Commun.*, **41**, 383 (1982)

[111] W. Demtröder, "Optics of Gaussian Beams", in "Laser Spectroscopy 1: Basic Principles", (Springer-Verlag (2014), ISBN 978-3-540-73418-5)

[112] J. Viefhaus, F. Scholz, S. Deinert, L. Glaser, M. Ilchen, J. Seltmann, P. Walter, and F. Siewert, "The Variable Polarization XUV Beamline P04 at PETRA III: Optics, mechanics and their performance", *Nucl. Instrum. Meth. A*, **710**, 151 (2013)

[113] D. Attwood, K. Halbach, and K. Kim, "Tunable Coherent X-rays", *Science*, **228**, 1265 (1985)

[114] A. Singer and I. A. Vartanyants, "Coherence properties of focused X-ray beams at high-brilliance synchrotron sources", *J. Synchrotron Radiat.*, **21**, 5 (2014)

[115] X. Meng, C. Xue, H. Yu, Y. Wang, Y. Wu, and R. Tai, "Numerical analysis of partially coherent radiation at soft x-ray beamline", *Opt. Express*, **23**, 29675 (2015)

[116] R. L. Johnson, "Grazing-incidence monochromators for synchrotron radiation - A review", *Nucl. Instrum. Meth. A*, **246**, 303 (1986)

[117] M. Itou, T. Harada, and T. Kita, "Soft x-ray monochromator with a varied-space plane grating for synchrotron radiation: Design and evaluation", *Appl. Opt.*, **28**, 146 (1989)

[118] C. Y. Li, J. F. Zhu, and Q. P. Wang, "Design of a Varied-line-spacing plane grating monochromator at NSRL for surface physics experiments", *J. Phys. Conf. Ser.*, **425**, 162008 (2013)

[119] M. Fujisawa, A. Harasawa, A. Agui, M. Watanabe, A. Kakizaki, S. Shin, T. Ishii, T. Kita, T. Harada, Y. Saitoh, and S. Suga, "Varied line-spacing plane grating monochromator for undulator beamline", *Rev. Sci. Instrum.*, **67**, 345 (1996)

[120] D. Paterson, B. E. Allman, P. J. McMahon, J. Lin, N. Moldovan, K. A. Nugent, I. McNulty, C. T. Chantler, C. C. Retsch, T. H. K. Irving, and D. C. Mancini,

"Spatial coherence measurement of X-ray undulator radiation", *Opt. Commun.*, **195**, 79 (2001)

[121] J. Turunen and A. T. Friberg, "Matrix representation of Gaussian Schell-model beams in optical systems", *Opt. Laser Technol.*, **18**, 259 (1986)

[122] H. T. Yura and S. G. Hanson, "Optical beam wave propagation through complex optical systems", *J. Opt. Soc. Am. A*, **4**, 1931 (1987)

[123] J. Stöhr and H. C. Siegmann, *Magnetism: From Fundamentals to Nanoscale Dynamics*, (Springer-Verlag (2006), ISBN: 978-3-540-30283-4)

[124] R. Nakajima, J. Stöhr, and Y. U. Idzerda, "Electron-yield saturation effects in L-edge x-ray magnetic circular dichroism spectra of Fe, Co, and Ni", *Phys. Rev. B*, **59**, 6421 (1999)

[125] A. Scherz, W. F. Schlotter, K. Chen, R. Rick, J. Stöhr, J. Lüning, I. McNulty, C. Günther, F. Radu, W. Eberhardt, O. Hellwig, and S. Eisebitt, "Phase imaging of magnetic nanostructures using resonant soft x-ray holography", *Phys. Rev. B*, **76**, 214410 (2007)

[126] J. L. Erskine and E. A. Stern, "Calculation of the M23 magneto-optical absorption spectrum of ferromagnetic nickel", *Phys. Rev. B*, **12**, 5016 (1975)

[127] G. Schütz, W. Wagner, W. Wilhelm, P. Kienle, R. Zeller, R. Frahm, and G. Materlik, "Absorption of circularly polarized x rays in iron", *Phys. Rev. Lett.*, **58**, 737 (1987)

[128] M. Faraday, "Experimental Researches in Electricity. Nineteenth Series", *Phil. Trans. R. Soc. Lond.*, **136**, 1 (1846)

[129] J. Kerr, "XLIII. On rotation of the plane of polarization by reflection from the pole of a magnet", *Phil. Mag. S. 5*, **3**, 321 (1877)

[130] J. Stöhr, "Exploring the microscopic origin of magnetic anisotropies with X-ray magnetic circular dichroism (XMCD) spectroscopy", *J. Magn. Magn. Mater.*, **200**, 470 (1999)

[131] E. C. Stoner, "Collective Electron Ferromagnetism. II. Energy and Specific Heat", *P. Roy. Soc. Lond. A Mat.*, **169**, 339 (1939)

[132] R. Nakajima, *X-ray magnetic circular dichroism: Spectroscopy in transition metal thin films*, Ph.D. thesis, Stanford University (1998)

[133] S. Valencia, A. Gaupp, W. Gudat, H.-C. Mertins, P. M. Oppeneer, D. Abramsohn, and C. M. Schneider, "Faraday rotation spectra at shallow core levels: 3p edges of Fe, Co, and Ni", *New J. Phys.*, **8**, 254 (2006)

[134] M. Lörgen, *Coherent Soft X-Ray Magnetic Scattering and Lensless Imaging*, Ph.D. thesis, Technische Universität Berlin (2004)

[135] B. Henke, E. Gullikson, and J. Davis, "X-Ray Interactions: Photoabsorption, Scattering, Transmission, and Reflection at E = 50-30,000 eV, Z = 1-92", *Atomic Data and Nuclear Data Tables*, **54**, 181 (1993)

[136] S. Lovesey and S. Collins, *X-Ray Scattering and Absorption by Magnetic Materials*, (Oxford University Press Inc., (1996), ISBN: 978-0198517375)

[137] J. B. Kortright, S.-K. Kim, G. P. Denbeaux, G. Zeltzer, K. Takano, and E. E. Fullerton, "Soft-x-ray small-angle scattering as a sensitive probe of magnetic and charge heterogeneity", *Phys. Rev. B*, **64**, 092401 (2001)

[138] G. van der Laan, B. T. Thole, G. A. Sawatzky, J. B. Goedkoop, J. C. Fuggle, J.-M. Esteva, R. Karnatak, J. P. Remeika, and H. A. Dabkowska, "Experimental proof of magnetic x-ray dichroism", *Phys. Rev. B*, **34**, 6529 (1986)

[139] E. Arenholz, G. van der Laan, R. V. Chopdekar, and Y. Suzuki, "Anisotropic x-ray magnetic linear dichroism at the Fe L2,3 edges in Fe3O4", *Phys. Rev. B*, **74**, 094407 (2006)

[140] J. Kunez and P. M. Oppeneer, "Anisotropic x-ray magnetic linear dichroism at the L2,3 edges of cubic Fe, Co, and Ni: *Ab initio* calculations and model theory", *Phys. Rev. B*, **67**, 024431 (2003)

[141] H.-C. Mertins, S. Valencia, A. Gaupp, W. Gudat, P. Oppeneer, and C. Schneider, "Magneto-optical polarization spectroscopy with soft X-rays", *Appl. Phys. A-Mater.*, **80**, 1011 (2005)

[142] C. Gutt, L.-M. Stadler, S. Streit-Nierobisch, A. P. Mancuso, A. Schropp, B. Pfau, C. M. Günther, R. Könnecke, J. Gulden, B. Reime, J. Feldhaus, E. Weckert, I. A. Vartanyants, O. Hellwig, F. Staier, R. Barth, M. Grunze, A. Rosenhahn,

D. Stickler, H. Stillrich, R. Frömter, H. P. Oepen, M. Martins, T. Nisius, T. Wilhein, B. Faatz, N. Guerassimova, K. Honkavaara, V. Kocharyan, R. Treusch, E. Saldin, S. Schreiber, E. A. Schneidmiller, M. V. Yurkov, S. Eisebitt, and G. Grübel, "Resonant magnetic scattering with soft x-ray pulses from a free-electron laser operating at 1.59 nm", *Phys. Rev. B*, **79**, 212406 (2009)

[143] G. Winkler, A. Kobs, A. Chuvilin, D. Lott, A. Schreyer, and H. P. Oepen, "On the variation of magnetic anisotropy in Co/Pt(111) on silicon oxide", *J. Appl. Phys.*, **117**, 105306 (2015)

[144] A. Kobs, *Magnetogalvanic effects in ferromagnets of reduced dimensions*, Ph.D. thesis, Universität Hamburg (2013)

[145] O. Hellwig, A. Berger, J. B. Kortright, and E. E. Fullerton, "Domain structure and magnetization reversal of antiferromagnetically coupled perpendicular anisotropy films", *J. Magn. Magn. Mater.*, **319**, 13 (2007)

[146] T. Egami and S. Billinge, *Underneath the Bragg Peaks: Structural Analysis of Complex Materials*, (Pergamon Materials Series (2012), ISBN: 978-0-080-97133-9)

[147] B. E. Warren, *X-ray Diffraction*, (Dover Books on Physics (1991), ISBN: 978-0-486-66317-3)

[148] T. O. Mentes, C. Sanchez-Hanke, and C. C. Kao, "Reconstruction of magnetization density in two-dimensional samples from soft X-ray speckle patterns using the multiple-wavelength anomalous diffraction method", *J. Synchrotron Radiat.*, **9**, 90 (2002)

[149] T. Asakura, H. Fujii, and K. Murata, "Measurement of Spatial Coherence Using Speckle Patterns", *Opt. Acta*, **19**, 273 (1972)

[150] R. Erf, *Speckle Metrology*, (Academic Press, Inc. (1978), ISBN: 0-12-241360-1)

[151] A. Patterson, "A Direct Method for the Determination of the Components of Interatomic Distances in Crystals", *Z. Kristallogr.*, **90**, 517 (1935)

[152] J. C. Dainty, "The statistics of speckle pattern", in "Progress in Optics", (Elsevier (1977), ISBN: 978-0-444-10914-9)

[153] M. Sikorski, S. Song, A. Schropp, F. Seiboth, Y. Feng, R. Alonso-Mori, M. Chollet, H. T. Lemke, D. Sokaras, T.-C. Weng, W. Zhang, A. Robert, and D. Zhu, “Focus characterization at an X-ray free-electron laser by coherent scattering and speckle analysis”, *J. Synchrotron Radiat.*, **22**, 599 (2015)

[154] H. Fujii and T. Asakura, “A contrast variation of image speckle intensity under illumination of partially coherent light”, *Opt. Commun.*, **12**, 32 (1974)

[155] H. Fujii and T. Asakura, “Effect of surface roughness on the statistical distribution of image speckle intensity”, *Opt. Commun.*, **11**, 35 (1974)

[156] S. O. Hruszkewycz, M. Sutton, P. H. Fuoss, B. Adams, S. Rosenkranz, K. F. Ludwig, W. Roseker, D. Fritz, M. Cammarata, D. Zhu, S. Lee, H. Lemke, C. Gutt, A. Robert, G. Grübel, and G. B. Stephenson, “High Contrast X-ray Speckle from Atomic-Scale Order in Liquids and Glasses”, *Phys. Rev. Lett.*, **109**, 185502 (2012)

[157] S. Lee, W. Roseker, C. Gutt, B. Fischer, H. Conrad, F. Lehmkühler, I. Steinke, D. Zhu, H. Lemke, M. Cammarata, D. Fritz, P. Wochner, M. Castro-Colin, S. O. Hruszkewycz, P. H. Fuoss, G. B. Stephenson, G. Grübel, and A. Robert, “Single shot speckle and coherence analysis of the hard X-ray free electron laser LCLS”, *Opt. Express*, **21**, 24647 (2013)

[158] E. Dufresne, *Intensity fluctuation spectroscopy with coherent X-rays*, Ph.D. thesis, Centre for the Physics of Materials Canada (1995)

[159] M. Gilbert, H.-C. Mertins, M. Tesch, O. Berges, H. Feilbach, and C. M. Schneider, “TetraMag: A compact magnetizing device based on eight rotating permanent magnets”, *Rev. Sci. Instrum.*, **83**, 025109 (2012)

[160] D. Nolle, M. Weigand, P. Audehm, E. Goering, U. Wiesemann, C. Wolter, E. Nolle, and G. Schütz, “Note: Unique characterization possibilities in the ultra high vacuum scanning transmission x-ray microscope (UHV-STXM) MAXIMUS using a rotatable permanent magnetic field up to 0.22 T”, *Rev. Sci. Instrum.*, **83**, 046112 (2012)

[161] C. Weier, *Resonant Magnetic Scattering Studies using Synchrotron Radiation and Laser-Generated Extreme Ultraviolet Light*, Ph.D. thesis, Forschungszentrum Jülich, Peter Grünberg Institut (2015)

[162] T. Itoh, *Ion beam assisted film growth*, (Elsevier (1989), ISBN: 0-444-87280-9)

[163] J. A. Thornton, "Magnetron sputtering: Basic physics and application to cylindrical magnetrons", *J. Vac. Sci. Technol.*, **15**, 171 (1978)

[164] H. Stillrich, *Magnetische Nanostrukturen basierend auf Co/Pt-Multilagen hergestellt mittels selbstorganisierter Masken aus Blockcopolymer-Micellen*, Ph.D. thesis, Universität Hamburg (2008)

[165] G. Winkler, *Korrelation zwischen strukturellen und magnetogalvaniscehn Eigenschaften von Pt/Co/Pt- und Pd/Co/Pd-Schichtsystemen*, Ph.D. thesis, Universität Hamburg (2015)

[166] H. Stillrich, C. Menk, and H. P. Frömter, R.and Oepen, "Magnetic anisotropy and spin reorientation in Co/Pt multilayers: Influence of preparation", *J. Magn. Magn. Mater.*, **322**, 1353 (2010)

[167] H. N. Chapman, A. Barty, M. J. Bogan, S. Boutet, M. Frank, S. P. Hau-Riege, S. Marchesini, B. W. Woods, S. Bajt, W. H. Benner, R. A. London, E. Plonjes, M. Kuhlmann, R. Treusch, S. Dusterer, T. Tschentscher, J. R. Schneider, E. Spiller, T. Moller, C. Bostedt, M. Hoener, D. A. Shapiro, K. O. Hodgson, D. van der Spoel, F. Burmeister, M. Bergh, C. Caleman, G. Huldt, M. M. Seibert, F. R. N. C. Maia, R. W. Lee, A. Szoke, N. Timneanu, and J. Hajdu, "Femtosecond diffractive imaging with a soft-X-ray free-electron laser", *Nat. Phys.*, **2**, 839 (2006)

[168] M. M. Seibert, T. Ekeberg, F. R. N. C. Maia, M. Svenda, J. Andreasson, D. Jonsson, O.and Odic, B. Iwan, A. Rocker, D. Westphal, M. Hantke, D. P. DePonte, A. Barty, J. Schulz, L. Gumprecht, N. Coppola, A. Aquila, M. Liang, T. A. White, A. Martin, C. Caleman, S. Stern, C. Abergel, V. Seltzer, J.-M. Claverie, C. Bostedt, J. D. Bozek, S. Boutet, A. A. Miahnahri, M. Messerschmidt, J. Krzywinski, G. Williams, K. O. Hodgson, M. J. Bogan, C. Y. Hampton, R. G. Sierra, D. Starodub, I. Andersson, S. Bajt, M. Barthelmess, J. C. H. Spence, P. Fromme, U. Weierstall, R. Kirian, M. Hunter, R. B. Doak, S. Marchesini, S. P. Hau-Riege, M. Frank, R. L. Shoeman, L. Lomb, S. W. Epp, R. Hartmann, D. Rolles, A. Rudenko, C. Schmidt, L. Foucar, N. Kimmel, P. Holl, B. Rudek, B. Erk, A. Homke, C. Reich, D. Pietschner, G. Weidenspointner, L. Struder, G. Hauser, H. Gorke, J. Ullrich, I. Schlichting, S. Herrmann, G. Schaller, F. Schopper, H. Soltau, K.-U. Kuhnel, R. Andritschke, C.-D. Schroter, F. Krasniqi, M. Bott, S. Schorb, D. Rupp, M. Adolph, T. Gorkhover, H. Hirsemann, G. Potdevin, H. Graafsma, B. Nilsson, H. N. Chapman, and

J. Hajdu, "Single mimivirus particles intercepted and imaged with an X-ray laser", *Nature*, **470**, 78 (2011)

[169] G. J. Williams, H. M. Quiney, A. G. Peele, and K. A. Nugent, "Coherent diffractive imaging and partial coherence", *Phys. Rev. B*, **75**, 104102 (2007)

[170] B. Abbey, K. A. Nugent, G. J. Williams, J. N. Clark, A. G. Peele, M. A. Pfeifer, M. de Jonge, and I. McNulty, "Keyhole coherent diffractive imaging", *Nat. Phys.*, **4**, 394 (2008)

[171] C. Tieg, R. Frömter, D. Stickler, H. Stillrich, C. Menk, S. Streit-Nierobisch, L.-M. Stadler, C. Gutt, O. Leupold, M. Sprung, G. Grübel, and H. P. Oepen, "Overcoming the field-of-view restrictions in soft x-ray holographic imaging", *J. Phys. Conf. Ser.*, **211**, 012024 (2010)

[172] J. M. Rodenburg, A. C. Hurst, A. G. Cullis, B. R. Dobson, F. Pfeiffer, O. Bunk, C. David, K. Jefimovs, and I. Johnson, "Hard-X-Ray Lensless Imaging of Extended Objects", *Phys. Rev. Lett.*, **98**, 034801 (2007)

[173] O. Bunk, M. Dierolf, S. Kynde, I. Johnson, O. Marti, and F. Pfeiffer, "Influence of the overlap parameter on the convergence of the ptychographical iterative engine", *Ultramicroscopy*, **108**, 481 (2008)

[174] A. Tripathi, J. Mohanty, S. H. Dietze, O. G. Shpyrko, E. Shipton, E. E. Fullerton, S. S. Kim, and I. McNulty, "Dichroic coherent diffractive imaging", *Proc. Natl Acad. Sci. USA*, **108**, 13393 (2011)

[175] G. Grübel, G. Stephenson, C. Gutt, H. Sinn, and T. Tschentscher, "XPCS at the European X-ray free electron laser facility", *Nucl. Instrum. Meth. B*, **262**, 357 (2007)

[176] C. Gutt, L.-M. Stadler, A. Duri, T. Autenrieth, O. Leupold, Y. Chushkin, and G. Grübel, "Measuring temporal speckle correlations at ultrafast x-ray sources", *Opt. Express*, **17**, 55 (2009)

[177] E. E. Fenimore and T. M. Cannon, "Coded aperture imaging with uniformly redundant arrays", *Appl. Opt.*, **17**, 337 (1978)

[178] J. E. Trebes, K. A. Nugent, S. Mrowka, R. A. London, T. W. Barbee, M. R. Carter, J. A. Koch, B. J. MacGowan, D. L. Matthews, L. B. Da Silva, G. F.

Stone, and M. D. Feit, “Measurement of the spatial coherence of a soft-x-ray laser”, *Phys. Rev. Lett.*, **68**, 588 (1992)

[179] A. I. Gonzalez and Y. Mejia, “Nonredundant array of apertures to measure the spatial coherence in two dimensions with only one interferogram”, *J. Opt. Soc. Am. A*, **28**, 1107 (2011)

[180] K. A. Nugent, “Partially coherent diffraction patterns and coherence measurement”, *J. Opt. Soc. Am. A*, **8**, 1574 (1991)

[181] V. Kohn, I. Snigireva, and A. Snigirev, “Direct Measurement of Transverse Coherence Length of Hard X Rays from Interference Fringes”, *Phys. Rev. Lett.*, **85**, 2745 (2000)

[182] D. Stickler, R. Frömter, W. Li, A. Kobs, and H. P. Oepen, “Integrated setup for the fabrication and measurement of magnetoresistive nanoconstrictions in ultrahigh vacuum”, *Rev. Sci. Instrum.*, **79**, 103901 (2008)

[183] P. F. Carcia, “Perpendicular magnetic anisotropy in Pd/Co and Pt/Co thin-film layered structures”, *J. Appl. Phys.*, **63**, 5066 (1988)

[184] B. N. Engel, C. D. England, R. A. Van Leeuwen, M. H. Wiedmann, and C. M. Falco, “Interface magnetic anisotropy in epitaxial superlattices”, *Phys. Rev. Lett.*, **67**, 1910 (1991)

[185] S. Greaves, P. Grundy, and R. Pollard, “Magnetic properties of cobalt layers and Co/Pt multilayers”, *J. Magn. Magn. Mater.*, **121**, 532 (1993)

[186] M. T. Johnson, P. J. H. Bloemen, F. J. A. den Broeder, and J. J. de Vries, “Magnetic anisotropy in metallic multilayers”, *Rep. Prog. Phys.*, **59**, 1409 (1996)

[187] F. J. A. den Broeder, W. Hoving, and P. J. H. Bloemen, “Magnetic anisotropy of multilayer”, *J. Magn. Magn. Mater.*, **93**, 562 (1991)

[188] B. Kaplan and G. Gehring, “The domain structure in ultrathin magnetic films”, *J. Magn. Magn. Mater.*, **128**, 111 (1993)

[189] C. Kooy and U. Enz, “Experimental and theoretical study of the domain configuration in thin layers of BaFe12O19”, *Philips Res. Rep.*, **15**, 7 (1960)

[190] Z. Malek and V. Kambersky, “On the theory of the domain structure of thin films of magnetically uni-axial materials”, *Czechosl. Journ. Phys.*, **8**, 416 (1958)

[191] A. Maziewski, V. Zablotskii, and M. Kisielewski, "Analysis of Magnetic Domain Sizes in Ultrathin Ferromagnetic Films", *Phys. Status Solidi A*, **189**, 1001 (2002)

[192] J. E. Davies, O. Hellwig, E. E. Fullerton, G. Denbeaux, J. B. Kortright, and K. Liu, "Magnetization reversal of Co/Pt multilayers: Microscopic origin of high-field magnetic irreversibility", *Phys. Rev. B*, **70**, 224434 (2004)

[193] X. Shi, P. Fischer, V. Neu, D. Elefant, J. C. T. Lee, D. A. Shapiro, M. Farmand, T. Tyliszczak, H.-W. Shiu, S. Marchesini, S. Roy, and S. D. Kevan, "Soft x-ray ptychography studies of nanoscale magnetic and structural correlations in thin SmCo5 films", *Appl. Phys. Lett.*, **108**, 094103 (2016)

[194] M. Blume, "Magnetic scattering of x rays (invited)", *J. Appl. Phys.*, **57**, 3615 (1985)

[195] E. E. Fullerton, O. Hellwig, K. Takano, and J. B. Kortright, "Soft X-ray magnetic scattering as a probe of recording media", *Nucl. Instrum. Meth. B*, **200**, 202 (2003)

[196] H. A. Dürr, E. Dudzik, S. S. Dhesi, J. B. Goedkoop, G. van der Laan, M. Belakhovsky, C. Mocuta, A. Marty, and Y. Samson, "Chiral Magnetic Domain Structures in Ultrathin FePd Films", *Science*, **284**, 2166 (1999)

[197] J. Miguel, J. F. Peters, O. M. Toulemonde, S. S. Dhesi, N. B. Brookes, and J. B. Goedkoop, "X-ray resonant magnetic scattering study of magnetic stripe domains in *a*-GdFe thin films", *Phys. Rev. B*, **74**, 094437 (2006)

[198] D. Stickler, R. Frömter, H. Stillrich, C. Menk, H. P. Oepen, C. Gutt, S. Streit-Nierobisch, L.-M. Stadler, G. Grübel, C. Tieg, and F. Yakhou-Harris, "Domain size in systems with canted magnetization", *Phys. Rev. B*, **84**, 104412 (2011)

[199] Y. T. Millev, H. P. Oepen, and J. Kirschner, "Influence of external field on spin reorientation transitions in uniaxial ferromagnets. I. General analysis for bulk and thin-film systems", *Phys. Rev. B*, **57**, 5837 (1998)

[200] Y. T. Millev, H. P. Oepen, and J. Kirschner, "Influence of external fields on spin reorientation transitions in uniaxial ferromagnets. II. Ultrathin ferromagnetic films", *Phys. Rev. B*, **57**, 5848 (1998)

[201] D. Drouin, A. R. Couture, D. Joly, X. Tastet, V. Aimez, and R. Gauvin, "CASINO V2.42 A Fast and Easy-to-use Modeling Tool for Scanning Electron Microscopy and Microanalysis Users", *Scanning*, **29**, 92 (2007)

[202] R. Gauvin, P. Hovongton, P. Drouin, D.and Horny, H. Demers, and A. R. Couture, "Casino - monte CArlo Simulation of electroN trajectory in sOlids", Technical report, Universite de Sherbrooke (http://www.gel.usherbrooke.ca/casino/What.html)

[203] C. T. Chen, Y. U. Idzerda, H.-J. Lin, N. V. Smith, G. Meigs, E. Chaban, G. H. Ho, E. Pellegrin, and F. Sette, "Experimental Confirmation of the X-Ray Magnetic Circular Dichroism Sum Rules for Iron and Cobalt", *Phys. Rev. Lett.*, **75**, 152 (1995)

[204] K. Saravanan, C.-H. Kao, Y.-C. Shao, Y.-F. Wang, B.-Y. Wang, H. T. Wang, C.-J. Tsai, W.-C. Lin, C.-W. Pao, H.-M. Tsai, L.-Y. Jang, H. J. Lin, J.-F. Lee, and W.-F. Pong, "Magnetic anisotropic properties of Pd/Co/Pd trilayer films studied by X-ray absorption spectroscopy and magnetic circular dichroism", *RSC Adv.*, **5**, 19014 (2015)

[205] Y. Wu, J. Stöhr, B. D. Hermsmeier, M. G. Samant, and D. Weller, "Enhanced orbital magnetic moment on Co atoms in Co/Pd multilayers: A magnetic circular x-ray dichroism study", *Phys. Rev. Lett.*, **69**, 2307 (1992)

[206] N. Nakajima, T. Koide, T. Shidara, H. Miyauchi, H. Kawabe, H. Fukutani, A. Fujimori, K. Iio, T. Katayama, and Y. Suzuki, "Core-level magnetic circular dichroism in Co/Pt multilayers with varying Co-layer thicknesses", *J. Electron Spectrosc.*, **78**, 271 (1996)

[207] N. Nakajima, T. Koide, T. Shidara, H. Miyauchi, H. Fukutani, A. Fujimori, K. Iio, T. Katayama, M. Nývlt, and Y. Suzuki, "Perpendicular Magnetic Anisotropy Caused by Interfacial Hybridization via Enhanced Orbital Moment in Co/Pt Multilayers: Magnetic Circular X-Ray Dichroism Study", *Phys. Rev. Lett.*, **81**, 5229 (1998)

[208] R. Bodenberger and A. Hubert, "Zur bestimmung der blochwandenergie von einachsigen ferromagneten", *Phys. Status Solidi A*, **44**, K7 (1977)

[209] E. E. Underwood, *Quantitative Stereology*, (Addison-Wesley Educational Publishers Inc (1970), ISBN: 978-0201076509)

[210] O. Glatter and O. Kratky, *Small Angle X-ray Scattering*, (Academic Press (1982), ISBN: 978-0122862809)

[211] M. J. Donahue and D. G. Porter, “OOMMF Users Guide”, *Nat. Inst. Standards Technol., Gaithersburg, MD, USA, Interagency Rep. NISTIR 6376* (1999)

[212] MicroMagnum, “http://micromagnum.informatik.uni-hamburg.de”, (2012)

[213] J. Thielsch, H. Stopfel, U. Wolff, V. Neu, T. G. Woodcock, K. Güth, L. Schultz, and O. Gutfleisch, “In situ magnetic force microscope studies of magnetization reversal of interaction domains in hot deformed Nd-Fe-B magnets”, *J. Appl. Phys.*, **111**, 103901 (2012)

[214] C. Forbes, M. Evans, N. Hastings, and B. Peacock, *Statistical Distributions*, (John Wiley & Sons, Inc. (2011), ISBN: 978-0470390634)

[215] M. S. Pierce, C. R. Buechler, L. B. Sorensen, J. J. Turner, S. D. Kevan, E. A. Jagla, J. M. Deutsch, T. Mai, O. Narayan, J. E. Davies, K. Liu, J. H. Dunn, K. M. Chesnel, J. B. Kortright, O. Hellwig, and E. E. Fullerton., “Disorder-Induced Microscopic Magnetic Memory”, *Phys. Rev. Lett.*, **94**, 017202 (2005)

[216] B. Lilley, “LXXI. Energies and widths of domain boundaries in ferromagnetics”, *The London, Edinburgh, and Dublin Philosophical Magazine and Journal of Science*, **41**, 792 (1950)

[217] H. Träuble, O. Boster, H. Kronmüller, and A. Seeger, “Ferromagnetische Eigenschaften hexagonaler Kobalt-Einkristalle”, *Phys. Status Solidi B*, **10**, 283 (1965)

[218] S. Schaffert, *Holographic Imaging and Time-Resolved X-ray Scattering on Magnetic-Domain systems*, Ph.D. thesis, Technische Universität Berlin (2014)

[219] A. Malik, A. R. Sandy, L. B. Lurio, G. B. Stephenson, S. G. J. Mochrie, I. McNulty, and M. Sutton, “Coherent X-Ray Study of Fluctuations during Domain Coarsening”, *Phys. Rev. Lett.*, **81**, 5832 (1998)

[220] R. Frömter, H. Stillrich, C. Menk, and H. P. Oepen, “Imaging the Cone State of the Spin Reorientation Transition”, *Phys. Rev. Lett.*, **100**, 207202 (2008)

[221] Y. Millev and J. Kirschner, “Reorientation transitions in ultrathin ferromagnetic films by thickness- and temperature-driven anisotropy flows”, *Phys. Rev. B*, **54**, 4137 (1996)

[222] R. C. O´Handley, *Modern Magnetic Materails: Principles and Applications*, (John Wiley & Sons, Inc. (2000), ISBN: 978-0471155669)

[223] H. Ibach, *Physics of Surfaces and Interfaces*, (Springer-Verlag (2006), ISBN: 978-3-540-34710-1)

[224] M. B. Stearns, *Landolt-Börnstein - Group III Condensed Matter, Numerical Data and Functional Relationship in Science and Technology*, volume 19a, (Springer-Verlag (1986), ISBN: 3-540-15904-5)

[225] P. F. Carcia, A. D. Meinhaldt, and A. Suna, "Perpendicular magnetic anisotropy in Pd/Co thin film layered structures", *Appl. Phys. Lett.*, **47**, 178 (1985)

[226] F. J. A. den Broeder, D. Kuiper, H. C. Donkersloot, and W. Hoving, "A comparison of the magnetic anisotropy of [001] and [111] oriented Co/Pd Multilayers", *Appl. Phys. A*, **49**, 507 (1989)

[227] H. Draaisma, W. de Jonge, and F. den Broeder, "Magnetic interface anisotropy in Pd/Co and Pd/Fe multilayers", *J. Magn. Magn. Mater.*, **66**, 351 (1987)

[228] L. Néel, "Magnetic surface anisotropy and superlattice formation by orientation.", *J. Phys. Radium*, **15**, 225 (1954)

[229] D. Stickler, *Abbildung von magnetischen Mikrostrukturen mittels Fourier-Transforms-Holographie*, Ph.D. thesis, Universität Hamburg (2010)

[230] W. B. Zeper, F. J. A. M. Greidanus, P. F. Carcia, and C. R. Fincher, "Perpendicular magnetic anisotropy and magneto-optical Kerr effect of vapor-deposited Co/Pt-layered structures", *J. Appl. Phys.*, **65**, 4971 (1989)

[231] H. Stillrich, C. Menk, R. Frömter, and H. P. Oepen, "Magnetic anisotropy and the cone state in Co/Pt multilayer films", *J. Appl. Phys.*, **105**, 07C308 (2009)

[232] H. P. Oepen, M. Speckmann, Y. Millev, and J. Kirschner, "Unified approach to thickness-driven magnetic reorientation transitions", *Phys. Rev. B*, **55**, 2752 (1997)

[233] H. B. G. Casimir, J. Smit, U. Enz, J. F. Fast, H. P. J. Wijn, E. W. Gorter, A. J. W. Duyvesteyn, J. D. Fast, and J. J. de Jong, "Rapport sur quelques recherches dans le domaine du magnetisme aux laboratoires Philips", *J. Phys. Radium*, **20**, 360 (1959)

[234] J.-W. Lee, J.-R. Jeong, S.-C. Shin, J. Kim, and S.-K. Kim, "Spin-reorientation transitions in ultrathin Co films on Pt(111) and Pd(111) single-crystal substrates", *Phys. Rev. B*, **66**, 172409 (2002)

[235] J.-W. Lee, J. Kim, S.-K. Kim, J.-R. Jeong, and S.-C. Shin, "Full vectorial spin-reorientation transition and magnetization reversal study in ultrathin ferromagnetic films using magneto-optical Kerr effects", *Phys. Rev. B*, **65**, 144437 (2002)

[236] Y. Millev, "Bose - Einstein integrals and domain morphology in ultrathin ferromagnetic films with perpendicular magnetization", *J. Phys.: Condens. Matter*, **8**, 3671 (1996)

[237] M. Speckmann, H. P. Oepen, and H. Ibach, "Magnetic Domain Structures in Ultrathin Co/Au(111): On the Influence of Film Morphology", *Phys. Rev. Lett.*, **75**, 2035 (1995)

[238] A. Suna, "Perpendicular magnetic ground state of a multilayer film", *J. Appl. Phys.*, **59**, 313 (1986)

[239] H. J. G. Draaisma and W. J. M. de Jonge, "Magnetization curves of Pd/Co multilayers with perpendicular anisotropy", *J. Appl. Phys.*, **62**, 3318 (1987)

[240] G. Shirane, V. J. Minkiewicz, and R. Nathans, "Spin Waves in 3d Metals", *J. Appl. Phys.*, **39**, 383 (1968)

[241] M. Shalaby, C. Vicario, and C. P. Hauri, "The terahertz frontier for ultrafast coherent magnetic switching: Terahertz-induced demagnetization in ferromagnets", *arXiv:1506.05397* (2015)

[242] L. Müller, S. Schleitzer, C. Gutt, B. Pfau, S. Schaffert, J. Geilhufe, C. von Korff Schmising, M. Schneider, C. M. Günther, F. Büttner, F. Capotondi, E. Pedersoli, S. Düsterer, H. Redlin, A. Al-Shemmary, R. Treusch, J. Bach, R. Frömter, B. Vodungbo, J. Gautier, P. Zeitoun, H. Popescu, V. Lopez-Flores, N. Beaulieu, F. Sirotti, N. Jaouen, G. Malinowski, B. Tudu, K. Li, J. Lüning, H. P. Oepen, M. Kiskinova, S. Eisebitt, and G. Grübel, "Ultrafast Dynamics of Magnetic Domain Structures Probed by Coherent Free-Electron Laser Light", *Synchrotron Radiation News*, **26**, 27 (2013)

[243] S. Hashimoto, Y. Ochiai, and K. Aso, "Perpendicular magnetic anisotropy and magnetostriction of sputtered Co/Pd and Co/Pt multilayered films", *J. Appl. Phys.*, **66**, 4909 (1989)

PUBLICATIONS

Publication List

Published

[P1] Kai Bagschik, Robert Frömter, Judith Bach, Björn Beyersdorff, Leonard Müller, Stefan Schleitzer, Magnus Hardensson Berntsen, Christian Weier, Roman Adam, Jens Viefhaus, Claus Michael Schneider, Gerhard Grübel, and Hans Peter Oepen. "Employing soft X-ray resonant magnetic scattering to study domain sizes and anisotropy in Co/Pd multilayers". *Phys. Rev. B,* **94**, 134413 (2016).

[P2] Kai Bagschik, Robert Frömter, Leonard Müller, Wojciech Roseker, Judith Bach, Philipp Staeck, Carsten Thönnißen, Stefan Schleitzer, Magnus Hardensson Berntsen, Christian Weier, Roman Adam, Jens Viefhaus, Claus Michael Schneider, Gerhard Grübel, and Hans Peter Oepen. "Spatial coherence determination from the Fourier analysis of a resonant soft X-ray magnetic speckle pattern". *Opt. Express,* **24**, 23162 (2016).

[P3] Christian Weier, Roman Adam, A. Kakay, D.E. Bürgler, Robert Frömter, Judith Bach, Björn Beyersdorff, Kai Bagschik, Gerrit Winkler, Andre Kobs, Leonard Müller, Stefan Schleitzer, Magnus Hardensson Berntsen, P. Grychtol, Hans Peter Oepen, H. C. Kapeyn, M. M. Murnane, Claus Michael Schneider. "Studying magnetic domains in ferromagnetic alloys and multilayers using soft X-ray scattering". *JARA-FIT Annual Report,* 133 (2014).

Conference Contributions

[C1] Judith Bach, Robert Frömter, Björn Beyersdorff, Kai Bagschik, Christian Weier, Roman Adam, Leonard Müller, Stefan Schleitzer, Jens Viefhaus, Gerrit Winkler, Carsten Thönnißen, Christian Gutt, Gerhard Grübel, and Hans Peter Oepen,
High-resolved Soft X-ray Holographic Imaging at PETRA III,
Poster at 22nd International Congress on X-ray Optics and Microanalysis 2013, Hamburg (Germany).

[C2] Kai Bagschik, Robert Frömter, Judith Bach, Björn Beyersdorff, Hans Peter Oepen, Leonard Müller, Stefan Schleitzer, Magnus Hardensson Berntsen, Gerhard Grübel, Christian Weier, Roman Adam, and Claus Michael Schneider,
High-Resolution Magnetic Imaging with Soft X-ray Holographic Microscopy,
Talk at CUI Winter School 2013, Obergurgl (Germany).

[C3] Kai Bagschik, Carsten Thönnißen, Robert Frömter, Judith Bach, Björn Beyersdorff, Christian Weier, Roman Adam, Leonard Müller, Stefan Schleitzer, Jens Viefhaus, Gerrit Winkler, Andreas Meyer, Christian Gutt, Gerhard Grübel, and Hans Peter Oepen,
Imaging Magnetic Nanodots With Soft X-Ray Holographic Microscopy,
Poster at CUI International Symposium 2013, Hamburg (Germany).

[C4] Kai Bagschik, Robert Frömter, Judith Bach, Björn Beyersdorff, Hans Peter Oepen, Leonard Müller, Stefan Schleitzer, Magnus Hardensson Berntsen, Gerhard Grübel, Christian Weier, Roman Adam, and Claus Michael Schneider,
Investigation of Thickness-Driven Domain size via X-ray Resonant Magnetic Scattering,
Talk at Readi Workshop 2014 (Pier Workshop) 2014, Hamburg (Germany).

[C5] Kai Bagschik, Judith Bach, Björn Beyersdorff, Robert Frömter, Hans Peter Oepen, Leonard Müller, Stefan Schleitzer, Magnus Hardensson Berntsen, Gerhard Grübel, Christian Weier, Roman Adam, and Claus Michael Schneider,
Soft X-ray Holographic Microscopy,
Talk at PETRA III P04 Users Meeting 2014, Hamburg (Germany)

[C6] Kai Bagschik, Robert Frömter, Judith Bach, Björn Beyersdorff, Hans Peter Oepen, Leonard Müller, Stefan Schleitzer, Magnus Hardensson Berntsen, Gerhard Grübel, Christian Weier, Roman Adam, and Claus Michael Schneider,
Resonant X-ray scattering study of domain sizes in wedged multilayer samples,
Talk at CUI Winter School 2014, Weissenhäuser Strand (Germany).

[C7] Robert Frömter, Kai Bagschik, Judith Bach, Björn Beyersdorff, Christian Weier, Roman Adam, Leonard Müller, Stefan Schleitzer, Magnus Hardensson Berntsen, Gerhard Grübel, Claus Michael Schneider, and Hans Peter Oepen,
Blocking the collapse of domain size durcing spin-reorientation transition of canted Co/Pd multilayer films by second-order anisotropy,
Poster at MMM 2014, Hawai (USA).

[C8] Kai Bagschik and Stefan Schleitzer,
Ultrafast Optical Demagnetization of Nanosized Magnetic Domains Imaged via Soft X-ray Fourier Transform Holography,
Talk at 12th international conference on X-ray microscopy 2014, Melbourne (Australia).

[C9] Kai Bagschik, Judith Bach, Björn Beyersdorff, Carsten Thönnißen, Gerrit Winkler, Christian Weier, Roman Adam, Leonard Müller, Stefan Schleitzer, Jens Viefhaus, Claus Michael Schneider, Gerhard Grübel, and Hans Peter Oepen,
High-Resolution Soft X-Ray Holographic Microscope,
Poster at 12th international conference on X-ray microscopy 2014, Melbourne (Australia).

[C10] Jochen Wagner, Kai Bagschik, Judith Bach, Robert Frömter, Leonard Müller, Stefan Schleitzer, Jens Viefhaus, Christian Weier, Roman Adam, Claus Michael Schneider, Gerhard Grübel, and Hans Peter Oepen,
High-Resolution Soft X-ray Holographic Microscope,
Talk at DPG-Frühjahrstagung 2015, Berlin (Germany)

[C11] Kai Bagschik, Robert Frömter, Judith Bach, Björn Beyersdorff, Hans Peter Oepen, Leonard Müller, Stefan Schleitzer, Magnus Hardensson Berntsen, Gerhard Grübel, Christian Weier, Roman Adam, and Claus Michael Schneider,
Imaging if Magnetic Nanodots using X-ray Holographic Microscopy,

Talk at CUI Winter School 2016, Todtmoos (Germany) .

[C12] Kai Bagschik, Robert Frömter, Jochen Wagner, Stefan Freercks, Carsten Thönnißen, Judith Bach, Björn Beyersdorff, Hans Peter Oepen, Leonard Müller, Stefan Schleitzer, Gerhard Grübel, Magnus Hardensson Berntsen, Christian Weier, Roman Adam, and Claus Michael Schneider,
X-ray holographic imaging of magnetic nanostructures and spatial coherence determination,
Talk at PETRA III P04 Users Meeting 2016, Hamburg (Germany)

[C13] Jochen Wagner, Robert Frömter, Kai Bagschik, Stefan Freercks, Carsten Thönnißen, Björn Beyersdorff, Leonard Müller, Stefan Schleitzer, Magnus Hardensson Berntsen, Jens Viefhaus, Gerhard Grübel, and Hans Peter Oepen,
Arrays of magnetic nanodots studied by X-ray holographic microscopy and scattering,
Poster at MMM 2016, New Orleans (USA)

[C14] Jochen Wagner, Kai Bagschik, Stefan Freercks, Andre Kobs, Robert Frömter, Leonard Müller, Magnus Hardensson Berntsen, Gerhard Grübel, and Hans Peter Oepen,
Imaging of magnetic nanodots utilizing soft X-ray holograpic microscopy,
Talk at DPG-Frühjahrstagung 2016, Regensburg (Germany)

[C15] Jochen Wagner, Kai Bagschik, Robert Frömter, Stefan Freercks, Carsten Thönnißen, Andre Kobs, Leonard Müller, Magnus Hardensson Berntsen, Jens Viefhaus, Gerhard Grübel, and Hans Peter Oepen,
Imaging of magnetic nanodots utilizing soft X-ray holograpic microscopy,
Poster at PETRA III Variable Polarization XUV Beamline P04 User Meeting 2016, Hamburg (Germany)

[C16] Jochen Wagner, Robert Frömter, Kai Bagschik, Stefan Freercks, Carsten Thönnißen, Björn Beyersdorff, Leonard Müller, Stefan Schleitzer, Magnus Hardensson Berntsen, Jens Viefhaus, Gerhard Grübel, and Hans Peter Oepen,
Arrays of magnetic nanodots studied by X-ray holographic microscopy and scattering,
Poster at DESY Photon Science User Meeting 2017, Hamburg (Germany)

ACKNOWLEDGMENTS

An dieser Stelle möchte ich mich bei vielen Menschen bedanken, ohne deren Hilfe die Anfertigung dieser Doktorarbeit nicht möglich gewesen wäre. Mein ganz besonderer Dank gilt meinem Doktorvater Herrn Prof. Dr. Hans Peter Oepen, für die Betreuung meiner Doktorarbeit, für die vielen anregenden Diskussionen, für die Unterstützung und für die vielen Gespräche auf wissenschaftlicher und persönlicher Ebene. Meinen Dank gilt außerdem Herrn Prof. Dr. Gerhard Grübel für die Bereitschaft die Arbeit als Zweitgutachter zu beurteilen.

Mein außerordentlicher Dank gilt Dr. Robert Frömter, für die Unterstützung, die vielen Diskussionen, die für mich außerordentlich wertvollen Denkanregungen und Ratschläge und die Hilfe bei den Korrekturen dieser Arbeit. Während meiner Doktorarbeit konnte ich immer von seinen Erfahrungen profitieren nicht nur auf wissenschaftlicher, sondern auch auf persönlicher Ebene.

Des Weiteren möchte ich mich bei Dr. Leonard Müller bedanken, für die Unterstützung, die Betreuung und ganz besonders für die vielen wissenschaftlichen Diskussionen während unzähliger Strahlzeiten.

Judith Bach, Dr. Björn Beyersdorff, Dr. Christian Weier, Stefan Schleitzer und Dr. Magnus Berntsen möchte ich danken für die freundliche Unterstützung und die gemeinsamen erlebnisreichen Strahlzeiten an der P04 beamline.

Meinen CUI Buddys Daniel Riebesehl und Carsten Thönnißen möchte ich danken für die schöne Zeit während der ganzen Winter Schools, den Saunarunden und den vielen lustigen Gesprächen.

Jochen Wagner möchte ich danken für die gemeinsame Zeit in der Holografie-Gruppe, für die vielen Laufrunden um die Alster, die lustigen Gespräche, die

Unterstützung und den vielen Blutspende Abenden.

Jonathan Jacobsohn und Dr. Gerrit Winkler möchte ich danken für die Unterstützung bei der Herstellung der magnetischen Schichten.

Dr. Ándre Philippi-Kobs möchte ich danken für die vielen fachlichen Diskussionen über Magnetismus und die Hilfe bei der Korrektur dieser Arbeit.

Dr. Wojciech Roseker und Dr. Felix Lehmkühler möchte ich danken für die vielen Diskussion über speckle patterns und Kohärenz.

Außerdem möchte ich mich bei der ganzen Gruppe G bedanken für die schöne Zeit, das gute Arbeitsklima, die Unterstützung und die vielen großartigen Feiern.

Zum Schluss möchte ich mich noch bei meiner Familie bedanken. Ganz besonders möchte ich mich bei meiner Mutter Maria bedanken für die vielen guten Ratschläge und motivierenden Worte, außerdem bei meinem Vater Erwin für seine Unterstützung und meinen Geschwistern Tim, Jan und Nina. Vor allem möchte ich noch meiner Freundin Lena danken, für die aufbauenden Worte, die Unterstützung, das Verständnis und das immer die richtigen Worte finden.

EIDESSTATTLICHE VERSICHERUNG

Hiermit erkläre ich an Eides statt, dass ich die vorliegende Dissertationsschrift selbst verfasst und keine anderen als die angegebenen Quellen und Hilfsmittel benutzt habe.

I hereby declare, on oath, that I have written the present dissertation by my own and have not used other than the acknowledged resources and aids.

Hamburg, den (city and date) Unterschrift (signature)